

博士論文

論文題目 **Spin injection and spin transport in superconductors**
(超伝導体中におけるスピン注入とスピン輸送)

氏 名 若村 太郎

Spin injection and spin transport in superconductors

(超伝導体中におけるスピン注入とスピン輸送)

Doctoral thesis

Taro Wakamura

The University of Tokyo

March, 2015



東京大学
THE UNIVERSITY OF TOKYO



RIKEN



物性研究所

The Institute for Solid State Physics



RIKEN

Center for Emergent Matter Science



東京大学大学院
新領域創成科学研究科
GRADUATE SCHOOL OF FRONTIER SCIENCES
THE UNIVERSITY OF TOKYO

Advisory Committee:

Prof. Dr. Y. Otani, Chair/Advisor

Prof. Dr. H. Bouchiat

Prof. Dr. S. Maekawa

Prof. Dr. H. Takagi

Prof. Dr. F. Tsukihashi

Copyright by 2015. T. Wakamura

Abstract

Spin injection and spin transport in superconductors

(超伝導体中におけるスピン注入とスピン輸送)

若村太郎

Taro Wakamura

Spintronics is an active research field in condensed matter physics, whose aim is to exploit and manipulate the spin degree of freedom. Despite the growing interest in spintronics, however, spin transport in superconductors has not been explored yet especially from the experimental point of view. In this study, we have investigated spin transport in superconductors. We mainly discuss three subjects in the thesis; the spin relaxation time in a superconducting Nb, the inverse spin Hall effect (ISHE) in a superconducting niobium-nitride (NbN) and generation of the spin-triplet supercurrent in the superconductor (S) – ferromagnet (F) – S Josephson junctions.

Spin relaxation for spin currents is an important factor because it determines how long electrons can keep the initial direction of spin angular momentum. The most critical difference in spin transport in superconductors from that in normal metals is that it is mediated by the Bogoliubov quasiparticles, rather than electrons. These Bogoliubov quasiparticles can be regarded as a superposition of electron-like and hole-like excitations, and due to the different energy dispersion than that for electrons, the group velocity of the quasiparticles is smaller than that of electrons. Since spin relaxation occurs after electrons experience many scatterings by phonons and impurities, smaller group velocity brings about longer spin relaxation time. There have been several studies which investigate the spin relaxation time in superconductors, but their results are not conclusive: Due to spurious effects, underestimation or overestimation occurs, and it makes precise evaluation of the spin relaxation time difficult in superconductors.

In our work, we inject spin currents into a superconductor, and investigate the spin relaxation time in the superconducting state. We exclude the spurious effects described above by using the refined device structure, and attempt to estimate the spin relaxation time precisely. To attain this goal, we fabricate the lateral spin valve (LSV) devices. These devices are composed of two ferromagnet wires bridged by a nonmagnet wire. As a ferromagnet, we use permalloy (Py, $\text{Ni}_{81}\text{Fe}_{19}$), and as a nonmagnet, Cu. In these devices, when a change current passes between one of the two Py wires and the Cu bridge, a spin current is generated in the Cu. This spin current can be nonlocally detected using the other Py wire, and the detected signals are called nonlocal spin valve (NLSV) signals. We choose Nb as a superconductor because it has high critical temperature ($T_C = 9.2$ K) among metallic

superconductors, and also has large spin-orbit interaction (SOI). Large SOI is also good to observe the spin Hall effect (SHE). For materials with large SOI, the spin absorption technique is useful to inject spin currents. When a wire with large SOI is inserted below the Cu bridge in the LSVs, the spin current is partly absorbed into the Cu, because it is energetically favorable for the spin current to enter into the wire with large SOI and relax faster. As a result, the detected NLSV signals in the other Py wire are suppressed. Through this spin absorption technique, we inject spin currents into Nb and investigate the difference in the spin absorption between the normal state and the superconducting state.

We perform the spin absorption experiments both above and below T_C ($= 5.5$ K in our device). At 10 K, above T_C , the NLSV signals from the LSVs with the Nb middle wire are suppressed compared with those from the LSVs without the Nb middle wire, as in our previous studies. The spin absorption is independent of the magnitude of the charge current we flow between the Py spin injector and the Cu bridge (spin injection current, I). At 370 mK, much lower than T_C , however, the situation becomes drastically different: The spin absorption strongly depends on I , and as I decreases, the NLSV signals increase. These increasing NLSV signals are the signature of the suppressed spin absorption.

To determine the origin of this anomalous behavior in the spin absorption, we measure the resistance close to the Cu/Nb interface (R_1), because the interface is the most sensitive part for spin absorption. Temperature dependence of R_1 is first measured. We next fix the bath temperature and modulate I , and simultaneously measure R_1 . Then we obtain the same curve for the relation between R_1 and T , and R_1 and I . This indicates that the effective temperature at the Cu/Nb interface is deviated from that of the bath due to I .

Taking into account these effects, we carry out theoretical calculations. When transport of electrons between the Cu and Nb wire is considered, it is necessary to calculate the density of states (DOS) of Nb. We note that in our LSVs, the Cu/Nb interface is highly transparent owing to the fabrication through the shadow evaporation. For this transparent contact between a superconductor and a normal metal, it is essential to account for the superconducting proximity effect. The DOS of Nb can be calculated with the Usadel equation in this regime. The point to note here is that in the Usadel equation, there is a term which contains the spin relaxation time. Therefore by using the spin relaxation time as a fitting parameter, we can calculate the amount of the absorbed spin current into the Nb wire so as to reproduce the experimental data. We perform the calculation based on this idea, and succeed in reproducing the experimental data of the NLSV signals as a function of I at 370 mK (the bath temperature). From the theoretical fitting, we also obtain the spin relaxation time for each I . The spin relaxation time in the superconducting state is found to increase with decreasing I , and it becomes more than four times larger than that in the normal state when $I < 10$ μ A. Considering the effective temperature increase with I , this result is a clear experimental demonstration of the

enhanced spin relaxation time in the superconducting state with decreasing temperature, as theoretically predicted.

We next investigate the SHE in a superconductor. In place of Nb used in the above study, we use niobium-nitride (NbN) in the present case owing to higher T_C . The device is composed of a Py wire and a NbN wire bridged by a Cu wire. Using the spin absorption technique, we can inject pure spin currents into the NbN wire. The injected spin currents are converted into charge currents through the ISHE, which can be detected as a voltage difference between the two edges of the NbN wire. The detected voltage depends on the orientation of the spin polarization of the injected spin currents, which follows the direction of the magnetization of the Py spin injector. Thus during the measurements we apply the inplane magnetic field to control the magnetization of the Py.

We perform the ISHE measurements both at 20 K ($> T_C = 10$ K) and 3 K ($< T_C$). At 20 K, we observe typical inverse spin Hall signals (ΔR_{ISHE}), and ΔR_{ISHE} do not depend on the magnitude of the spin injection current (I).

We next measure the ISHE at 3 K, then ΔR_{ISHE} first decreases with decreasing I , and then for $I < 100$ μA they increase dramatically. With $I = 0.01$ μA , the signal is more than 2000 times larger than that in the normal state.

To confirm that the observed signals derive from the ISHE, we measure the angular dependence of the signals on the angle θ between the external magnetic field and the longitudinal axis of the Py spin injector. Then the angular dependence shows the sinusoidal relation to θ , a signature of the ISHE.

We also investigate how superconductivity of NbN plays a role for this enormous ISHE. As noted above, the unique feature of spin transport in superconductors is that it is mediated by the Bogoliubov quasiparticles. These quasiparticles are composed of a combination of electron-like and hole-like excitations. At equilibrium, the number of quasiparticles in the electron-like branch and hole-like branch is balanced. When the ISHE occurs in superconductors, this balance between the two branches is broken, and the charge imbalance (CI) occurs. This charge CI effect is a nonequilibrium phenomenon, and has to relax in a certain time or length. The ISHE can be detected through the CI effect in the superconducting state, and to obtain the signals one has to place the voltage probes within the length (CI length) from the region where the ISHE occurs. In the ISHE in NbN, due to large SOI of NbN thus the small spin diffusion length, the ISHE arises just below the Cu/NbN interface in the NbN wire. Therefore if superconductivity plays a role for the enormous ISHE, there should be a distance dependence of the detected signals between the Cu/NbN junction and the voltage probe (d). To confirm this scenario, we prepare two devices with different d , $d = 0.4$ μm and 10 μm . As a CI length, we use 4 μA from the value for Al as a reference. We measure ΔR_{ISHE} for the two devices at 3 K and 20 K. At 20 K, they show almost the same magnitude of ΔR_{ISHE} . However, at 3 K, while the device with $d = 0.4$ μm shows very large signals, signals from that with d

= 10 μm are strongly suppressed. Based on these results, we can conclude that the signals are detected via the CI effect and superconductivity of NbN should play an important role for the enormous ISHE.

We next carry out calculations to analyze the experimental data. ΔR_{ISHE} is proportional to the longitudinal resistivity ρ_{xx} and its quadratic, ρ_{xx}^2 . In superconductors, ρ_{xx} has to be replaced by ρ_{qp} , the resistivity of quasiparticles. Due to the superconducting gap, ρ_{qp} is written as $\rho_{xx}/2f_0(\Delta)$, where $f_0(\Delta)$ is the Fermi distribution function at the superconducting gap Δ . Since ρ_{qp} is increasing with decreasing temperature, ΔR_{ISHE} can also be enhanced. Based on this idea, we perform numerical calculations, and obtain increasing ΔR_{ISHE} with decreasing temperature (T). We note here that in our experiments, is increasing with I , not T . To investigate the relation between I and T , we measure the resistance close to the Cu/NbN interface (R_1) in the same way as that described above. Then we obtain a good agreement between the relation R_1 vs temperature and R_1 vs I . By comparing these two relations, we can relate the effective temperature at the Cu/NbN interface to I . However, direct substitution of this relation into the equation between ΔR_{ISHE} and T does not reproduce the enormous enhancement of ΔR_{ISHE} with decreasing I . Based on the obtained relation between I and T through R_1 , we assume that the effective temperature at the Cu/NbN interface is proportional to the square-root of I . By using this relation we can reproduce the experimental data fairly well.

The final subject is generation of the spin-triplet supercurrents in SFS Josephson junctions. Spin-triplet supercurrents are attractive in terms of spintronics because they can carry spin angular momentum truly without dissipation. In recent years, there have been reports on the observation of spin-triplet supercurrents in SFS Josephson junctions by using strong ferromagnets as Fs. However, no studies have directly linked spin-triplet supercurrents to spintronics.

To explore the potentiality of spin-triplet supercurrents for spintronics, we fabricate the SFS Josephson junction composed of the Co ferromagnetic wire and two tungsten (W) wires deposited by the Focused-Ion-Beam (FIB) system. W deposited by FIB systems is known to show T_C much higher than that of bulk W. We first measure superconductivity of W itself, and observe $T_C = 9.5$ K for our devices. We next measure the superconducting transition of the W-Co-W Josephson junction, where W-W distance (d) is 600 nm. Then we obtain the zero resistance through the junction at 7 K, even though d is much larger than the coherence length of the ferromagnet based on spin-singlet supercurrents. We also confirm that ferromagnetism of the Co wire is sustained by measuring the anisotropic magnetoresistance at room temperature. These facts support the observation of spin-triplet supercurrents in our device, which might be induced by the spin active interface due to the strong SOI of W wires.

Contents

1	Introduction	4
1.1	General reviews	4
1.2	Review on spin transport in superconductors	11
2	Theoretical backgrounds	15
2.1	Spin transport	15
2.1.1	Spin transport model in nonlocal spin valves	15
2.1.2	Spin relaxation mechanism	18
2.2	Spin Hall effect	21
2.2.1	Anomalous Hall effect	21
2.3	Superconductivity	28
2.3.1	The BCS theory	28
2.3.2	Spin transport in superconductors	30
2.3.3	Odd-frequency spin-triplet superconductors	30
2.3.4	Spin-triplet supercurrents and spintronics	33
3	Experimental methods	34
3.1	Sample fabrication	34
3.1.1	Electron-beam lithography and Liftoff process	34
3.1.2	Shadow evaporation technique	36
3.1.3	Focused-ion-beam deposition and sputtering	37
3.2	Measurements	39
3.2.1	Measurement circuits	39
3.2.2	Cooling system	40
4	Spin injection into a superconductor with strong spin-orbit coupling	42
4.1	Introduction and Motivation	42
4.2	Experimental results	45
4.3	Analysis	49
4.4	Interface effects: shadow evaporation vs sputtering	56

4.5	Brief summary	61
5	Quasiparticle-mediated spin Hall effect in a superconductor	63
5.1	Introduction and Motivation	63
5.2	Experimental results	66
5.3	Analyses	75
5.4	Optimization of the NbN fabrication process	84
5.5	Direct spin Hall effect	87
5.6	Brief summary	87
6	Application of odd-frequency spin-triplet supercurrent to spintronics	89
6.1	Motivation	89
6.2	Experimental results	93
6.3	Problems and future studies	95
7	Conclusions and future perspective	97
7.1	Conclusions on spin transport in superconductors	97
7.1.1	Spin injection into a superconductor with strong spin-orbit coupling	97
7.1.2	Quasiparticle-mediated spin Hall effect in a superconductor	98
7.2	Future perspectives	99
7.2.1	Spin transport in high T_C superconductors	99
7.2.2	Spin Hall effect in $6p$ metals	101

Chapter 1

Introduction

In this section we briefly introduce the concept of spintronics, reviewing some outstanding previous studies which have moved the field forward dramatically. We also show the state-of-art research results and experimental techniques.

1.1 General reviews

Our modern society largely relies on electronics. Progress in electronics makes our daily lives more convenient and comfortable. While the heart of electronics is to manipulate charge degrees of freedom of electrons, as well known, electrons have not only charge degrees of freedom but also spin degrees of freedom. The main concept of spintronics

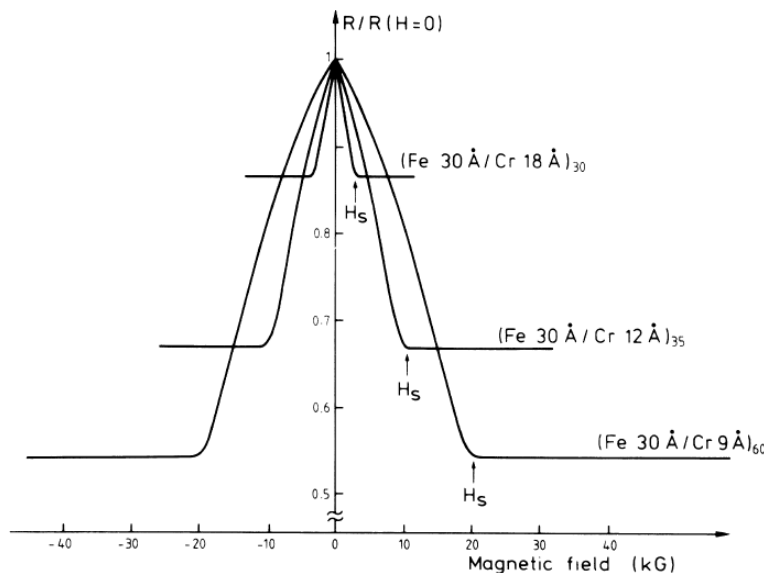


Figure 1.1: Results of the GMR experiment by Baibach *et al.* [4]. In this experiment a current flows in a Cr plane. As the thickness of the Cr layer decreases, the magnetoresistance value becomes larger. This shows enhancement of the magnetization effect from two ferromagnets which sandwich a Cr layer.

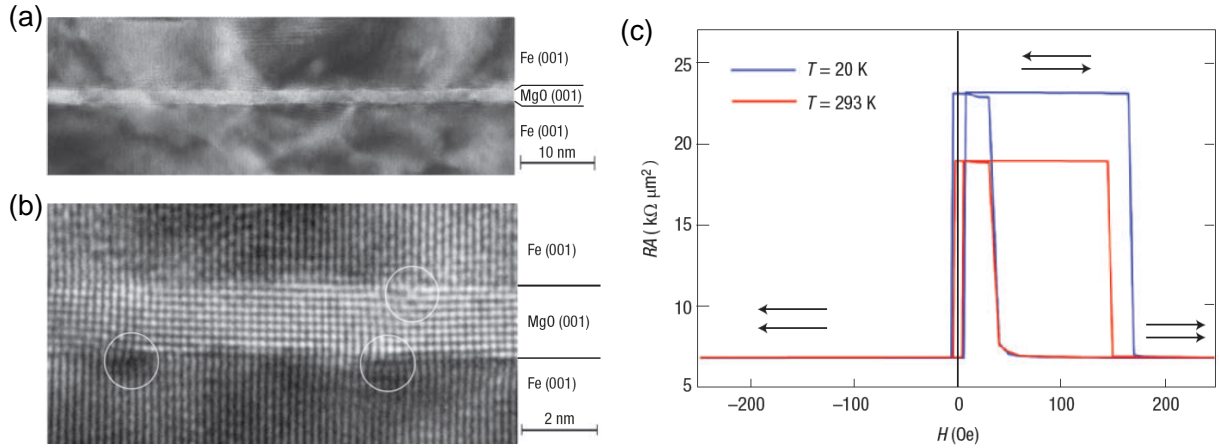


Figure 1.2: Experimental results on the giant tunnel magnetoresistance done by Yuasa *et al* [6]. (a) and (b): The tunneling electrical microscope (TEM) cross-sectional image of the epitaxial layers.

[1], a new kind of electronics, is to manipulate the spin degrees of freedom of electrons as well as the charge degree of freedom.

Spintronics is now one of the most active research areas in condensed matter physics. The nomenclature of spintronics sounds novel, but its basic idea has already appeared long ago. Spin-dependent transport, an important topic in spintronics was first discovered by Mott in 1936 [2, 3]. He found that in ferromagnets, when a temperature is low enough that magnon scattering is negligible, electrons of majority spin and those of minority spin do not mix and the total conductivity can be expressed as a sum of that for each spin channel. Here majority and minority are defined if spin of the electrons are parallel or antiparallel to the magnetization of the ferromagnet. This finding based on a two-current model is highly insightful, and the idea is also applied to recent studies. While electronic transport in ferromagnets has kept its attention of researchers, current growing interest in spintronics was practically provoked in 1988 by the discovery of the giant magnetoresistance (GMR) effect by Fert *et al* [4], which retold the importance of spin-dependent transport. They fabricated superlattices composed of stacking layers of Fe and Cr, where the adjacent Fe layers are antiferromagnetically coupled. When the inplane magnetic field is applied, the Fe layers finally align in parallel, and magnetoresistance shows dramatically large values (Fig. 1.1). These GMR effect experiments are a clear evidence of spin-polarized transport, and the work has stimulated intensive studies to enhance the magnetoresistance ratio. In addition to the above "current-in-plane (CIP)" configuration, "current-perpendicular-to-plane (CPP)" setup was subsequently proposed [5]. The magnetoresistance ratio gradually increased, but the next breakthrough occurred in 2004: gigantic magnetoresistance

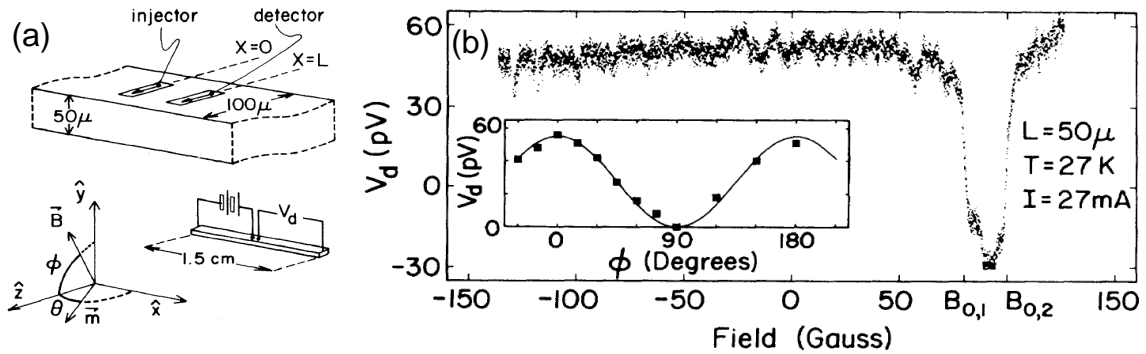


Figure 1.3: The first spin injection experiment by Johnson and Silsbee is shown [8]. (a): Sample structure. Two permalloy (Py) islands are on a bulk Al. A current flows between Py and Al, and a voltage is nonlocally detected between the Py and Al at the other side. (b): Detected voltage. An antiparallel magnetization state generates a voltage difference ~ 75 pV at $T = 27$ K. (Inset): Results of the Hanle effect measurements. Horizontal axis denotes the angle of the external magnetic field.

was reported for Fe(001)/MgO(001)/Fe(001) magnetic tunnel junctions ("tunneling magnetoresistance (TMR)" effect), shown in Fig. 1.2 [6, 7]. These reports have again triggered much interests in magnetoresistance and spin-dependent transport. Growing TMR ratio has also brought technological progress, and the TMR effect is now applied to magnetic random access memories (MRAM) and hard disc drives.

In the examples we have shown above, samples are multilayers structure where the thickness of each layer is an order of nanometres, and the lateral size is comparable to or more than micrometres. The biggest difference between charge and spin transport is that spin of electrons projected to a certain axis is not conserved. We normally define the length of spin as a projection of spin to one certain axis. When charge currents pass in a solid, electrons are scattered by impurities, phonons, grain boundaries, etc. However, charge of electrons is a scalar quantity and conserved. On the other hand, spin of electrons is scattered by magnons and magnetic impurities or relaxed by spin-orbit interaction. Spin of electrons is a vector quantity and its length is conserved, but its direction is deflected thus the projection of spin to a certain axis may change or disappear. Disappearance of spin occurs in a certain length scale (the spin diffusion length) or time scale (the spin relaxation time). Hence to observe spin-dependent phenomena, one has to place probes whose distance is less than the spin relaxation length. The spin diffusion length generically ranges from nanometre to micrometre. These scalelengths are easily accessible in a multilayer geometry by making the thickness of films an order of nanometre and measuring voltage difference between the top and the bottom of the layers. However, in a lateral geometry the story is not so simple because it is difficult to make the distance between two voltage probes an order of nanometres,

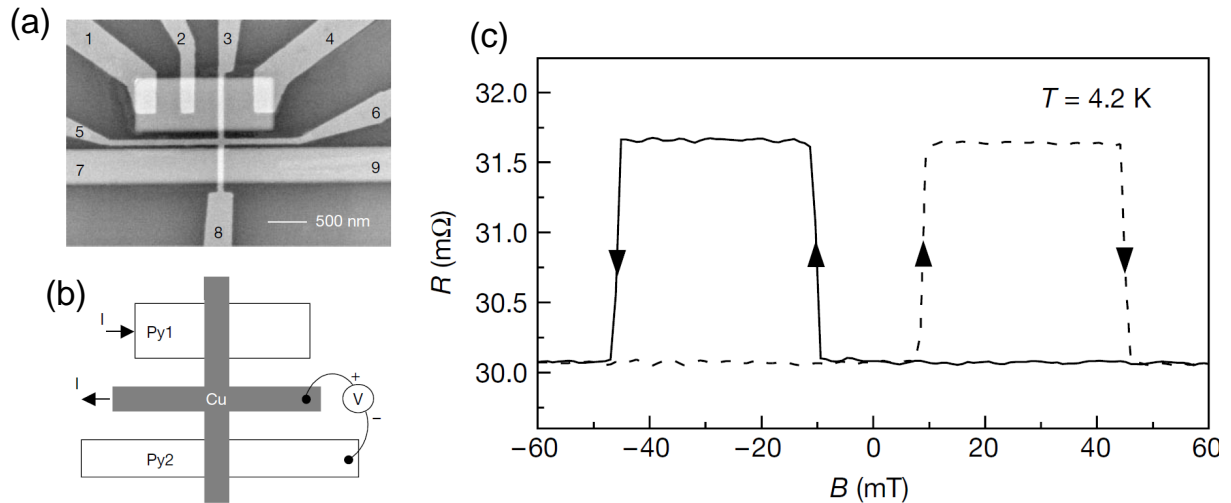


Figure 1.4: Nonlocal spin injection and detection experiments reported by Jedema *et al* [9]. (a) The SEM image of the nanoscale device. (b) Schematic illustration of the device. Electrical current is passing between the Py wire and one of the arms in the Cu cross, and the voltage is detected between another arm and the other Py wire. (c) Observed signal taken at 4.2 K. According to the parallel/antiparallel magnetization configuration, a finite signal is observed.

thus nanofabrication processes are essential.

The first pioneering work on spin transport in a lateral geometry has been performed by Johnson and Silsbee [8]. They have prepared the structure where two small pads of ferromagnets (permalloy, NiFe) are on an aluminum wire (Fig. 1.3). These two pads act as a spin injector and detector. When currents pass between one of the two pads and one edge of the wire and a voltage between the other pad and the other edge of the wire is detected, voltage difference is observed according to parallel/antiparallel magnetization configuration of the two ferromagnets. This is the first experimental demonstration of nonlocal spin injection and detection, but the detected voltage is vanishingly small because nanofabrication technique had not been established and the scale of the geometry is much larger than the spin diffusion length of aluminum, which is $\leq 1 \mu\text{m}$ even at low temperatures.

Spin transport measurements in lateral devices has evolved with the state-of-art nanofabrication techniques, especially the electron-beam (EB) lithography. Around fifteen years later since the first demonstration by Johnson and Silsbee, controlled experiment on nonlocal spin injection and detection was reported by Jedema *et al* [9]. (Fig. 1.4). They prepared nanometre-scale lateral spin valves (LSVs) and generated spin currents by passing charge currents between a ferromagnet and a nonmagnet. In their experiments much larger signals compared with those of the work by JS were observed because owing to nanofabrication, it was possible to make the distance between

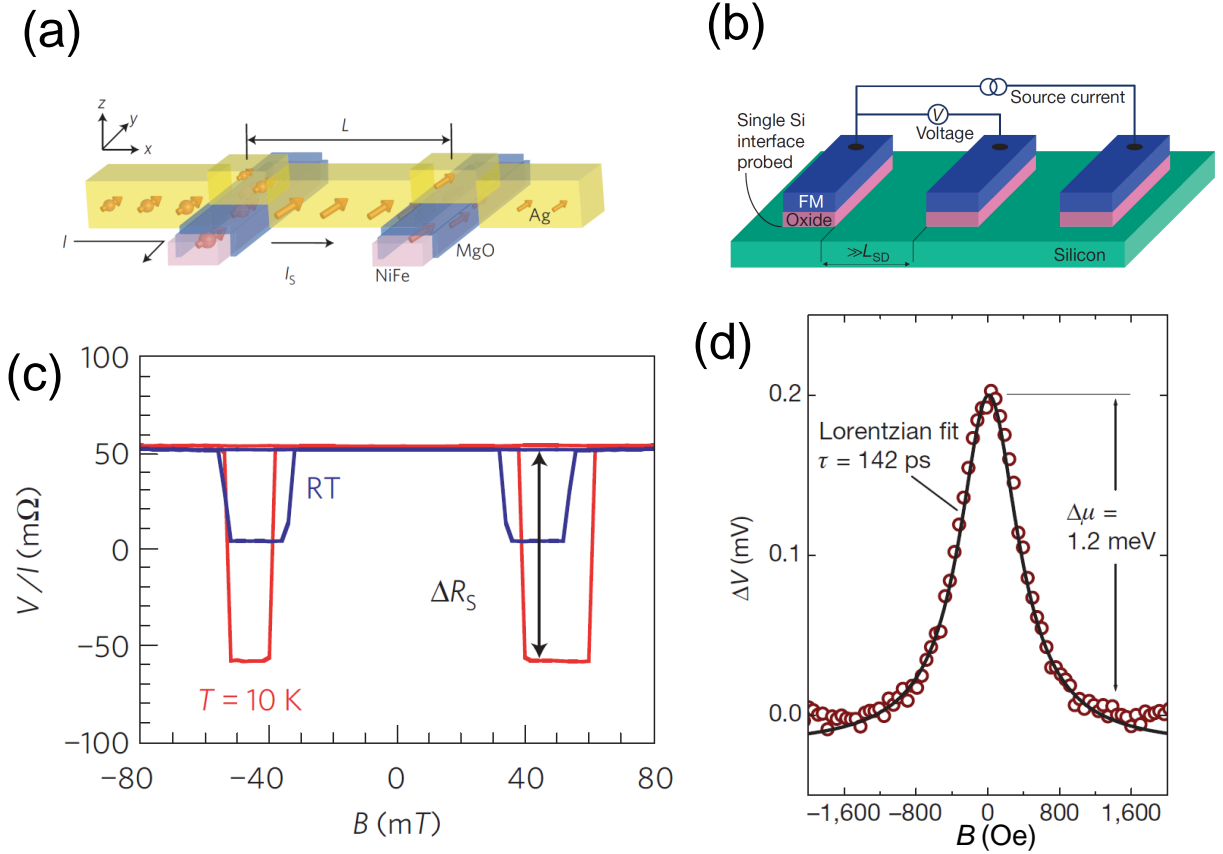


Figure 1.5: Examples of spin transport measurements. (a) and (c): NLSV measurements using Ag/Py lateral devices. To resolve the impedance mismatch problem, an MgO layer is inserted between Ag and Py ((a)). As a result, gigantic signals are observed both at room temperature (RT) and at 10 K. (b) and (d): three terminal Hanle measurement using silicon semiconductors. Spin transport properties are derived from the Hanle signals as shown in (d).

two voltage probes less than the spin diffusion length of Al. We note that this kind of LSVs are one of the most powerful tools to produce spin currents from charge currents. Inspired by the work by Jedema, many studies have been carried out to investigate spin transport properties for different kinds of materials and to find good materials for an efficient spin current generation, transport and detection. Typical materials used in these experiments are metals and semiconductors, but some exotic materials like graphene [10] or two dimensional electron gas in oxide heterostructures [11] are also used for spin transport experiments (see Fig. 1.5). Usually the word "spin current" refers to a flow of spin angular momentum carried by electrons, but on the other hand spin waves can also be regarded as a medium to propagate spin angular momentum. Spin transport through such "spin wave spin currents" has also been investigated by Kajiwara *et al.* [12]. This work is remarkable in terms of physics and highly promising

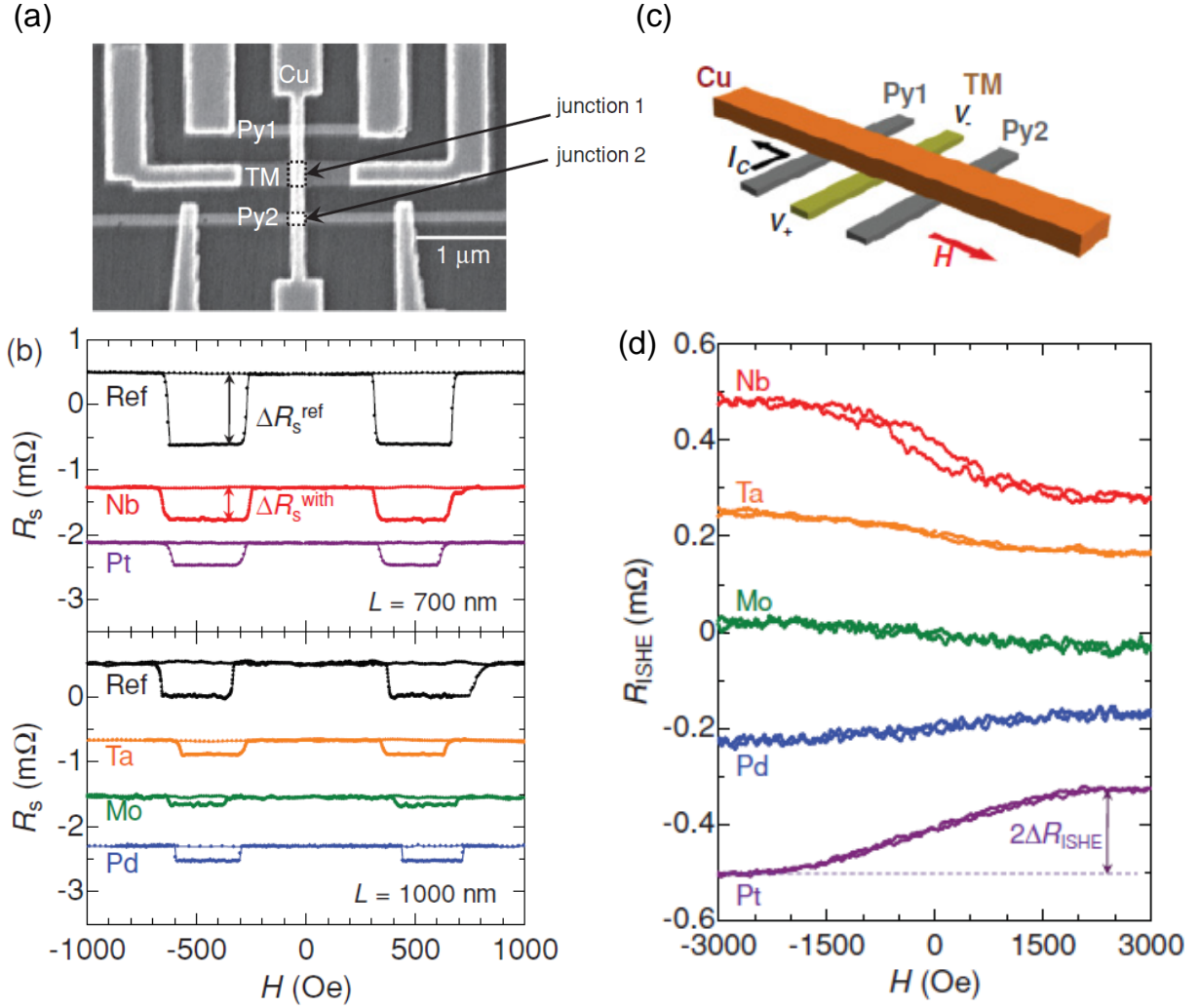


Figure 1.6: Measurements of the ISHE using the spin absorption technique by Morota *et al.* [25] (a): The SEM image of the device structure. (b): The NLSV signals obtained from with/without (Ref) middle wires. Metals with large SOI are used as middle wires. The decreased signals compared with those from samples without a middle wire demonstrate that spin currents are partly absorbed into the middle wires. (c): Schematic illustration of the ISHE measurements. Magnetic field is applied perpendicular to the longitudinal axis of the Py spin injector. (d): Detected signals with measurement setup as shown in (c). Inverse spin Hall signals are defined as $R_{\text{ISHE}} \equiv R(H > 2000\text{Oe}) - R(H < -2000\text{Oe})$.

for future applications to achieve dissipationless spintronics because one can transfer electrical signals through insulators.

We have introduced the LSVs as an example of the method to do conversion between spin and charge currents. As explained above, an efficient spin-charge conversion is an important task in spintronics, and this conversion is possible also via the spin Hall effect (SHE) [13, 14]. The SHE is a phenomenon where spin currents are generated from

charge currents through spin-dependent scatterings by spin-orbit interaction (SOI). It has been first experimentally demonstrated using Al [15] and Pt subsequently [16, 17]. Evaluation of the amplitude of the SHE for different materials is also a current research topic of great interest in spintronics, and many studies have been reported using metals, semiconductors and even organics. By using the SHE, other techniques than the LSVs to investigate spin transport in materials become possible. One of the methods often used nowadays is the spin pumping [18, 19, 20, 21], and the spin-torque ferromagnetic resonance [22, 23, 24]. Electrical measurements are also useful to study the SHE [16, 25, 26, 27]. As an example, we show electrical measurements of the inverse spin Hall effect (ISHE) done by Morota *et al.* [25] in Fig. 1.6. The device structure is shown in Fig. 1.6(a). There are two ferromagnetic (F) wires bridged by a nonmagnetic wire (N), and below the nonmagnetic wire a middle wire (M) is inserted between the two F wires. We assume that the M has large SOI. As in nonlocal spin injection and detection measurements (nonlocal spin valve (NLSV) measurements), when currents pass between one of the two Fs and the N, spin currents are generated in the N. This spin current is partly absorbed into the M because the SOI of the M is larger than that of the N, and it is energetically favorable for spin currents to be absorbed into the M and there relax faster than flowing in the N with smaller SOI. Therefore spin currents detected by the other F is reduced so that the NLSV signal decreases. This spin absorption measurement is a powerful tool to inject spin currents into materials with large SOI. The absorbed spin currents are converted into charge currents via the ISHE in the M. The relation among the generated charge current vector \mathbf{J}_C , the direction of the spin polarization \mathbf{s} and the spin current vector \mathbf{J}_s are

$$\mathbf{J}_C \propto \mathbf{J}_s \times \mathbf{s}. \quad (1.1)$$

In the above measurements, \mathbf{J}_s is normal to the substrate due to the small spin diffusion length of the M with the large SOI. Therefore to detect the voltage difference between the two edges of the M, one has to apply an external magnetic field perpendicular to the F. Figure 1.6(d) shows experimental results of the ISHE obtained by spin absorption and the electrical detection of the ISHE. It is clear that amplitudes of the signals depend strongly on materials. Quantity which characterizes an efficiency of spin-charge conversion is the spin Hall (SH) angle $\alpha_{\text{SH}} \equiv \rho_{\text{SHE}}/\rho_{xx}$, where ρ_{SHE} is the SH resistivity and ρ_{xx} the longitudinal resistivity. α_{SH} depends on materials, and in Table 1.1 we show α_{SH} for representative materials.

Material	Spin Hall angle [%]	ref.
Pt	2.1 ± 0.5	[25]
Pd	1.2 ± 0.4	[25]
Ta	$-(0.37 \pm 0.11)$	[25]
β -W	30 ± 2	[24]
CuIr	2.1 ± 0.6	[26]
CuBi	$-(24 \pm 9)$	[27]

Table 1.1: Spin Hall angle for metals and alloys. SH angles are values at 10 K other than that of W.

1.2 Review on spin transport in superconductors

In the previous subsections we have mainly discussed progress in spintronics with normal metals, semiconductors and insulators. Since the main subject of the research is related to spin transport in superconductors, in this subsection we briefly remark on research progress in spintronics with superconductors.

Compared with spin transport in normal metals or semiconductors, less studies have been reported on spin transport in superconductors. However, there are several theoretical papers which propose novel phenomena occurring for spin transport in superconductors. A first example is the enhanced spin relaxation time in superconductors. The most important difference between spin transport in normal metals and superconductors is that in superconductors spin transport is mediated not by electrons but by superconducting (Bogoliubov) quasiparticles. These quasiparticles induce many novel phenomena to occur in superconductors which cannot be observed in normal metals. For example, as we will explain in the following theoretical part, the group velocity of superconducting quasiparticles is generally smaller than that of electrons. In metals, electrons move diffusively, and they move forward with being scattered by phonons, impurities or grain boundaries. Spin is slightly canted for each scattering process, and after experiencing many scattering processes they are completely randomized. Thus smaller group velocity brings smaller motion of particles and the spin relaxation time can become longer. This spin relaxation time enhancement in superconductors is theoretically predicted by Yamashita *et al.* [28]. Experimental studies on the spin relaxation time in superconductors have also been carried out, but conclusions are not consistent with each other (details are discussed in Chapter 4).

The SHE in superconductors is also one of the intriguing subjects in spintronics with superconductors. Gigantic SHE in superconductors is theoretically proposed: the basic idea is as follows: the spin Hall resistivity ρ_{SHE} , which offers an estimate of the

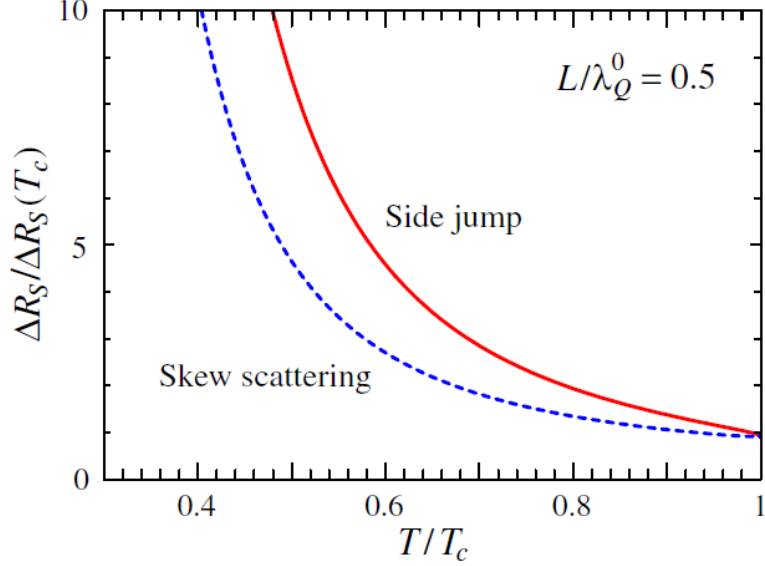


Figure 1.7: Results of the theoretical calculations for gigantic SHE in superconductors. As temperature (T) decreases below the critical temperature (T_C), the SH signal ΔR_S dramatically increases. In the Figure ΔR_S is normalized by that at T_C ($\Delta R_S(T_C)$)

amplitude of the SHE consists of two terms containing the longitudinal resistivity ρ_{xx} and is expressed as follows

$$\rho_{\text{SHE}} = a\rho_{xx} + b\rho_{xx}^2, \quad (1.2)$$

where a and b are both constants. Since spin transport is mediated by superconducting quasiparticles in superconductors, one has to replace the longitudinal resistivity ρ_{xx} with that of quasiparticles. According to the theory [29], the resistivity of superconducting quasiparticles ρ_{qp} may be written as

$$\rho_{\text{qp}} = \frac{\rho_{xx}^0}{2f_0(\Delta)}, \quad (1.3)$$

where $f_0(\Delta) = (\exp(\Delta/(k_B T)) + 1)^{-1}$ is the Fermi distribution function at the superconducting gap Δ , and ρ_{xx}^0 is the normal longitudinal resistivity just above T_C . Therefore (1.2) can be rewritten as

$$\rho_{\text{SHE}} = a \frac{\rho_{xx}^0}{2f_0(\Delta)} + b \left(\frac{\rho_{xx}^0}{2f_0(\Delta)} \right)^2. \quad (1.4)$$

Both terms in the rhs dramatically increases with decreasing T because $f_0(\Delta) \rightarrow 0$ when $T \rightarrow 0$. Thus the SHE in superconductors becomes gigantic.

As introduced above, the distinctive feature of spin transport in superconductors is that it is mediated by superconducting quasiparticles. When one injects electrons externally to superconductors, they are partly converted into Cooper pairs and partly

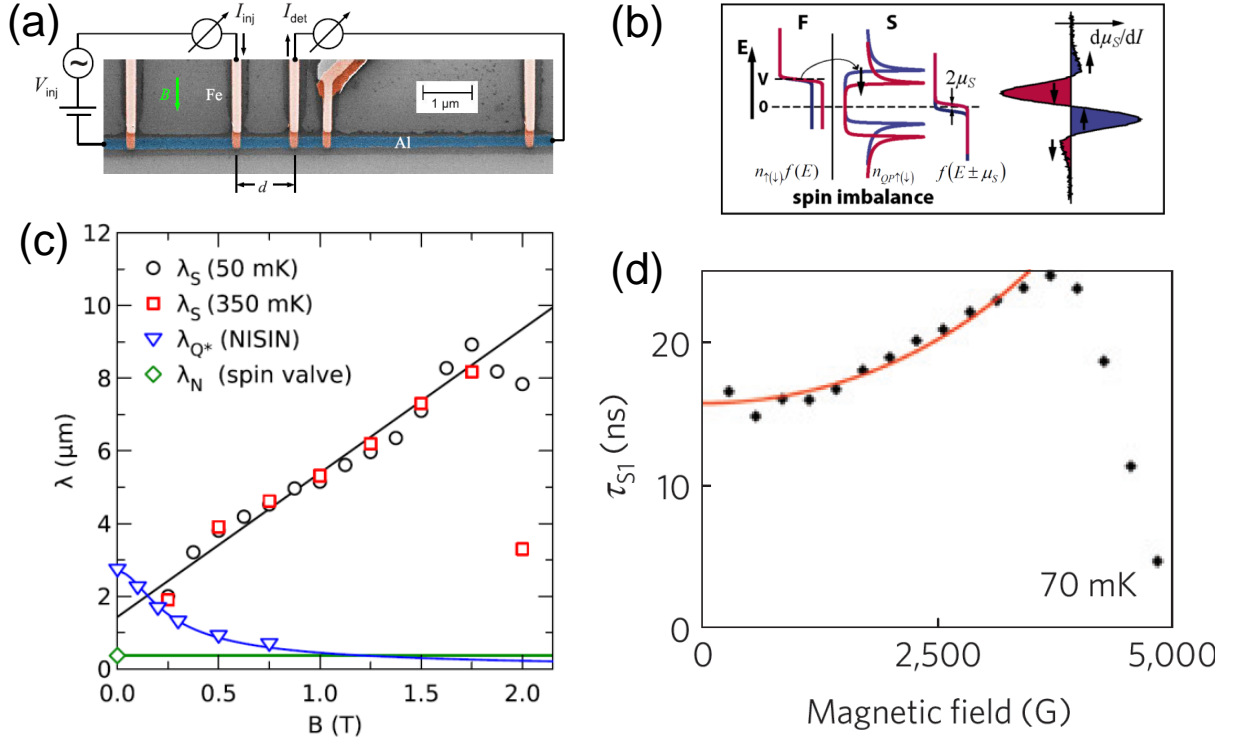


Figure 1.8: Experimental demonstration of the spin-charge separation in a superconducting Al reported by (A) Hübler *et al.* and (B) Quay *et al.* (a): the device image cited from (A). The structure is similar to the lateral spin valve device. (b): large external inplane magnetic field splits the DOS of superconducting Al, which largely suppresses spin relaxation of quasiparticles (from (B)). (c): the spin relaxation length λ_S and the charge imbalance length λ_Q are plotted as a function of the inplane magnetic field B . In the large B region, $\lambda_S \gg \lambda_Q$, which explicitly shows the spin-charge separation (from (A)). (d): enhanced spin relaxation time τ_{S1} is plotted as a function of magnetic field (from (B)).

into quasiparticles. One of the unique features of superconducting quasiparticles is that they are a superposition of electron-like and hole-like excitations. When charges are carried by quasiparticles, the number of quasiparticles on electron-like excitation branch and hole-like branch is different. However, at equilibrium and at a finite temperature the number of quasiparticles on each branch has to be balanced. The branch imbalance is called as the charge imbalance, and the charge imbalance finally relaxes into the equilibrium state during the lifetime of quasiparticles. When one injects spin currents or spin-polarized currents into a superconductor, the charge imbalance and the spin imbalance relaxes independently. This is called *spin-charge separation*. The spin charge separation for externally injected spin-polarized current was first theoretically predicted by Kivelson and Rokhsar [31], and experimental demonstration has been reported very recently [32, 33]. Experimental results are shown in Fig. 1.8. In both

studies they have fabricated lateral spin valve devices using superconducting Al, and inject spin currents from ferromagnets. Large inplane magnetic field was externally applied to the device. Because of the small SOI in Al, the density of states (DOS) of the superconducting Al becomes spin dependent (Fig 1.8(b)). Due to this spin split of the DOS, a down spin, for example, has to acquire an extra energy comparable or more than the Zeeman energy to flip itself into an up spin. This effect dramatically suppresses spin flip so that the spin diffusion length λ_S dramatically increases. Compared with the charge imbalance length λ_Q , $\lambda_S \gg \lambda_Q$ is a signature of the spin-charge separation. These reports are representative examples which exploit unique properties of superconductors for spintronics.

Chapter 2

Theoretical backgrounds

2.1 Spin transport

In this section we briefly discuss how to describe spin transport in materials based on the one-dimensional theoretical model proposed by Takahashi and Maekawa [35]. Analysis of our experimental data which will appear in the following chapters relies on this model.

2.1.1 Spin transport model in nonlocal spin valves

As discussed in the previous chapter, electrical spin injection and detection measurements using lateral spin valve (LSV) devices are highly useful to investigate spin transport properties in materials as demonstrated in many studies [9, 34].

Spin transport in LSVs can be described by the two current model proposed by Takahashi and Maekawa [35]. Typical LSV device geometry is shown in Fig. 2.1(a). The device is composed of two ferromagnetic (F) wires bridged by a nonmagnetic (N) wire. One of the F wires (F1) acts as a spin injector and the other F wire (F2) a spin detector. We assume that magnetization of the two wires is collinear to the longitudinal axis of the Fs due to the shape anisotropy. We define the width of the F and N wire as w_F and w_N , and the thickness d_F and d_N , respectively. The center-to-center distance between the two F wires is L .

Now we explain how to describe spin transport in the LSV device based on [35]. Our description is based on the two-current model and there are two channels, a channel for upspin and that for downspin. We assume diffusive motion of electrons typical in metals. In this regime with an electric field \mathbf{E} , spin-dependent currents consist of a drift part and a diffusive part: $\mathbf{j}_\sigma = \sigma_\sigma \mathbf{E} - e D_\sigma \nabla n_\sigma$, where σ_σ is the electrical conductivity of electrons with spin σ . Here σ is either \uparrow or \downarrow to the quantization axis. e is the charge of an electron, $e = -|e|$, n_σ the carrier density of electrons with spin σ and D_σ is the diffusion constant for σ . Using the relation $\nabla n_\sigma = N_\sigma \nabla \varepsilon_F^\sigma$ and the Einstein's

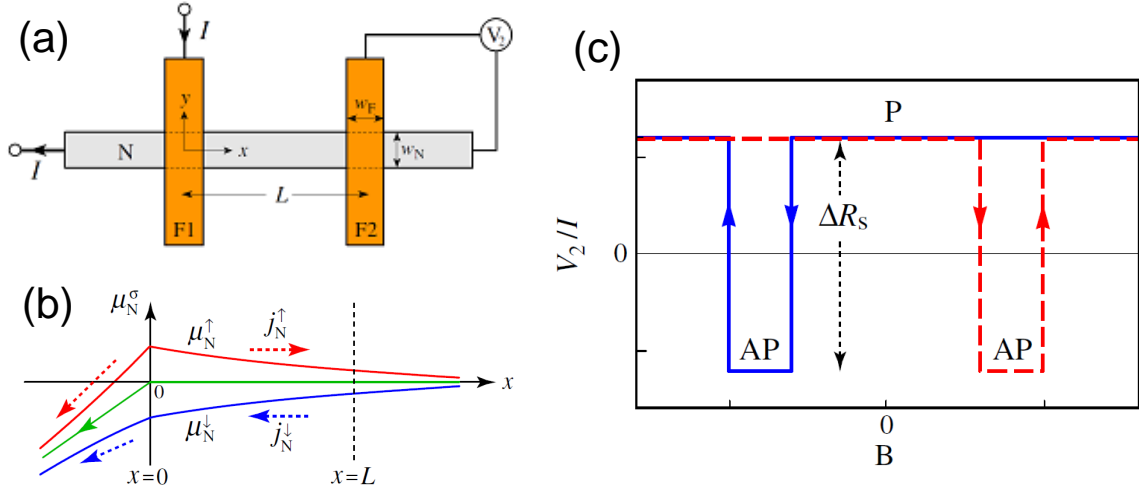


Figure 2.1: (a): Schematic illustration of the LSV structure and the NLSV measurement. A current flows between the ferromagnet and nonmagnet. A voltage is detected between the ferromagnet and nonmagnet at the other side nonlocally. (b): the ECP distribution of the NLSV structure. A pure spin current diffuses in the nonmagnet wire, where there are no charge currents. (c): Illustration of the typical NLSV signal. spin accumulation is defined by the difference in V_2/I between parallel/antiparallel magnetization of the two ferromagnet wires. [35]

relation $\sigma_\sigma = e^2 N_\sigma D_\sigma$ (N_σ : the density of states in the subband for spin σ , ϵ_F^σ : the Fermi energy of electrons with spin σ), the current density \mathbf{j}_σ can be expressed as

$$\mathbf{j}_\uparrow = -\frac{\sigma_\uparrow}{e} \nabla \mu_\uparrow \quad (2.1)$$

$$\mathbf{j}_\downarrow = -\frac{\sigma_\downarrow}{e} \nabla \mu_\downarrow, \quad (2.2)$$

where $\mu_\sigma = \epsilon_F^\sigma + e\phi$ is the electrochemical potential (ECP) and ϕ is the electrostatic potential.

Since there is no divergence of charge currents, the continuity equation for charge and spin currents in the steady(time-independent) state is expressed as

$$\nabla \cdot (\mathbf{j}_\uparrow + \mathbf{j}_\downarrow) = 0 \quad (2.3)$$

$$\nabla \cdot (\mathbf{j}_\uparrow - \mathbf{j}_\downarrow) = -e \frac{n_\uparrow - \bar{n}_\uparrow}{\tau_{\uparrow\downarrow}} + e \frac{n_\downarrow - \bar{n}_\downarrow}{\tau_{\downarrow\uparrow}}, \quad (2.4)$$

where \bar{n}_σ represents the equilibrium carrier density of spin σ and $\tau_{\sigma\sigma'}$ the scattering time of an electron from a spin state σ to σ' . Substituting these equations into the

detailed balance equation $N_{\uparrow}/\tau_{\uparrow\downarrow} = N_{\downarrow}/\tau_{\downarrow\uparrow}$, equations from the ECP are

$$\nabla^2(\sigma_{\uparrow}\mu_{\uparrow} + \sigma_{\downarrow}\mu_{\downarrow}) = 0 \quad (2.5)$$

$$\nabla^2(\mu_{\uparrow} - \mu_{\downarrow}) = \frac{1}{\lambda_{\text{sf}}^2}(\mu_{\uparrow} - \mu_{\downarrow}), \quad (2.6)$$

where $\lambda_{\text{sf}} = \sqrt{D\tau_{\text{sf}}}$ represents the spin diffusion length with the spin relaxation time τ_{sf} and the diffusion coefficient D . These two terms are described as

$$\frac{1}{\tau_{\text{sf}}} = \frac{1}{2} \left(\frac{1}{\tau_{\uparrow\downarrow}} + \frac{1}{\tau_{\downarrow\uparrow}} \right) \quad (2.7)$$

$$\frac{1}{D} = \frac{N_{\uparrow}/D_{\downarrow} + N_{\downarrow}/D_{\uparrow}}{N_{\uparrow} + N_{\downarrow}} \quad (2.8)$$

At the interface between the F and N wire, the ECP changes discontinuously if the interface is not transparent. In order to express this drop of the ECP, we introduce the spin dependent interface currents

$$I_1^{\sigma} = \frac{1}{eR_1^{\sigma}}(\mu_{\text{F1}}^{\sigma} - \mu_{\text{N}}^{\sigma}) \quad (2.9)$$

$$I_2^{\sigma} = \frac{1}{eR_2^{\sigma}}(\mu_{\text{F2}}^{\sigma} - \mu_{\text{N}}^{\sigma}). \quad (2.10)$$

where R_1^{σ} and R_2^{σ} are the resistance of the interface 1 and 2, μ_{F1}^{σ} , μ_{F2}^{σ} and μ_{N}^{σ} are the ECP of spin σ in the F1, F2 and N wire, respectively. Here we assume that currents flow uniformly through the interface.

Using the equations introduced above, we can derive distribution of spin currents $I_s = I_{\uparrow} - I_{\downarrow}$, taking account for the fact that both charge and spin currents conserve at each interface. As an example, when a bias current I flows from the F1 to the left side of the N ($I_1 = I$) and there are no charge currents on the right side of the N ($I_2 = 0$), we have the solution for the ECP. In the N, the ECP has a general form

$$\mu_{\text{N}}^{\sigma} = \bar{\mu}_{\text{N}} + \sigma(a_1 e^{-|x|/\lambda_{\text{N}}} - a_2 e^{-|x-L|/\lambda_{\text{N}}}). \quad (2.11)$$

Here $\bar{\mu}_{\text{N}} = -[eI/(\sigma_{\text{N}}A_{\text{N}})]x$ ($A_{\text{N}} = w_{\text{N}}d_{\text{N}}$) represents the charge transport, and therefore at $x > 0$, $\bar{\mu}_{\text{N}} = 0$. The second term generates the difference between the ECP of up-spin electrons and down-spin electrons. In this regime, in the region $x > 0$ in the N, spin currents without charge currents (named *pure spin currents*) flow. In the F, the ECP distributes as

$$\mu_{\text{F1}}^{\sigma} = \bar{\mu}_{\text{F1}} + \sigma b_1^{\sigma} e^{-z/\lambda_{\text{F}}}, \quad (2.12)$$

$$\mu_{\text{F2}}^{\sigma} = \bar{\mu}_{\text{F2}} - \sigma b_2^{\sigma} e^{-z/\lambda_{\text{F}}}. \quad (2.13)$$

In (2.13), we assume that $d_F \gg \lambda_F$ and $\bar{\mu}_{F1} = -[eI/(\sigma_F A_J)]z + eV_1$, $\bar{\mu}_{F2} = eV_2$. Using the condition that charge currents ($I = I_\uparrow + I_\downarrow$) and spin currents are continuous at the interface as mentioned above, we can determine the unknown coefficients. The spin-dependent voltage V_2 detected at the F2 is then given by

$$V_2/I = \pm 2R_N e^{-L/\lambda_N} \prod_{i=1}^2 \left(\frac{P_J \frac{R_i}{R_N}}{1 - P_J^2} + \frac{p_F \frac{R_F}{R_N}}{1 - p_F^2} \right) \times \left[\prod_{i=1}^2 \left(1 + \frac{2 \frac{R_i}{R_N}}{1 - P_J^2} + \frac{2 \frac{R_F}{R_N}}{1 - p_F^2} \right) - e^{-2L/\lambda_N} \right]^{-1}, \quad (2.14)$$

where $R_N = \rho_N \lambda_N / A_N$ and $R_F = \rho_F \lambda_F / A_J$ are the resistance of the N and F wire with the cross sections A_N and A_J . λ_N and λ_F are the spin diffusion length in the N and F, ρ_N and ρ_F are the resistivity of the N and F, respectively. p_F is the current polarization in the F. P_J denotes the polarization at the interface and is defined as $P_J = |G_i^\uparrow - G_i^\downarrow| / G_i$ with the interface conductance G_i at the interface i . + and - signs in the equation correspond to the parallel (P) and antiparallel (AP) magnetization configuration in the F1 and F2. The detected spin accumulation voltage is

$$\Delta R = I^{-1}(V_2^P - V_2^{AP}) = 2I^{-1}|V_2|, \quad (2.15)$$

by subtracting the detected voltage divided by I in the parallel and antiparallel magnetization configuration.

2.1.2 Spin relaxation mechanism

Spin relaxation and spin dephasing are one of the important topics in spintronics. Spin currents in materials are nonequilibrium and equilibrated by some mechanisms we will show below. There are mainly four mechanisms which contribute to spin relaxation: the Elliott-Yafet mechanism, the D'yakonov-Perel' mechanism, the Bir-Aronov-Pikus mechanism and the hyperfine interaction [36]. Since the Elliott-Yafet mechanism is the most relevant to metallic systems, we mainly explain the Elliott-Yafet mechanism and briefly discuss the other mechanisms.

In the Elliott-Yafet process electrons with upspin couple with those with downspin via the spin-orbit interaction (SOI) with ions in the lattice. Elliott pointed in 1954 that if there is a SOI between ions in the lattice and conduction electrons, spin of these electrons can relax via the momentum scattering like phonon scattering or impurity scattering [37].

SOI has a general form, which written as

$$V_{SO} = \frac{\hbar}{4m^2 c^2} (\nabla V_{SC} \times \mathbf{p}) \otimes \sigma, \quad (2.16)$$

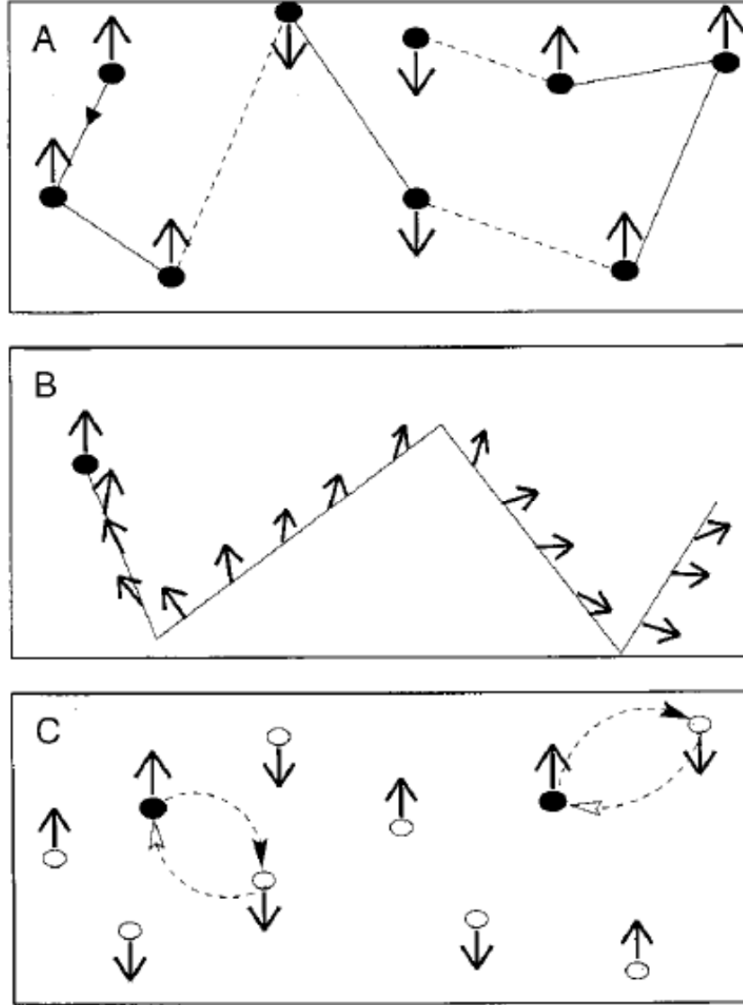


Figure 2.2: Schematic image of various spin relaxation mechanisms. (a): the Elliot-Yafet mechanism. Two spin channels are assumed, and after experiencing many momentum scatterings, spin flips to the other state. (b): the D'yakonov-Perel mechanism. Due to the lack of the inversion symmetry, spin feels an effective magnetic field, which continuously exerts a torque to tilt the spin. (c): the Bir-Pikus mechanism. The magnetic coupling between electrons and nuclei is important.

where m is the free-electron mass, V_{SC} is the scalar (spin-independent) periodic lattice potential, $\mathbf{p} \equiv -i\hbar\nabla$ is the linear momentum operator, and σ are the Pauli matrices, respectively.

Due to the SOI, spin of an electron and its momenta correlate, and the upspin state $|\uparrow\rangle$ and the downspin state $|\downarrow\rangle$ are no longer the eigenstates for σ_z . Therefore, the Bloch wave functions in solids are modified as

$$\Psi'_{\mathbf{k}\uparrow}(\mathbf{r}) = \alpha_{\mathbf{k}}(\mathbf{r})|\uparrow\rangle + \beta_{\mathbf{k}}(\mathbf{r})|\downarrow\rangle \quad (2.17)$$

$$\Psi'_{\mathbf{k}\downarrow}(\mathbf{r}) = \xi_{\mathbf{k}}(\mathbf{r})|\uparrow\rangle + \eta_{\mathbf{k}}(\mathbf{r})|\downarrow\rangle, \quad (2.18)$$

where $\Psi'_{\mathbf{k}\uparrow}(\mathbf{r})$ and $\Psi'_{\mathbf{k}\downarrow}(\mathbf{r})$ are the states which originally have $|\uparrow\rangle$ and $|\downarrow\rangle$ in the spin states, respectively. Mixing with the other spin state is therefore determined by the ratio between the coefficient of the original spin state and that of the other spin state. For example, for the Bloch wave function $\Psi'_{\mathbf{k}\uparrow}(\mathbf{r})$, the value of $\beta_{\mathbf{k}}(\mathbf{r})$ determines the strength of the mixing. A perturbative calculation leads to the results of $\beta_{\mathbf{k}}(\mathbf{r}) \sim \lambda_{\text{SO}}/\Delta E \ll 1$, where ΔE represents difference between two energy bands with the same \mathbf{k} and λ_{SO} the matrix element of V_{SO} between them. This result reflects the fact that the energy scale of V_{SO} is generally much less than the energy difference between the two neighboring states in the energy band. Thus usually we can neglect the mixing and approximate $\Psi'_{\mathbf{k}\uparrow}(\mathbf{r}) \sim |\uparrow\rangle$, for example.

However, in certain conditions, the value of $\beta_{\mathbf{k}}(\mathbf{r})$ becomes effective. Although the SOI itself does not cause spin relaxation, combination of the SOI with momentum scattering makes it effective. Momentum scattering is usually caused via scatterings with phonons or impurities. In combination with the phonon-mediated spin relaxation mechanism suggested by Yafet, a consistent picture of the phonon-induced spin relaxation has been established [38].

The spin relaxation of the Elliott-Yafet mechanism is characterized by the spin relaxation time τ_s . There are two important relations which give an order of magnitude of τ_s . One is the "Elliott relation" and gives the relative relation between τ_s and τ_p . Here τ_p represents the momentum relaxation time. After the Born approximation, one obtains

$$\frac{1}{\tau_s} \sim \frac{\beta^2}{\tau_p}. \quad (2.19)$$

Here we emphasize that τ_s linearly depends on τ_p . Another important relation is called the "Yafet relation", and expressed as

$$\frac{1}{\tau_s} \sim \beta^2 \rho(T). \quad (2.20)$$

This equation shows that the temperature dependence of τ_s is an inverse of that of the resistivity. We note that the momentum scattering is dominated by the phonon scattering at high T and by the impurity scattering at low T . This relation was experimentally confirmed by Monod and Beuneu [39].

One of the other mechanisms of the spin relaxation is the D'yakonov-Perel' mechanism. It originates from the SOI induced by the broken inversion symmetry of materials [40]. When the inversion symmetry is broken, the two Bloch states with the same momentum, such as $\Psi'_{\mathbf{k}\uparrow}(\mathbf{r})$ and $\Psi'_{\mathbf{k}\downarrow}(\mathbf{r})$ no longer degenerate, namely, $E_{\mathbf{k}\uparrow} \neq E_{\mathbf{k}\downarrow}$. In this regime, energy splitting between upspins electron and downspin electrons can be described by an intrinsic \mathbf{k} -dependent magnetic field $\mathbf{B}(\mathbf{k})$. This field is generally called the "Dresselhaus field" and derives from the SOI in the band structure. Since electrons

precess around this effective field, the corresponding Hamiltonian can be expressed as

$$\mathcal{H} = \frac{1}{2}\hbar\sigma \otimes \boldsymbol{\Omega}(\mathbf{k}), \quad (2.21)$$

where $\boldsymbol{\Omega}(\mathbf{k}) = (e/m)\mathbf{B}(\mathbf{k})$. Since the effective field depends on momentum of an electron \mathbf{k} , electrons experiencing different momentum scattering process feel different directions of $\boldsymbol{\Omega}(\mathbf{k})$. Thus this causes the spin dephasing.

The most important difference between the Elliott-Yafet and the D'yakonov-Perel' mechanism is how τ_s depends on τ_p : in the Elliott-Yafet mechanism, $\tau_s \propto \tau_p$ as explained above, and in the D'yakonov-Perel' mechanism, on the other hand, $\tau_s \propto 1/\tau_p$. This difference is widely used to determine the mechanism of spin relaxation in various materials.

The other mechanisms become significant especially in semiconductors. For example, the Bir-Aronov-Pikus mechanism is relevant to the exchange interaction between electrons and holes in *p*-doped semiconductors [41]. The hyperfine interaction between the magnetic moment of electrons and nuclei is important for the spin dephasing of localized electrons such as those in quantum dots or bound on donors [42]. It is usually trivial for itinerant electrons in metals and is negligible [43].

2.2 Spin Hall effect

2.2.1 Anomalous Hall effect

Spintronics is a field of research which contains many novel concepts, and the spin Hall effect (SHE) is one of the indispensable phenomena in the field. However, the SHE can be regarded as an analogue of the anomalous Hall effect (AHE), a longstanding controversial topic in condensed matter physics. Therefore we first review the AHE to understand the SHE more profoundly. The Hall effect was first discovered by Edwin H. Hall in 1879 [44]. When a current flows in a conductor placed in a perpendicular magnetic field H_z , electrons are pushed transversely by the Lorentz force and transverse voltage appears in the conductor. Following the first discovery in nonmagnetic conductors, he subsequently found that this effect becomes more than ten times larger when a conductor is a ferromagnet. Experimentalists empirically learned that in ferromagnets, the Hall resistivity ρ_{xy} first steeply rises then saturates at a high H_z . In 1893, Kundt [45] discovered in Fe, Co and Ni, this saturated value is roughly proportional to the magnetization M_z . This empirical finding was formulated by Pugh [46] in 1930 as

$$\rho_{xy} = R_0 H_z + R_s M_z, \quad (2.22)$$

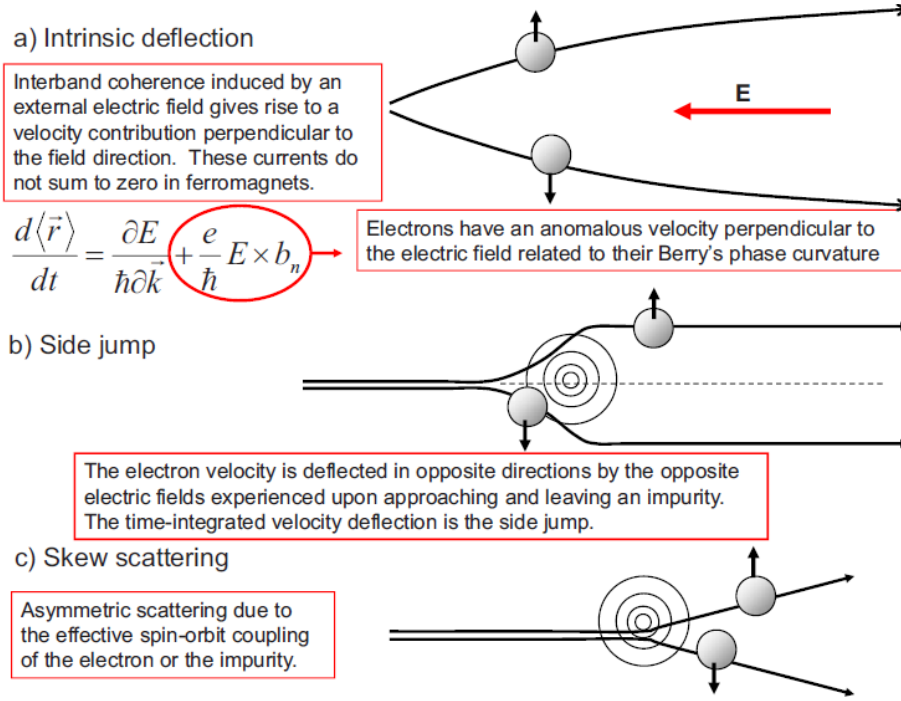


Figure 2.3: Schematic description of the mechanisms of the AHE cited from [53]. (a): Intrinsic contribution. Berry curvature derived from the band structure provides an emergent magnetic field, which generates the anomalous velocity perpendicular to the applied electric field. (b): Side-jump effect. When electrons enter into an impurity potential, they acquire the anomalous velocity from the potential perpendicular to their momentum, so that their trajectories are perpendicularly deflected. (c): Skew scattering mechanism. Spin-orbit interaction causes an asymmetric scattering according to the direction of spin of electrons.

where R_0 is the ordinary Hall coefficient, R_s is the anomalous Hall coefficient. The second term indicates that the spontaneous magnetization contributes to the Hall effect. While these remarkable effects were known before the birth of quantum mechanics, the microscopic theory, however, appeared in more than decades after the birth of the quantum mechanics.

Karplus and Luttinger [47] theoretically demonstrated in 1954 that the origin of the AHE is the anomalous velocity. When electrons in a solid are placed in an external electric field \mathbf{E} , they obtain an additional group velocity perpendicular to \mathbf{E} . Based on this idea, they showed that the Hall conductivity can be calculated as the sum of this anomalous velocity over all occupied band, and the sum becomes nonzero for ferromagnets. This effect is a consequence of a band structure, thus independent of scattering. ρ_{xy} is linked to σ_{xy} as $\rho_{xy} \sim \sigma_{xy} / \sigma_{xx}^2$ with the longitudinal conductivity σ_{xx} when $\sigma_{xy} \ll \sigma_{xx}$, this *intrinsic* contribution demands $\rho_{xy} \propto \rho_{xx}^2$. This intrinsic mechanism of the AHE was reformulated using the concept of the Berry phase afterward [48],

but it offered the idea which tells us that band structures are important components for the AHE.

The theory by Karplus and Luttinger is based on the assumption of a perfect crystal, and neglects effects from disorders. Smit [49, 50] and Berger [51, 52] on the other hand approached the problem from an imperfect crystal containing disorders. Smit investigated the influence of disorders in detail, and pointed out that the asymmetric scattering from impurities with SOI causes the AHE. This effect is dubbed as *skew scattering* and the relation $\rho_{xy} \propto \rho_{xx}$ was predicted. Berger, on the other hand, proposed that the main mechanism of the AHE is the *side jump* effect, where electrons acquire the anomalous velocity when they are scattered by impurities with SOI. One aspect for which the side jump effect is controversial is that this effect is independent of scattering strength or impurities concentration. Namely, $\sigma_{xy} \sim \rho_{xy}/\rho_{xx}^2 = \text{const.}$ Thus the relation between ρ_{xy} and ρ_{xx} becomes $\rho_{xy} \propto \rho_{xx}^2$, the same as that of the *intrinsic* contribution. Below, we briefly introduce each contribution by using some equations. To know more details about the AHE, the author recommend seeing the review [53].

(A) Intrinsic contribution

We here assume a two dimensional conductor. According to the perturbation theory, when an electric field $\mathbf{E} = (0, E)$ is applied, an eigenstate $|\alpha\rangle$ changes in a first order in E to

$$|\alpha'\rangle = |\alpha\rangle + \sum_{\beta \neq \alpha} \frac{\langle \beta | eEy | \alpha \rangle}{E_\alpha - E_\beta} |\beta\rangle, \quad (2.23)$$

where E_α and E_β is the eigenenergy for the state α and β , respectively. Then the expectation value of the current density to x , $\langle j_x \rangle$ can be calculated in a first order in E as

$$\langle j_x \rangle = \frac{1}{L^2} \sum_{\alpha} f(E_\alpha) \langle \alpha' | j_x | \alpha' \rangle = \frac{1}{L^2} \sum_{\alpha} f(E_\alpha) \sum_{\beta \neq \alpha} \frac{\langle \alpha | (-ev_x) | \beta \rangle \langle \beta | eEy | \alpha \rangle}{E_\alpha - E_\beta} + \text{c.c.}, \quad (2.24)$$

where $f(E)$ is the Fermi distribution function and L^2 is the size of the system. c. c. means the complex conjugate. Using the relation $\langle \beta | v_y | \alpha \rangle = \frac{-i}{\hbar} \langle \beta | [y, \mathcal{H}] | \alpha \rangle = \frac{-i}{\hbar} (E_\alpha - E_\beta) \langle \beta | y | \alpha \rangle$, we can write

$$\sigma_{xy} = \langle j_x \rangle / E = -ie^2 \hbar \frac{1}{L^2} \sum_{\alpha} f(E_\alpha) \sum_{\beta \neq \alpha} \frac{\langle \alpha | v_x | \beta \rangle \langle \beta | v_y | \alpha \rangle}{(E_\alpha - E_\beta)^2} + \text{c.c.} \quad (2.25)$$

We express the state α and β using the band component n and the Bloch wave number \mathbf{k} below. The velocity operator is defined as

$$\mathbf{v}(\mathbf{k}) = \frac{1}{i\hbar} [\mathbf{r}, \mathcal{H}(\mathbf{k})] = \frac{1}{\hbar} \nabla_{\mathbf{k}} \mathcal{H}(\mathbf{k}). \quad (2.26)$$

Therefore

$$\sigma_{xy} = -i \frac{e^2}{\hbar} \frac{1}{L^2} \sum_{\mathbf{k}} \sum_n f(E_n(\mathbf{k})) \sum_{n' \neq n} \left[\frac{\langle n, \mathbf{k} | \frac{\partial \mathcal{H}}{\partial k_x} | n', \mathbf{k} \rangle \langle n', \mathbf{k} | \frac{\partial \mathcal{H}}{\partial k_y} | n, \mathbf{k} \rangle}{(E_n(\mathbf{k}) - E_{n'}(\mathbf{k}))^2} - \text{c.c.} \right] \quad (2.27)$$

This equation reduces to

$$\sigma_{xy} = -\frac{e^2}{\hbar} \frac{1}{L^2} \sum_{\mathbf{k}} \sum_n f(E_n(\mathbf{k})) B_{n,z}(\mathbf{k}) = -\frac{e^2}{\hbar} \int \frac{d^2 k}{2\pi} \sum_n f(E_n(\mathbf{k})) B_{n,z}(\mathbf{k}), \quad (2.28)$$

where $B_{n,z}(\mathbf{k})$ is the Berry curvature (see Appendix A). Especially at $T = 0$,

$$\sigma_{xy} = -\frac{e^2}{\hbar} \sum_n \int_{E_n(\mathbf{k}) < E_F} \frac{d^2 k}{2\pi} B_{n,z}(\mathbf{k}). \quad (2.29)$$

This equation explicitly shows that the Hall conductivity is expressed as a sum of the Berry curvature for all bands below the Fermi energy. Therefore by combining with the band calculations [54, 55], one can precisely calculate the Hall conductivity for a perfect crystal.

(B) Skew scattering

The skew scattering contribution is proportional to the Bloch state transport lifetime, thus it becomes dominant for nearly perfect (moderately resistive) crystals. It is originated from the chiral nature of scattering by spin-orbit coupled impurities, and calculated using the semiclassical Boltzmann theory. Derivation of equations shown below is based on [35]. The steady state Boltzmann equation is written as

$$\mathbf{v}_{\mathbf{k}} \cdot \nabla f_{\mathbf{k}}^{\sigma} + \frac{e\mathbf{E}}{\hbar} \cdot \nabla_{\mathbf{k}} f_{\mathbf{k}}^{\sigma} = \left(\frac{\partial f_{\mathbf{k}}^{\sigma}}{\partial t} \right)_{\text{scatt}}. \quad (2.30)$$

Based on the Fermi's golden rule, the transition probability from the state (\mathbf{k}, σ) to (\mathbf{k}', σ') , $P_{\mathbf{k}'\mathbf{k}}^{\sigma'\sigma}$, can be calculated with the equation

$$P_{\mathbf{k}'\mathbf{k}}^{\sigma\sigma'} = \frac{2\pi}{\hbar} |\langle \mathbf{k}'\sigma' | \hat{T} | \mathbf{k}\sigma \rangle|^2 \delta(\xi_{\mathbf{k}} - \xi_{\mathbf{k}'}), \quad (2.31)$$

where the \hat{T} matrix is expressed as

$$\langle \mathbf{k}'\sigma' | \hat{T} | \mathbf{k}\sigma \rangle = \left[v_{\mathbf{k}'\mathbf{k}} + \sum_{\mathbf{q}} \frac{V_{\mathbf{k}'\mathbf{q}} V_{\mathbf{q}\mathbf{k}}}{\xi_{\mathbf{k}} - \xi_{\mathbf{q}} + i\delta} \right] \delta_{\sigma'\sigma} + i\eta_{\text{SO}} V_{\mathbf{k}'\mathbf{k}} (\mathbf{k} \times \mathbf{k}') \cdot \sigma_{\sigma'\sigma}. \quad (2.32)$$

The rhs of (2.31) is expressed as

$$\left(\frac{\partial f_{\mathbf{k}}^{\sigma}}{\partial t} \right)_{\text{scatt}} = \sum_{\mathbf{k}'\sigma'} [P_{\mathbf{k}\mathbf{k}'}^{\sigma\sigma'} f_{\mathbf{k}'}^{\sigma'} - P_{\mathbf{k}'\mathbf{k}}^{\sigma'\sigma} f_{\mathbf{k}}^{\sigma}] = \sum_{\mathbf{k}'\sigma'} P_{\mathbf{k}'\mathbf{k}}^{\sigma'\sigma(1)} (f_{\mathbf{k}'}^{\sigma'} - f_{\mathbf{k}}^{\sigma}) + \sum_{\mathbf{k}'\sigma'} P_{\mathbf{k}'\mathbf{k}}^{\sigma'\sigma(2)} (f_{\mathbf{k}'}^{\sigma'} + f_{\mathbf{k}}^{\sigma}). \quad (2.33)$$

The contribution from the skew scattering is included in the term $P_{\mathbf{k}'\mathbf{k}}^{\sigma'\sigma(2)}$, which is explicitly written as

$$P_{\mathbf{k}'\mathbf{k}}^{\sigma'\sigma(2)} = \frac{(2\pi)^2}{\hbar} n_{\text{imp}} V_{\text{imp}}^3 N(0) \times [\eta_{\text{SO}}(\mathbf{k}' \times \mathbf{k}) \cdot \sigma_{\sigma\sigma'}] \delta_{\sigma\sigma'} \delta(\xi_{\mathbf{k}'} - \xi_{\mathbf{k}}), \quad (2.34)$$

whereas $P_{\mathbf{k}'\mathbf{k}}^{\sigma'\sigma(1)}$ is related to the symmetric scattering and the second order in V_{imp} and expressed as

$$P_{\mathbf{k}'\mathbf{k}}^{\sigma'\sigma(1)} = \frac{2\pi}{\hbar} n_{\text{imp}} V_{\text{imp}}^2 (\delta_{\sigma\sigma'} + |\eta_{\text{SO}}(\mathbf{k}' \times \mathbf{k}) \cdot \sigma_{\sigma\sigma'}|^2) \delta(\xi_{\mathbf{k}'} - \xi_{\mathbf{k}}). \quad (2.35)$$

To solve the Boltzmann equation, we express $f_{\mathbf{k}}^{\sigma}$ with three terms as

$$f_{\mathbf{k}}^{\sigma} = f_{k0}^{\sigma} + g_{\mathbf{k}}^{\sigma} + h_{\mathbf{k}}^{\sigma}, \quad (2.36)$$

where $f_{k0}^{\sigma} = \int f_{\mathbf{k}}^{\sigma} / (4\pi)$, the average of $f_{\mathbf{k}}^{\sigma}$ over the solid angle, $g_{\mathbf{k}}^{\sigma(1)}$ and $g_{\mathbf{k}}^{\sigma(2)}$ are directional distribution functions and meet the relation $\int g_{\mathbf{k}}^{\sigma} d\Omega_{\mathbf{k}} = 0$.

The first term in (2.33) is written as

$$\sum_{\mathbf{k}'\sigma'} P_{\mathbf{k}'\mathbf{k}}^{\sigma'\sigma(1)} (f_{\mathbf{k}'}^{\sigma'} - f_{\mathbf{k}}^{\sigma}) = -\frac{g_{\mathbf{k}}^{\sigma}}{\tau} - \frac{f_{k0}^{\sigma} - f_{k0}^{-\sigma}}{\tau_{\text{sf}}} \quad (2.37)$$

where,

$$\frac{1}{\tau} = \frac{1}{\tau_0} \left(1 + \frac{2\eta_{\text{SO}}^2}{3}\right) \quad (2.38)$$

$$\frac{1}{\tau_{\text{sf}}} = \frac{\eta_{\text{SO}}^2}{3\tau_0} (1 + \cos^2 \theta) \quad (2.39)$$

with the θ as an angle between \mathbf{k} and x axis. Then (2.30) becomes

$$\mathbf{v}_{\mathbf{k}} \cdot \frac{\partial f_{\mathbf{k}}^{\sigma}}{\partial \mathbf{r}} + \frac{e\mathbf{E}}{\hbar} \cdot \frac{\partial f_{\mathbf{k}}^{\sigma}}{\partial \mathbf{k}} = -\frac{g_{\mathbf{k}}^{\sigma}}{\tau} - \frac{f_{k0}^{\sigma} - f_{k0}^{-\sigma}}{\tau_{\text{sf}}}. \quad (2.40)$$

Generically $\tau \ll \tau_{\text{sf}}$. Therefore we neglect the second term of the rhs in (2.40), then

$$g_{\mathbf{k}}^{\sigma} \sim \tau \left(\mathbf{v}_{\mathbf{k}} \cdot \nabla + \frac{e\mathbf{E}}{\hbar} \cdot \nabla_{\mathbf{k}} \right) f_{k0}^{\sigma}. \quad (2.41)$$

The distribution function f_{k0}^{σ} can be written with the Fermi energy $\varepsilon_{\text{F}}^{\sigma}(\mathbf{r}) = \varepsilon_{\text{F}} + \sigma\delta\varepsilon_{\text{F}}(\mathbf{r})$ as

$$f_{k0}^{\sigma} = f_0(\xi_{\mathbf{k}} - \sigma\delta\varepsilon_{\text{F}}) \sim f_0(\xi_{\mathbf{k}}) - \sigma \frac{\partial f_0(\xi_{\mathbf{k}})}{\partial \xi_{\mathbf{k}}} \delta\varepsilon_{\text{F}}(\mathbf{r}). \quad (2.42)$$

Substituting (2.42) into (2.41), we obtain

$$g_{\mathbf{k}}^{\sigma} \sim \tau \frac{\partial f_0(\xi_{\mathbf{k}})}{\partial \xi_{\mathbf{k}}} \mathbf{v}_{\mathbf{k}} \cdot \nabla \mu_{\text{N}}^{\sigma}(\mathbf{r}), \quad (2.43)$$

where

$$\mu_{\text{N}}^{\sigma}(\mathbf{r}) = \varepsilon_{\text{F}} + e\phi + \sigma\delta\varepsilon_{\text{F}}(\mathbf{r}) \quad (2.44)$$

is the electrochemical potential.

The second-order term in the Boltzmann equation is expressed as

$$\sum_{\mathbf{k}'\sigma'} [P_{\mathbf{k}\mathbf{k}'}^{\sigma'\sigma(1)}(h_{\mathbf{k}}^{\sigma} - h_{\mathbf{k}'}^{\sigma'}) - P_{\mathbf{k}\mathbf{k}'}^{\sigma'\sigma(2)}(g_{\mathbf{k}}^{\sigma} + g_{\mathbf{k}'}^{\sigma'})] = 0. \quad (2.45)$$

Using (2.35), (2.34) and (2.43), $h_{\mathbf{k}}^{\sigma}$ term becomes

$$h_{\mathbf{k}}^{\sigma} = -\alpha_{\text{H}}^{\text{Skew}}\tau \frac{\partial f_0(\xi_{\mathbf{k}})}{\partial \xi_{\mathbf{k}}} (\sigma_{\sigma\sigma} \times \mathbf{v}_{\mathbf{k}}) \times \nabla \mu_{\text{N}}^{\sigma}(\mathbf{r}). \quad (2.46)$$

with

$$\alpha_{\text{H}}^{\text{Skew}} = \frac{2\pi}{3} \eta_{\text{SO}} N(0) V_{\text{imp}}. \quad (2.47)$$

Substituting the preceding results (2.43) and (2.46) into (2.36), we obtain

$$f_{\mathbf{k}}^{\sigma} \approx f_0(\xi_{\mathbf{k}}) - \sigma \frac{\partial f_0(\xi_{\mathbf{k}})}{\partial \xi_{\mathbf{k}}} \delta \mu_{\text{N}}(\mathbf{r}) + \tau \frac{\partial f_0(\xi_{\mathbf{k}})}{\partial \xi_{\mathbf{k}}} [\mathbf{v}_{\mathbf{k}} - \alpha_{\text{H}}^{\text{Skew}} \sigma_{\sigma\sigma} \times \mathbf{v}_{\mathbf{k}}] \cdot \nabla \mu_{\text{N}}^{\sigma}(\mathbf{r}). \quad (2.48)$$

The charge current density and the spin current density can be expressed using the Fermi distribution function as

$$\mathbf{J}_{\mathbf{q}} = e \sum_{\mathbf{k}} \frac{\hbar \mathbf{k}}{m} [f_{\mathbf{k}\uparrow} + f_{\mathbf{k}\downarrow}]. \quad (2.49)$$

$$\mathbf{J}_{\mathbf{s}} = e \sum_{\mathbf{k}} \frac{\hbar \mathbf{k}}{m} [f_{\mathbf{k}\uparrow} - f_{\mathbf{k}\downarrow}]. \quad (2.50)$$

Substituting (2.48) into (2.49) and (2.50), we obtain

$$\mathbf{J}_{\mathbf{q}} = \mathbf{j}_{\mathbf{q}} + \alpha_{\text{H}}^{\text{Skew}} [\mathbf{z} \times \mathbf{j}_{\mathbf{s}}] \quad (2.51)$$

and

$$\mathbf{J}_{\mathbf{s}} = \mathbf{j}_{\mathbf{s}} + \alpha_{\text{H}}^{\text{Skew}} [\mathbf{z} \times \mathbf{j}_{\mathbf{q}}], \quad (2.52)$$

with

$$\mathbf{j}_{\mathbf{q}} = \sigma_{\text{N}} \mathbf{E} \quad (2.53)$$

and

$$\mathbf{j}_{\mathbf{s}} = -\frac{\sigma_{\text{N}}}{e} \nabla \delta \mu_{\text{N}}, \quad (2.54)$$

where $\sigma_{\text{N}} = 2e^2 N(0)D$ with the density of states at the Fermi level $N(0)$ and the diffusion constant D . In (2.51) and (2.52) you can easily find in the second term the additional components which derive from the spin-charge conversion via the skew scattering contribution.

(C) Side jump

The side-jump contribution derives from the anomalous velocity term. In the presence of an impurity potential $V(\mathbf{r})$, this potential creates an electric field $\mathbf{E} = -\nabla V(\mathbf{r})/e$. An electron with momentum \mathbf{p} feels an effective magnetic field $\mathbf{B}_{\text{eff}} = -(1/mc)\mathbf{p} \times \mathbf{E}$. Therefore an effective spin-orbit coupling is generated through this effect and described as

$$V_{\text{SO}} = -\frac{1}{2}\mu_B\sigma \cdot \mathbf{B}_{\text{eff}} = \eta_{\text{SO}}\sigma \cdot [\nabla V(\mathbf{r}) \times \frac{\nabla}{i}], \quad (2.55)$$

where $\eta_{\text{SO}} = \hbar^2/(4m^2c^2)$. Therefore the total potential $U(\mathbf{r})$ is the sum of the impurity potential $V(\mathbf{r})$ and the spin-orbit potential $V_{\text{SO}}(\mathbf{r})$, $U(\mathbf{r}) = V(\mathbf{r}) + V_{\text{SO}}(\mathbf{r})$. The one-electron Hamiltonian with the potential $U(\mathbf{r})$ is expressed in the momentum space as

$$\mathcal{H} = \sum_{\mathbf{k}\sigma} \xi_{\mathbf{k}} a_{\mathbf{k}\sigma}^\dagger a_{\mathbf{k}\sigma} + \sum_{\mathbf{k}, \mathbf{k}'} \sum_{\sigma, \sigma'} U_{\mathbf{k}', \mathbf{k}}^{\sigma' \sigma} a_{\mathbf{k}' \sigma'}^\dagger a_{\mathbf{k} \sigma}, \quad (2.56)$$

where

$$U_{\mathbf{k}' \mathbf{k}}^{\sigma' \sigma} = V_{\text{imp}} [\delta_{\sigma' \sigma} + i\eta_{\text{SO}} \sigma_{\sigma' \sigma} \cdot (\mathbf{k} \times \mathbf{k}')] \sum_i e^{i(\mathbf{k} - \mathbf{k}') \cdot \mathbf{r}_i}. \quad (2.57)$$

In the above equation we assume that the impurity potential is delta-function like: $V(\mathbf{r}) \approx V_{\text{imp}} \sum_i \delta(\mathbf{r} - \mathbf{r}_i)$. The velocity of electron is calculated using the relation $\hat{\mathbf{v}} = d\mathbf{r}/dt = (1/i\hbar)[\mathbf{r}, \mathcal{H}]$ between the scattering state $|\mathbf{k}^+ \sigma\rangle$. In the first order Born approximation, $|\mathbf{k}^+ \sigma\rangle$ can be expressed as

$$|\mathbf{k}^+, \sigma\rangle = |\mathbf{k}, \sigma\rangle + \sum_{\mathbf{k}'} |\mathbf{k}', \sigma\rangle \frac{V_{\text{imp}} \sum_i e^{i(\mathbf{k} - \mathbf{k}') \cdot \mathbf{r}_i}}{\xi_{\mathbf{k}} - \xi_{\mathbf{k}'} + i\delta}. \quad (2.58)$$

Using the expression of the scattering state, the matrix element between the scattering state is described as

$$\mathbf{v}_{\mathbf{k}}^\sigma = \langle \mathbf{k}^+, \sigma | \frac{1}{i\hbar} [\mathbf{r}, \mathcal{H}] | \mathbf{k}^+, \sigma \rangle = \frac{\hbar \mathbf{k}}{m} + \omega_{\mathbf{k}}^\sigma, \quad (2.59)$$

where

$$\omega_{\mathbf{k}}^\sigma = \frac{\eta_{\text{SO}}}{\hbar} \langle \mathbf{k}^+, \sigma | \sigma \times \nabla V | \mathbf{k}^+, \sigma \rangle. \quad (2.60)$$

This $\omega_{\mathbf{k}}^\sigma$ term is called the anomalous velocity, and can be expressed as [35]

$$\omega_{\mathbf{k}}^\sigma = \alpha_{\text{H}}^{\text{sj}} \left[\sigma_{\sigma\sigma} \times \frac{\hbar \mathbf{k}}{m} \right] \quad (2.61)$$

with

$$\alpha_{\text{H}}^{\text{sj}} = \frac{k_{\text{F}} \eta_{\text{SO}}}{l_{\text{imp}}}, \quad (2.62)$$

where l_{imp} is the mean-free path. The anomalous velocity appears in the current operator as

$$\hat{\mathbf{J}}_{\sigma} = e \sum_{\mathbf{k}} \left[\frac{\hbar \mathbf{k}}{m} + \omega_{\mathbf{k}}^{\sigma} \right] a_{\mathbf{k}\sigma}^{\dagger} a_{\mathbf{k}\sigma}. \quad (2.63)$$

The charge current density $\mathbf{J}_{\mathbf{q}}$ and the spin current density $\mathbf{J}_{\mathbf{s}}$ are expressed as

$$\mathbf{J}_{\mathbf{q}} = \langle \hat{\mathbf{J}}_{\uparrow} + \hat{\mathbf{J}}_{\downarrow} \rangle \quad (2.64)$$

$$\mathbf{J}_{\mathbf{s}} = \langle \hat{\mathbf{J}}_{\uparrow} - \hat{\mathbf{J}}_{\downarrow} \rangle, \quad (2.65)$$

where

$$\langle A \rangle = \text{Tr}[\rho A_{\text{H}}] \quad (2.66)$$

with

$$\rho \equiv \frac{\exp[-\beta(H - \mu N)]}{\text{Tr}[\exp[-\beta(H - \mu N)]]}, \quad (2.67)$$

where A_{H} is the Heisenberg's expression. Thus we can explicitly write $\mathbf{J}_{\mathbf{q}}$ and $\mathbf{J}_{\mathbf{s}}$:

$$\mathbf{J}_{\mathbf{q}} = \mathbf{J}'_{\mathbf{q}} + \alpha_{\text{H}}^{\text{sj}}[\hat{\mathbf{z}} \times \mathbf{J}'_{\mathbf{s}}] \quad (2.68)$$

$$\mathbf{J}_{\mathbf{s}} = \mathbf{J}'_{\mathbf{s}} + \alpha_{\text{H}}^{\text{sj}}[\hat{\mathbf{z}} \times \mathbf{J}'_{\mathbf{q}}] \quad (2.69)$$

where

$$\mathbf{J}'_{\mathbf{q}} = e \sum_{\mathbf{k}} \frac{\hbar \mathbf{k}}{m} [f_{\mathbf{k}\uparrow} + f_{\mathbf{k}\downarrow}], \quad (2.70)$$

$$\mathbf{J}'_{\mathbf{s}} = e \sum_{\mathbf{k}} \frac{\hbar \mathbf{k}}{m} [f_{\mathbf{k}\uparrow} - f_{\mathbf{k}\downarrow}], \quad (2.71)$$

where $f_{\mathbf{k}\sigma} = \langle a_{\mathbf{k}\sigma}^{\dagger} a_{\mathbf{k}\sigma} \rangle$ is the distribution function of an electron with energy $\xi_{\mathbf{k}}$ and spin σ (at equilibrium, equivalent to the Fermi distribution function). The second term in (2.68) and (2.69) is originated from the spin-charge current conversion via the side-jump contribution.

2.3 Superconductivity

2.3.1 The BCS theory

One of the most important theories to describe superconductivity is the Bardeen-Cooper-Schrieffer(BCS) theory [56]. The basic idea is relevant to Bose-Einstein condensation of electrons' pairs, suggested by Cooper in 1956 [57]. He theoretically showed that even a weak attraction could bind pairs of electrons. This means that with some weak attraction the Fermi sea becomes unstable and the ground state becomes different from that of ordinary metals. Therefore redistribution can occur, which is energetically favorable considering the attractive potential among electrons. In the presence

of correlation between electrons, Hamiltonian is generally described as

$$\mathcal{H} = \sum_{\mathbf{k}\sigma} \epsilon_{\mathbf{k}} a_{\mathbf{k}\sigma}^{\dagger} a_{\mathbf{k}\sigma} + \frac{1}{2} \sum_{\mathbf{k}\mathbf{k}'\mathbf{q}\sigma\sigma'} V_{\mathbf{k}\mathbf{k}'\mathbf{q}\sigma\sigma'} a_{\mathbf{k}-\mathbf{q}\sigma}^{\dagger} a_{\mathbf{k}'+\mathbf{q}\sigma'}^{\dagger} a_{\mathbf{k}'\sigma'} a_{\mathbf{k}\sigma}. \quad (2.72)$$

In the normal state, the ground state is the state in which electrons are filled in Fermi sphere. This is described as

$$|\psi_{g0}\rangle = \prod_{|\mathbf{k}| < k_F} a_{\mathbf{k}\uparrow}^{\dagger} a_{\mathbf{k}\downarrow}^{\dagger} |\phi_{n0}\rangle. \quad (2.73)$$

Cooper assumed no kinetic energies of pairs (no momenta of each pair) as a ground state. Thus by transforming (2.73), a trial function of the BCS ground state is represented as

$$|\psi_g\rangle = \prod_{\mathbf{k}} (|u_{\mathbf{k}}| + |v_{\mathbf{k}}| e^{i\varphi} a_{\mathbf{k}\uparrow}^{\dagger} a_{-\mathbf{k}\downarrow}^{\dagger}) |\phi_0\rangle, \quad (2.74)$$

where $|\phi_0\rangle$ is the vacuum state. In this state the number of electrons (N) is undetermined and as a result a finite phase $e^{i\varphi}$ is added to $|v_{\mathbf{k}}|$. This phase is relevant to the uncertainty principle $\Delta N \Delta \varphi > 1$. For the normalization, the variable coefficients $|u_{\mathbf{k}}|$ and $|v_{\mathbf{k}}|$ fulfill $|u_{\mathbf{k}}|^2 + |v_{\mathbf{k}}|^2 = 1$. In order to determine the ground state, we transform the Hamiltonian (2.72) into the equation as follows

$$\mathcal{H} = \sum_{\mathbf{k}\sigma} \epsilon_{\mathbf{k}} a_{\mathbf{k}\sigma}^{\dagger} a_{\mathbf{k}\sigma} + \sum_{\mathbf{k}\mathbf{k}'} V_{\mathbf{k}\mathbf{k}'} a_{\mathbf{k}\uparrow}^{\dagger} a_{-\mathbf{k}\downarrow}^{\dagger} a_{-\mathbf{k}'\downarrow} a_{\mathbf{k}'\uparrow}. \quad (2.75)$$

In the equation (2.75) we ignore many other terms which involve electrons which do not form a pair composed of two electrons with opposite momentum, as $(\mathbf{k}, -\mathbf{k})$ because they do not contribute to the condensation. We substitute a transformation of $a_{-\mathbf{k}\downarrow} a_{\mathbf{k}\uparrow} = \langle a_{-\mathbf{k}\downarrow} a_{\mathbf{k}\uparrow} \rangle + a_{-\mathbf{k}\downarrow} a_{\mathbf{k}\uparrow} - \langle a_{-\mathbf{k}\downarrow} a_{\mathbf{k}\uparrow} \rangle$ into (2.75), and ignore second order term of the deviation from the average value ($a_{-\mathbf{k}\downarrow} a_{\mathbf{k}\uparrow} - \langle a_{-\mathbf{k}\downarrow} a_{\mathbf{k}\uparrow} \rangle$), then we obtain

$$\mathcal{H} = \sum_{\mathbf{k}\sigma} \epsilon_{\mathbf{k}} a_{\mathbf{k}\sigma}^{\dagger} a_{\mathbf{k}\sigma} + \sum_{\mathbf{k}\mathbf{k}'} V_{\mathbf{k}\mathbf{k}'} \{ a_{\mathbf{k}\uparrow}^{\dagger} a_{-\mathbf{k}\downarrow}^{\dagger} \langle a_{\mathbf{k}'\downarrow} a_{-\mathbf{k}'\uparrow} \rangle + \langle a_{\mathbf{k}\uparrow}^{\dagger} a_{-\mathbf{k}\downarrow}^{\dagger} \rangle a_{-\mathbf{k}\downarrow} a_{\mathbf{k}\uparrow} - \langle a_{\mathbf{k}\uparrow}^{\dagger} a_{-\mathbf{k}\downarrow}^{\dagger} \rangle \langle a_{\mathbf{k}'\downarrow} a_{-\mathbf{k}'\uparrow} \rangle \}. \quad (2.76)$$

Next we define the gap potential $\Delta_{\mathbf{k}}$ as $\Delta_{\mathbf{k}} = \sum_{\mathbf{k}'} V_{\mathbf{k}\mathbf{k}'} \langle a_{-\mathbf{k}'\downarrow} a_{\mathbf{k}'\uparrow} \rangle$. Then (2.76) becomes

$$\mathcal{H} = \sum_{\mathbf{k}\sigma} \epsilon_{\mathbf{k}} a_{\mathbf{k}\sigma}^{\dagger} a_{\mathbf{k}\sigma} - \sum_{\mathbf{k}} \{ \Delta_{\mathbf{k}} a_{\mathbf{k}\uparrow}^{\dagger} a_{-\mathbf{k}\downarrow}^{\dagger} + \Delta_{\mathbf{k}}^* a_{-\mathbf{k}\downarrow} a_{\mathbf{k}\uparrow} - \Delta_{\mathbf{k}} \langle a_{\mathbf{k}\uparrow}^{\dagger} a_{-\mathbf{k}\downarrow}^{\dagger} \rangle \}. \quad (2.77)$$

(2.77) can be diagonalized by using the Bogoliubov transformation:

$$a_{\mathbf{k}\uparrow} = u_{\mathbf{k}}^* \gamma_{\mathbf{k}0} + v_{\mathbf{k}} \gamma_{\mathbf{k}1}^{\dagger}, \quad (2.78)$$

$$a_{-\mathbf{k}\downarrow}^{\dagger} = -v_{\mathbf{k}}^{\dagger} \gamma_{\mathbf{k}0} + u_{\mathbf{k}} \gamma_{\mathbf{k}1}^{\dagger}, \quad (2.79)$$

where 0 and 1 are the spin index. After substitution, one finally obtains

$$\mathcal{H} = \sum_{\mathbf{k}} (\epsilon_{\mathbf{k}} - E_{\mathbf{k}} + \Delta_{\mathbf{k}} \langle a_{-\mathbf{k}\downarrow} a_{\mathbf{k}\uparrow} \rangle) + \sum_{\mathbf{k}} E_{\mathbf{k}} (\gamma_{\mathbf{k}0}^\dagger \gamma_{\mathbf{k}0} + \gamma_{\mathbf{k}1}^\dagger \gamma_{\mathbf{k}1}). \quad (2.80)$$

The first term is constant, and the second term represents the excitation from the ground state by using the Fermionic creation/annihilation operator of quasiparticles. Therefore, the BCS ground state can be regarded as a vacuum state for the quasiparticles. Here $E_{\mathbf{k}} = \sqrt{\xi_{\mathbf{k}}^2 + \Delta_{\mathbf{k}}^2}$ represents excitation spectrum of quasiparticles. Thus there is a finite gap $\Delta_{\mathbf{k}}$ for the excitation of superconductors.

2.3.2 Spin transport in superconductors

The most distinctive feature for spin transport in superconductors is that since the single particle excitation is described by the Bogoliubov transformation (2.78) and (2.79), spin transport is mediated by these Bogoliubov quasiparticles rather than electrons unless Cooper pairs are in the spin-triplet states. As seen in the Bogoliubov transformation, the Bogoliubov quasiparticles are regarded as a superposition of electron-like and hole-like excitations, and charge of the Bogoliubov quasiparticles can be an intermediate value between $-e$ to $+e$. At equilibrium, the number of quasiparticles on the electron-line and hole-like branch is the same. However, when electrons are injected externally into the superconductor, for example, the system is brought into nonequilibrium state and the number of quasiparticles on each branch becomes different (Fig. 2.4(a)). This nonequilibrium situation causes the charge imbalance (CI) effect, which relaxes in a certain time scale (τ_Q) or length scale (λ_Q). The CI effect is found to be important in Chapter 4 and Chapter 5.

In addition to unique properties like the CI effect of the Bogoliubov quasiparticles, the superconducting gap also plays an important role for spin transport in superconductors. As discussed in [28] or [29], based on the semiconductor model the resistivity of quasiparticles is proportional to $(f_0(\Delta))^{-1}$, where $f_0(E) = (\exp(E/k_B T) + 1)^{-1}$ is the Fermi distribution function. Due to the energy gap, the number of quasiparticles is decreasing with decreasing temperature. This effect is reflected not only to charge transport properties but also spin transport properties, as we will discuss in Chapter 5.

2.3.3 Odd-frequency spin-triplet superconductors

Interface between superconductors and other materials is rich of novel phenomena and has been a main subject in condensed matter physics. Especially, interface between a superconductor and a ferromagnet is of great interest. In most of the typical superconductors, electrons pair in the spin-singlet state. On the other hand, in ferromagnets

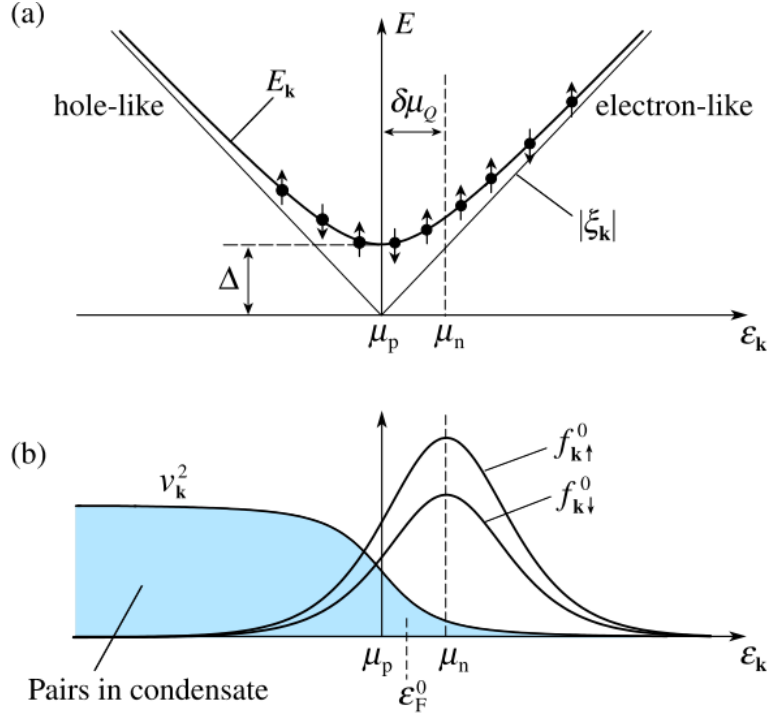


Figure 2.4: (a): Branch imbalance in electron-like and hole-like excitations. Spin of quasiparticles is also explicitly described. (b): Distribution function of upspin ($f_{k\uparrow}^0$), downspin electrons ($f_{k\downarrow}^0$) and condensate (x_k^2) [30].

an exchange interaction favors parallel spin orientation between electrons. Thus when a superconductor is in contact with a ferromagnet, competition between superconductivity and ferromagnetism brings about interesting physics. As described above, at the interface between a superconductor and a nonmagnetic normal metal Cooper pairs leak into the normal metal, and this is called the proximity effect. The same effect occurs even for the interface between a superconductor and a ferromagnet, but due to the exchange field in the ferromagnet, Cooper pairs are destroyed in much shorter length scale in ferromagnets than in nonmagnets.

However, there are two ways for the spin-singlet Cooper pairs to survive in ferromagnets. One is to acquire an additional momentum. For a Cooper pair, one electron with a momentum \mathbf{k}_F and \uparrow , and one electron with $-\mathbf{k}_F$ and \downarrow form a pair. We here explicitly write $\mathbf{k}_\uparrow = \mathbf{k}_F$ and $\mathbf{k}_\downarrow = -\mathbf{k}_F$. We assume a plane wave for an orbital part of the electron's wave function and then the orbital part of the two-electrons' wave function $\Psi_{\mathbf{k}_\uparrow, \mathbf{k}_\downarrow}(\mathbf{r}_1, \mathbf{r}_2)$ can be written as

$$\Psi_{\mathbf{k}_\uparrow, \mathbf{k}_\downarrow}(\mathbf{r}_1, \mathbf{r}_2) = \frac{1}{\sqrt{V}}(e^{i\mathbf{k}_F \cdot \mathbf{r}_1} e^{-i\mathbf{k}_F \cdot \mathbf{r}_2} + e^{-i\mathbf{k}_F \cdot \mathbf{r}_1} e^{i\mathbf{k}_F \cdot \mathbf{r}_2}). \quad (2.81)$$

When there is an exchange field \mathbf{E}_{ex} , each electron acquire an additional momentum

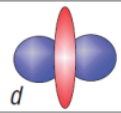
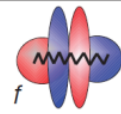
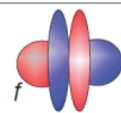
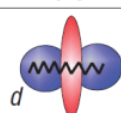
Spin	Frequency	Momentum		
Singlet (odd)	Even	Even		
$\uparrow\downarrow - \downarrow\uparrow$	Odd	Odd		
$\uparrow\uparrow \quad \downarrow\downarrow$	Even	Odd		
Triplet (even)	Odd	Even		
$\uparrow\downarrow + \downarrow\uparrow$				

Figure 2.5: Allowed symmetries of two electrons' wave functions.

\mathbf{Q} whose magnitude Q is written as

$$Q = \frac{E_{\text{ex}}}{\hbar v_F}, \quad (2.82)$$

where v_F is the Fermi velocity. Therefore the wave vector for upspin and downspin electrons become

$$\mathbf{k}_\uparrow = \mathbf{k}_F + \mathbf{Q}, \quad (2.83)$$

$$\mathbf{k}_\downarrow = -\mathbf{k}_F + \mathbf{Q}. \quad (2.84)$$

Then in this regime the orbital part of the two electrons' wave function $\tilde{\Psi}_{\mathbf{k}_\uparrow, \mathbf{k}_\downarrow}(\mathbf{r}_1, \mathbf{r}_2)$ is

$$\tilde{\Psi}_{\mathbf{k}_\uparrow, \mathbf{k}_\downarrow}(\mathbf{r}_1, \mathbf{r}_2) = \frac{1}{\sqrt{V}} (e^{i\mathbf{k}_F \cdot \mathbf{r}_1} e^{-i\mathbf{k}_F \cdot \mathbf{r}_2} + e^{-i\mathbf{k}_F \cdot \mathbf{r}_1} e^{i\mathbf{k}_F \cdot \mathbf{r}_2}) e^{2i\mathbf{Q} \cdot \mathbf{R}}, \quad (2.85)$$

where $\mathbf{R} = (\mathbf{r}_1 + \mathbf{r}_2)/2$ is the center of mass coordinate. Thus according to \mathbf{R} , the pair amplitude oscillates. This spatially oscillating state of the pair amplitude is called the FFLO (Fulde, Ferrell, Larkin and Ovchinnikov) state [58, 59]. The oscillation can be regarded as a phase change of the macroscopic wave function of Cooper pair, and negative $\tilde{\Psi}$ is equal to π phase shift of the wave function. Transition into the state with π phase shift is called the $0-\pi$ transition, which has been experimentally demonstrated by Ryazanov *et al.* [60, 61, 62]. The other way is to flip spins of electrons to align parallel. Spin-triplet pairing of Cooper pairs is allowed under the consideration of the Pauli's exclusion principle. We show in Fig. 2.5 the allowed symmetry components in the spin, frequency and momentum space [63]. Spin-triplet states have three components in the spin space ($S = 1, m = 0, \pm 1$). Spin-triplet pairing is proposed for two

systems, Sr_2RuO_4 and heavy Fermions such as UPt_3 . In these systems, symmetry in momentum space is odd, thus time-reversal symmetry is even. On the other hand, spin-triplet pairing of Cooper pairs whose symmetry does not exist in nature has been proposed at the superconductor/strong ferromagnet interface [64, 65]. This pairing has s -wave symmetry in the momentum space and is odd in the frequency space. While due to the Anderson's theorem Cooper pairs with symmetry other than s -wave one is fragile to disorders, this odd frequency pairing is robust against disorders. Following the theoretical predictions, Keizer *et al* [66] experimentally demonstrated the long-range supercurrent through the half-metallic CrO_2 Josephson junction. This first report has triggered many theoretical and experimental studies. We will introduce them in Chapter 6.

2.3.4 Spin-triplet supercurrents and spintronics

While many studies have been carried out on spin-triplet Cooper pairs at the superconductor/strong ferromagnet interface, in the experimental point of view, direct observation of spin-polarization of supercurrents is still lacking. In the previous studies, supercurrents which survive in a much longer length than that of spin-singlet ones are an only evidence of the spin-triplet pairing of Cooper pairs. To clarify spin polarization of supercurrents, technique familiar in spintronics might be useful [67]. Spin-transfer torque by spin-triplet supercurrents is also of great interest and studied theoretically [68, 69] Spintronics with spin-triplet supercurrents is a promising field worthy to explore.

Chapter 3

Experimental methods

3.1 Sample fabrication

In this chapter we briefly describe the details of the sample fabrication and measurement processes.

3.1.1 Electron-beam lithography and Liftoff process

In our study we use nanometre-scale devices and to fabricate these devices nanofabrication techniques are necessary. The electron beam (EB) lithography is one of the indispensable tools for making such nanometre-scale devices. We will show below how to make devices using the EB lithography.

We first coat a substrate with a resist using typical spin coater. We use different kinds of resist. We first introduce positive resists: for the EB evaporation or thermal evaporation, the polymethyl-methacrylate (PMMA, molecular weight 950, anisole 8%, made by Microchem Co. Ltd.). For sputtering, we use the ZEP520A. To perform the shadow evaporation, a double-layer resist is necessary. We combine the PMMA with the methacrylate (MMA) resist. Substrates in our studies are all thermally oxidized silicon (Si/SiO₂) substrates. Thickness of SiO₂ is estimated to be 300 nm.

After coating the resist, we perform prebaking. Conditions for prebaking is shown in Table 3.1.1.

We also show conditions for negative resists. We first coat a substrate with HMDS. After baking the substrate, we then coat it with ma-N2405 negative resist. Subsequently, we perform prebaking. Conditions for spin coating and prebaking is shown in Table 3.1.1.

Next step is the EB lithography. We use the "Elionix6600 electron beam lithography system" for the EB lithography with the acceleration voltage of 75 kV. We show several conditions for the EB lithography in Table 3.1.1.

After the lithography, we develop the resist. A developer for the PMMA and MMA

Resist	Annealing time/Temperature
ZEP	6 min/from RT to 180 °C
PMMA	5 min/180 °C
MMA in PMMA/MMA	3 min/180 °C
PMMA in PMMA/MMA	5 min/180 °C

Table 3.1: Prebaking conditions for positive resists

Resist	Spin coating condition	Prebaking condition
HMDS	1000 rpm, 5 sec+ 5000 rpm, 40 sec	80° 5 min
ma-N2405	1000 rpm, 5 sec + 3000 rpm, 50 sec	90° 1 min

Table 3.2: Conditions for preparing negative resists

is composed of the methyl-isobutyl-ketone (MIBK) and isopropyl alcohol (IPA) with the ratio of 4:1, whereas the pentyl-acetate is used for ZEP520A. The developing time for each resist is 30 seconds. For rinse, IPA is used for all resists.

Next process is materials evaporation. In our study, we deposit Py, Co, Cu, Nb, NbN, Bi and Pb. Py, Co and Nb are deposited through the EB evaporation technique. For Cu, Bi and Pb, we use the thermal evaporation technique. Materials are evaporated normal to the substrate except in the case of the shadow evaporation. See Table 3.1.1 for checking the deposition condition and the thickness of each material.

NbN layer is fabricated by sputtering. In the sputtering system base pressure was kept less than 8.0×10^{-5} Pa. The NbN layers were deposited by reactive DC-magnetron sputtering in a mixture of Ar and N₂ gases.

After the deposition process the resist is lift off in an organic solvent. In Table 3.5 we show an appropriate solvent for each resist.

Resist	Emission current	Dose time
PMMA	400 pA	2.1 μ s
PMMA/MMA double-layer resist	440 pA	2.2 μ s
ZEP	400 pA	0.6 μ s
ma-N2405	300 pA	0.45 μ s

Table 3.3: Conditions for the EB lithography of each kind of resist

Material	Deposition rate	Thickness
Cu	2.0 ~ 4.0 Å/s	100 nm
Bi	2.0 Å/s	20 nm
Pb	2.0 Å/s	20 nm
Py	0.4 ~ 1.5 Å/s	20 nm
Co	0.7 ~ 1.0 Å/s	100 nm
Nb	2.5 ~ 4.0 Å/s	30 nm

Table 3.4: Evaporation conditions for each metal.

Resist	Solvent
PMMA	Acetone
MMA	Acetone
ZEP	1-methyl-2-pyrrolidone
ma-N2405	Acetone

Table 3.5: Solvent for each resist

In other processes than the shadow evaporation, samples are taken out of the chamber between the deposition of different materials. All interfaces between two different materials are cleaned by an Ar-ion milling. Under the pressure of 2×10^{-4} Pa with Ar gas, the beam current and the acceleration voltage are 12 mA and 600 V, respectively.

To avoid surface oxidization, at the end of the process we deposit alumina (Al_2O_3) on top of the sample. Alumina is sputtered by the magnetron sputtering, and thickness is estimated to be 20 ~ 30 nm.

3.1.2 Shadow evaporation technique

The shadow evaporation technique is a useful method to deposit different materials *in situ* by evaporating different materials from different angles. For the shadow evaporation, we coat a substrate with two different types of resist which have different sensitivities to the electron beam: the polymethyl-methacrylate (PMMA) and methacrylate (MMA). After developing, due to the difference of the sensitivity we have an undercut structure (see Fig. 3.1). Owing to this undercut structure, we can deposit different kinds of material *in situ* from different angles to the substrate.

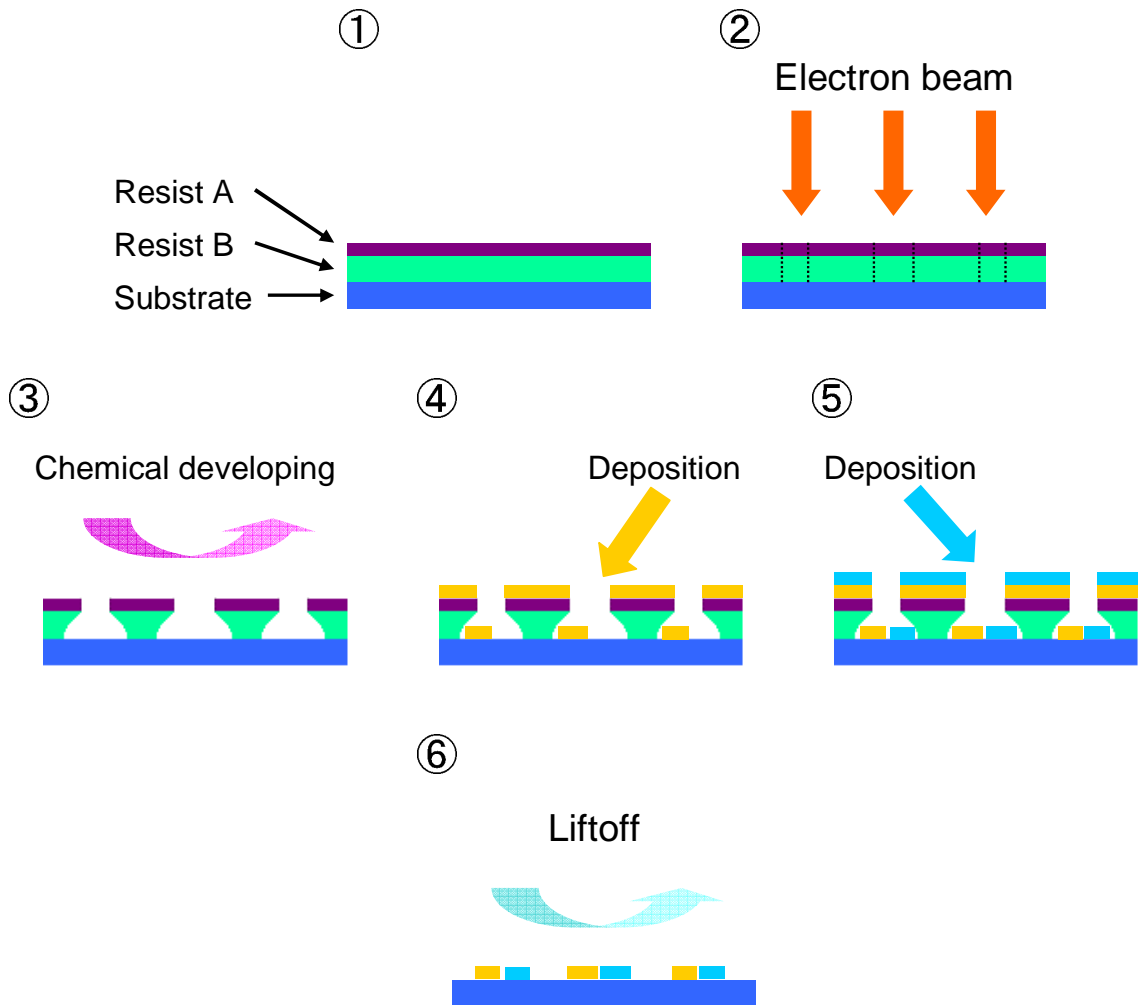


Figure 3.1: Process for the shadow evaporation. (1): Two different resists are coated on a substrate. (2): The resists are exposed to the electron beam. (3): Since sensitivity to the developer is different for the two resists, the lower resist is overdeveloped and transversal area has a trapezoid shape. (4,5): By depositing different materials from different angles, it is possible to deposit different kinds of material. (6): The resists are lift off.

3.1.3 Focused-ion-beam deposition and sputtering

The focused-ion-beam (FIB) system is a state-of-art technique for nanofabrication. By using the Ga-ion beam, one can perform sputtering of materials and depositon of carbon or tungsten (sometimes platinum).

Figure 3.2 shows the schematic illustration of the FIB sputtering in comparison to the scanning electron microscope (SEM). In the SEM, an electron beam irradiated to a material induces an emission of secondary electrons from the surface of the material. On the other hand, in the FIB system one can irradiate a beam of gallium (Ga) ions to a material. When the Ga-ion beam is irradiated, secondary electrons are emitted

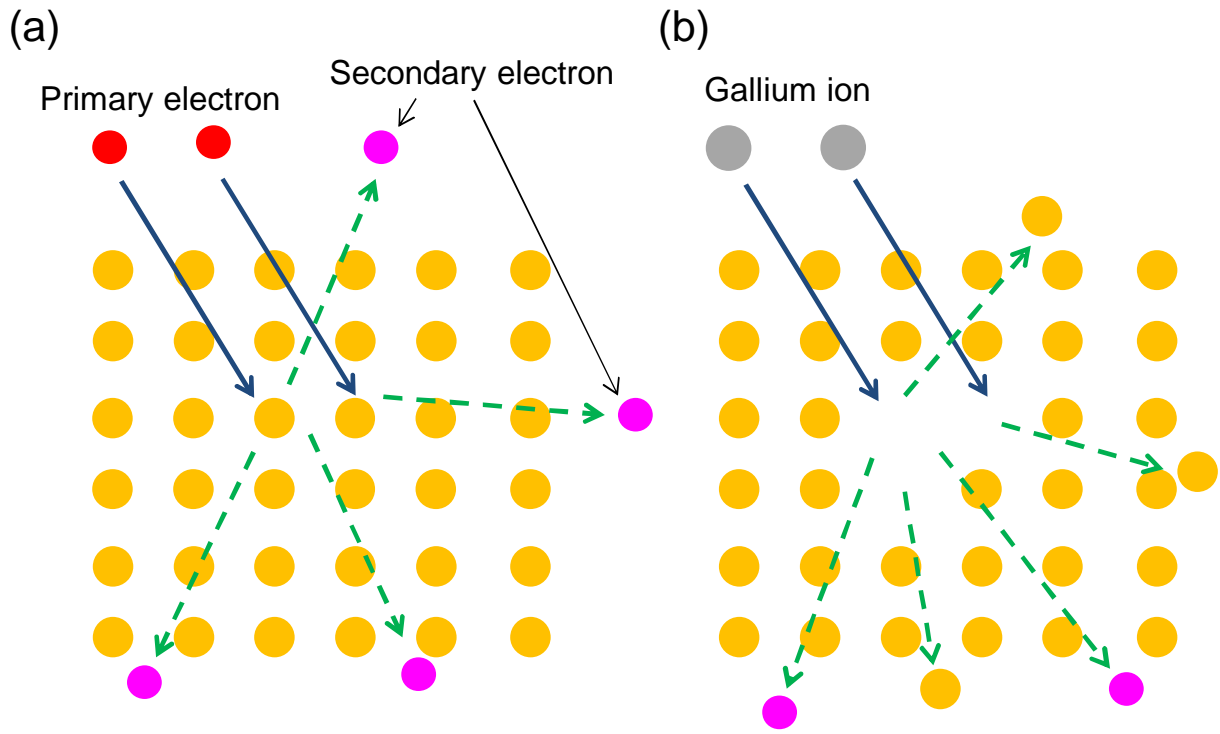


Figure 3.2: Schematic illustrations of the SEM (a) and the FIB system (b). In the SEM, an electron beam is irradiated to a material, and primary electrons of the electron beam eject secondary electrons. In the FIB system, a Ga-ions beam is irradiated, and this beam ejects not only secondary electrons but also atoms of the material because of the heavy mass of Ga.

and also, atoms on the surface of the material are ejected because of the much larger mass of Ga atoms than that of electrons. By controlling the acceleration voltage and the beam current, one can sputter materials using the FIB.

We next explain materials deposition in the FIB system. In the HITACHI NB5000 FIB system one can deposit carbon (C) or tungsten (W) in combination with the Ga-ion beam. In other FIB systems, platinum (Pt) deposition is also possible. Figure 3.3 shows the mechanism of materials deposition in the FIB systems. In the W deposition mode, the precursor gas $W(Co)_6$ is first injected in the process chamber. Subsequently, the Ga-ion beam is irradiated. This Ga-ion beam induces secondary electrons emitted from the surface of the material. These secondary electrons chemically resolve the precursor gas into solid and gas. While the gas is evacuated the solid is deposited on the surface of the material. Using this technique, one can deposit several materials onto the material.

As discussed in Chapter 6, the beam current (I_{Ga}) and the acceleration voltage (V_{acc}) of the Ga-ion beam are an important factor to perform both sputtering and deposition precisely. The beam current can be modulated by the acceleration voltage

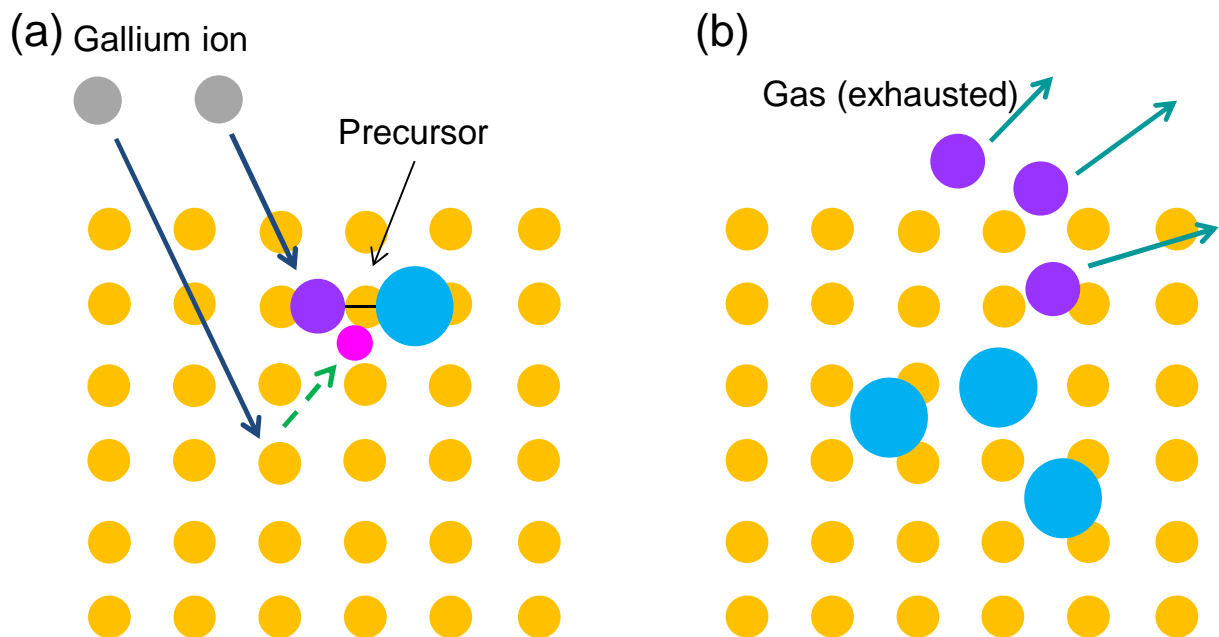


Figure 3.3: Image of the deposition mode. First the precursor gas is injected in the process chamber. Subsequently, the Ga-ions beam is irradiated to the substrate. Secondary electrons ejected from the substrate decompose the precursor into a gas and solid. The gas is exhausted but the solid is accelerated to the material and deposited onto the material.

and the size of the aperture for the beam. For the W deposition, we use at present $V_{\text{acc}} = 40$ kV and the aperture size of $30 \mu\text{m}$. The probe current is set to less than 5 pA.

3.2 Measurements

We perform electrical measurements both at room temperature (RT) and at low temperatures. We describe the details below.

3.2.1 Measurement circuits

A schematic illustration of the measurement circuits are shown in Fig. 3.4. We use a typical four-terminal ac rock-in technique with the frequency of 173 Hz for excitation currents. Current bias is obtained by the constant voltage source connected to a large resistor, $R_{\text{resistor}} \gg R_{\text{sample}}$. The voltage from the sample is amplified with a gain of 1000 and then filtered. External magnetic fields are applied by using an electromagnet, which can rotate around the cryostat.

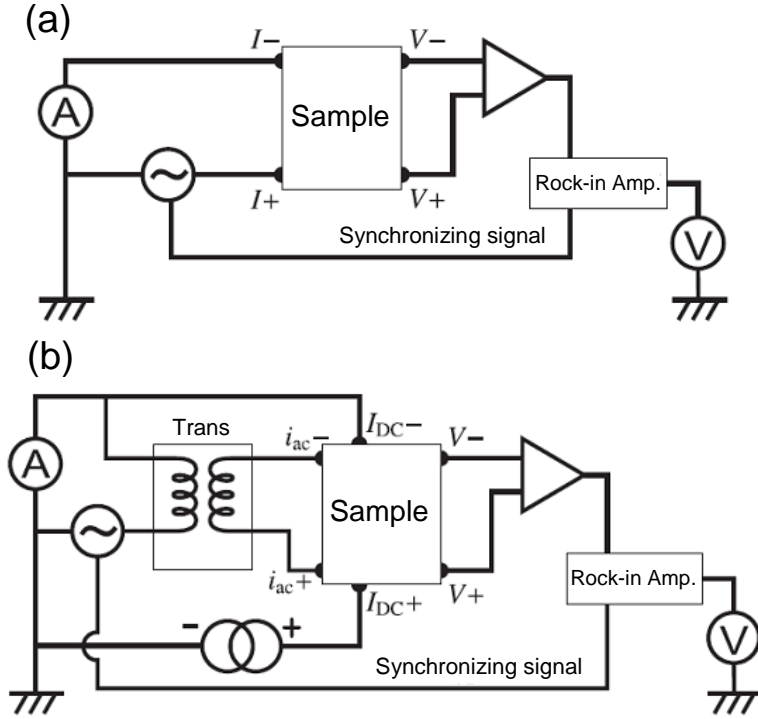


Figure 3.4: Schematic illustration of the circuit for electrical measurements. (a): Electrical circuit for all measurements except those for the spin injection current dependence of the resistance close to the superconductor/normal metal interface. (b): Electrical circuit for the spin injection current dependence of the resistance close to the superconductor/normal metal interface measurements.

3.2.2 Cooling system

Figure 3.5 shows our cooling system. Samples are installed in the insert, and the insert is cooled down in the cryostat. Samples can be cooled down to ~ 2 K, only by using ^4He flow in the cryostat. In this system, a sample is directly exposed to flowing ^4He gas pumped from the vessel which contained ^4He . The temperature is controlled under the PID operation with the heater equipped in the bottom of the cryostat. The temperature is also monitored by the thermometer at the bottom of the cryostat. For the spin absorption measurements into Nb, we use a one-shot ^3He insert. Samples are now installed at the edge of the insert, which is covered by the inner vacuum can (IVC). First the IVC is pumped up down to an order of 1×10^{-3} Pa through a fine vessel connected to the IVC. Next ^4He exchange gas is injected into the IVC, and the temperature of the IVC is controlled via the exchange of heat with outside of the IVC through the exchange gas. After the temperature of the IVC becomes lower than 3 K, the exchange gas is pumped up. We heat the sorbtion pump (sorb) to condense ^3He in the ^3He pot, close to the sample stage. In one or two hours, the condensation has been completed, then the sorb heater is turned off and the temperature of the sorb

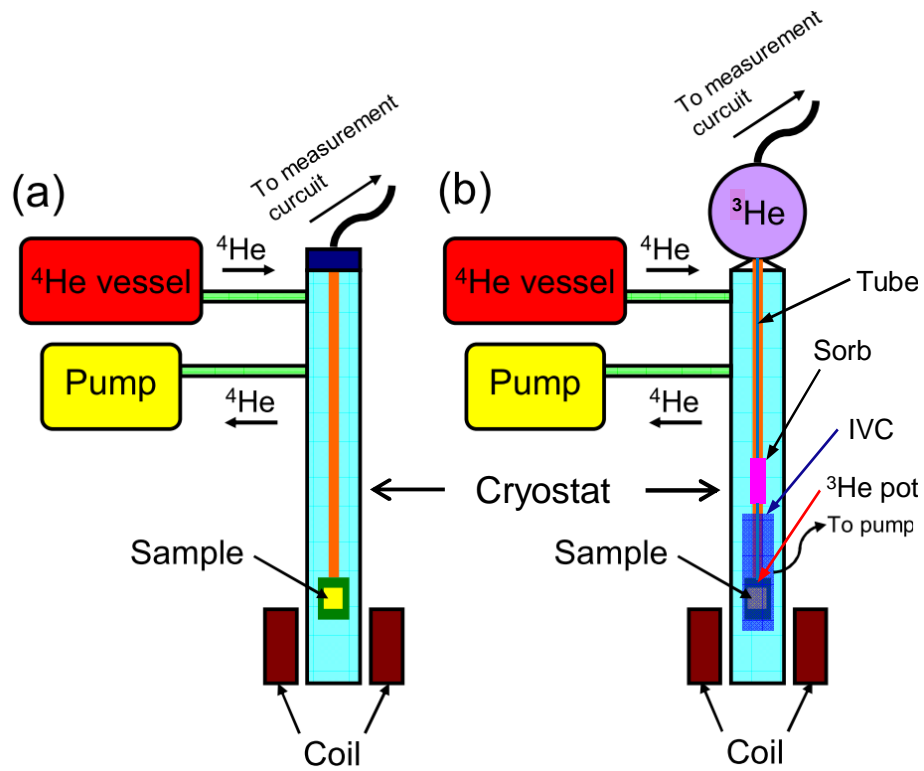


Figure 3.5: Schematic illustration of the cooling system. (a): ^4He flow cooling system. A sample is exposed to flowing ^4He gas and is cooled down to ~ 2 K. (b): One shot ^3He cryostat. A sample is now in the IVC and is cooled down to 350 mK.

falls. Then the pumping of ^3He begins and the temperature of the ^3He pot will fall to a minimum value ~ 370 mK.

Chapter 4

Spin injection into a superconductor with strong spin-orbit coupling

4.1 Introduction and Motivation

As discussed in the previous chapters, it is one of the important subjects in spintronics to inject spin currents into a wide variety of materials and investigate their spin transport properties. For applications, finding materials which have longer spin diffusion length is the central task because it enables us to transfer spin information in a long distance.

There have been a number of studies on spin transport so far, using normal metals or semiconductors in most cases. However, spin transport in superconductors has not

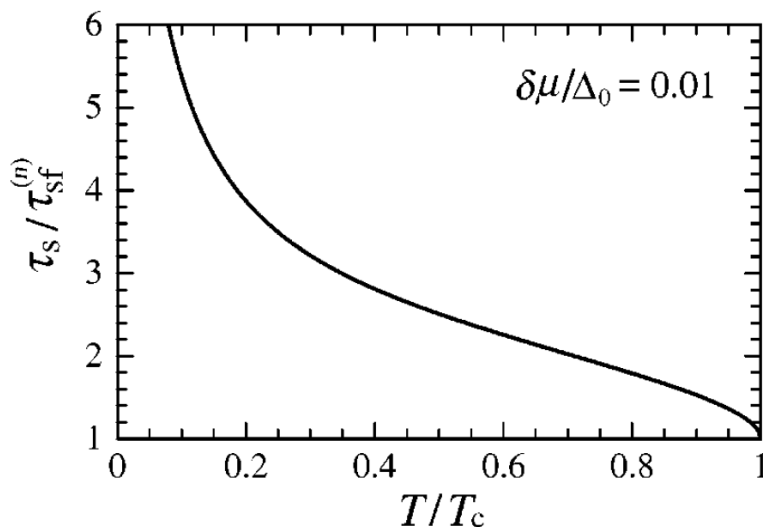


Figure 4.1: Theoretical calculation of the spin relaxation time in the superconducting state (τ_S) normalized by that in the normal state ($\tau_{sf}^{(n)}$). τ_S increases with decreasing temperatures below T_C (From [28]).

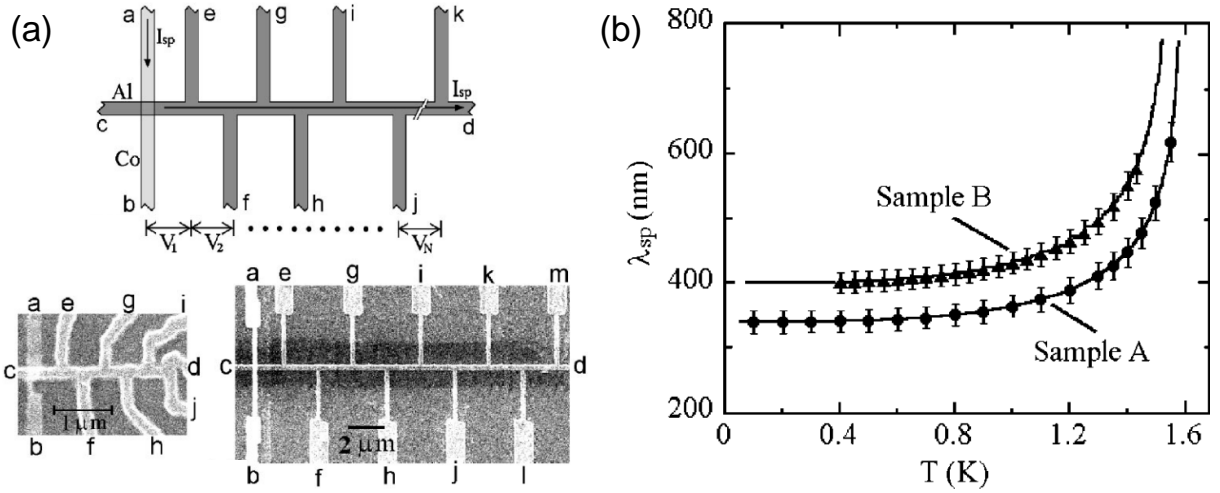


Figure 4.2: (a): Schematic and the SEM images of the device of Al/Co junction used in the study by Shin *et al.* [71]. The direct contact between the superconducting Al and ferromagnetic Co can induce the underestimation of spin relaxation. (b): Temperature dependence of the spin diffusion length in superconducting Al below T_C . Decreasing λ_{sp} with decreasing T_C might be due to mis use of D for quasiparticles and extra spin scattering at the interface with Co. We note that λ_{sp} in the normal state is $\sim 1 \mu\text{m}$.

been intensively explored yet. Indeed, superconductivity is a low temperature phenomenon and it does not appear at room temperature at the moment, spin transport in superconductors is intriguing both for scientific and engineering aspects. While few experimental studies have been carried out, potentiality of superconductors for spin transport has occasionally been pointed out theoretically. For example, as we have briefly remarked in the introductory chapter, due to the small group velocity of superconducting quasiparticles spin relaxation time (τ_{sf}) in superconductors is predicted to increase with decreasing temperature and become longer than that in their normal state [28] (see Fig. 4.1). Several experimental works have attempted to clarify this point. The biggest problem, however, is that these results are not consistent with each other. For example, while Yang *et al.* reported the million times enhancement of the spin relaxation time in superconducting Al [70], Shin *et al.* demonstrated that enhanced spin relaxation in Al in the superconducting state [71]. One of the reasons for such a deviation is that their device structures easily induce spurious effects so that τ_{sf} is underestimated or overestimated. As an example, we discuss results from the work done by Shin *et al.* [71]. As shown in Fig. 4.2, they have fabricated devices composed of a superconducting Al and ferromagnetic Co wire and made a Al/Co crossjunction. In this structure, the Co and Al wire contact directly to each other. However, this induces a problem to estimate τ_{sf} correctly because a direct contact of a superconductor to a ferromagnet strongly suppresses the superconducting gap, and also induces

an extra spin relaxation in the superconductor close to the interface with the ferromagnet. This is because the surface of a ferromagnet can be regarded as a sheet of magnetic impurities. In this study they have concluded that τ_{sf} in a superconducting Al is smaller than that above T_{C} . This is not consistent with the theoretical prediction by Yamashita *et al.* [28], but these spurious effects may induce an underestimation of τ_{sf} in a superconducting state as described above. The point which is often overlooked in the previous studies on the spin relaxation is the correction to the diffusion constant in the superconducting state. As we have remarked above, the group velocity of quasiparticles in superconductors is generically smaller than that of electrons. This causes the reduction of the diffusion constant as pointed out by Bardeen [72]. A diffusion constant D is written in three-dimensional systems as

$$D = \frac{1}{3}v^2\tau, \quad (4.1)$$

where v is the velocity of electrons and τ is the scattering time. For quasiparticles, both v and τ are corrected as [72, 28]

$$v_{\text{s}} = \frac{|\xi|}{E}v_{\text{n}}, \quad (4.2)$$

$$\tau_{\text{s}} = \frac{E}{|\xi|}\tau_{\text{n}}, \quad (4.3)$$

where ξ is $\varepsilon - \mu$, $E = \sqrt{\xi^2 + \Delta^2}$ with the superconducting gap Δ . In the above equations we explicitly write s (n) to express quantities in the superconducting (normal) state. Therefore the diffusion constant is also corrected as

$$D_{\text{s}} = \frac{|\xi|}{E}D_{\text{n}}. \quad (4.4)$$

This correction to D is often overlooked in the previous studies including [71], which can also induce the wrong estimation of the spin relaxation.

Taking into account these facts, even fundamental parameters for spin transport such as τ_{sf} have not been unambiguously evaluated for superconductors. To estimate these parameters precisely, experiments free from the spurious effects are highly demanded. In this study, we aim at demonstrating enhanced τ_{sf} in the superconducting state and exploring spin transport in superconductors. We note that our subject is NOT to obtain τ_{sf} longer than those presently reported for different materials. We used niobium as a superconductor. It is clear that to obtain longer τ_{sf} , as a superconductor aluminium is better because its spin-orbit interaction (SOI) is smaller than that of niobium. If we also include non-superconducting materials, organic materials like graphene should be more appropriate to acquire much longer τ_{sf} . One of the characteristics of niobium is that it has relatively large SOI among metallic superconductors.

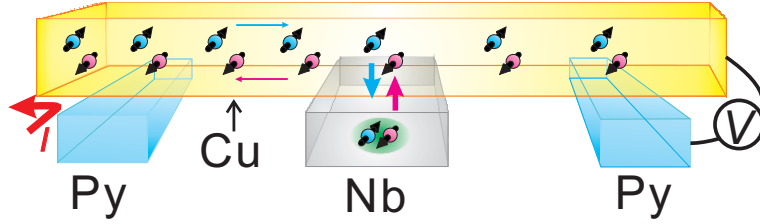


Figure 4.3: Schematic illustration of the spin absorption in the device with the Nb middle wire. A pure spin current is generated in the Cu bridge by passing a current between one of the Py wire and the Cu. The generated pure spin current is partly absorbed into the Nb middle wire because of the larger SOI of Nb than that of Cu. In this way spin injection into the Nb middle wire is possible.

As shown in the introductory chapters, SOI causes spin relaxation, but at the same time, it can generate intriguing phenomena, for example, the spin Hall effect (SHE). The SHE is indispensable to convert charge currents into spin currents and *vice versa*, and the SHE in superconductors is also predicted to exhibit different behaviors from those in normal metals. Our final goal is to observe the SHE in superconductors thus we have selected niobium as a superconductor. To inject spin currents into a superconducting niobium, spin-absorption technique is used. This technique is appropriate for materials with large SOI. In this regard, niobium is also favorable as a superconductor. Below we show outcomes of our research including experimental results, analyses and final conclusions.

4.2 Experimental results

To inject spin currents into superconductors we use the spin absorption technique. The spin absorption technique is useful especially for materials with large SOI, thus appropriate for superconducting Nb because it has relatively large SOI. A schematic illustration of the spin absorption measurement with the device structure is shown in Fig. 4.4. Since the details of the spin absorption technique have already been introduced in the previous chapters, we do not explain further. As a ferromagnet we use Py ($\text{Ni}_{81}\text{Fe}_{19}$) and as a nonmagnet Cu. To fabricate devices, we exploit the shadow evaporation technique. Through the shadow evaporation technique one can obtain a highly transparent interface between Nb and Cu. The fabrication process is as follows: we first do the electron beam (EB) lithography to the PMMA/MMA double layer resist on thermally oxidized SiO_2/Si substrates. After patterning and developing the resists, materials are deposited: Py is first evaporated onto the substrate at an angle of 30° from the horizontal axis, parallel to the surface of the substrates. Next Nb is deposited at an angle of 45° from the center direction. Finally, a nonmagnet Cu is

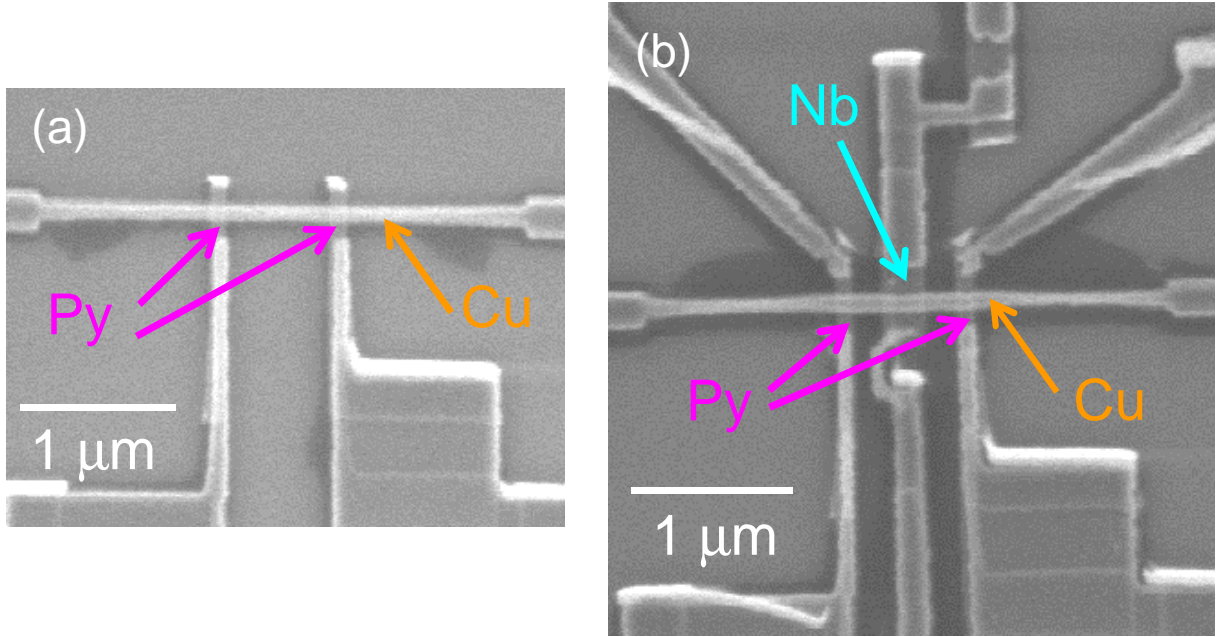


Figure 4.4: The SEM images of the device structures. (a): the typical lateral spin valve device. Two ferromagnetic Py wires are bridged by a nonmagnetic Cu wire. (b): the device for the spin absorption measurements. In between the two Py wires the Nb middle wire is inserted below the Cu bridge.

evaporated normal to the substrate. Py and Nb are evaporated by the EB, and Cu is deposited by thermal evaporation. Owing to this shadow evaporation technique, all fabrication processes can be done *in situ*. The base pressure of the chamber during the evaporation process is $\leq 10^{-9}$ Torr.

We fabricate two types of devices. One is the typical lateral spin valve device, where two Py wires are bridged by a nonmagnetic Cu wire (Fig. 4.3(a)). The other is the device for the spin absorption measurements, where an extra wire (middle wire) is inserted below the Cu wire in between the two Py wires (Fig. 4.3(b)). The center-to-center distance between the two Py wires is 900 nm, and width of the Py, Cu and Nb wires are 100 nm, 100 nm and 300 nm, respectively. Thickness of the Py, Cu and Nb wire is 20 nm, 100 nm, and 20 nm, respectively. Measurements are done with typical lockin technique at 10 K and 370 mK. Frequency of the excitation currents is 173 Hz. Samples are installed in a cryostat, and cooled down by a flow of ^4He in the cryostat down to 10 K. To carry out measurements at 370 mK, we equip samples with the one-shot type ^3He cooling system. To generate external magnetic field necessary for nonlocal spin valve (NLSV) measurements, rotational electromagnet is used.

We first measure the transition temperature (T_C) of the Nb middle wire. The temperature dependence of the resistance shows $T_C = 5.5$ K. Considering this T_C ,

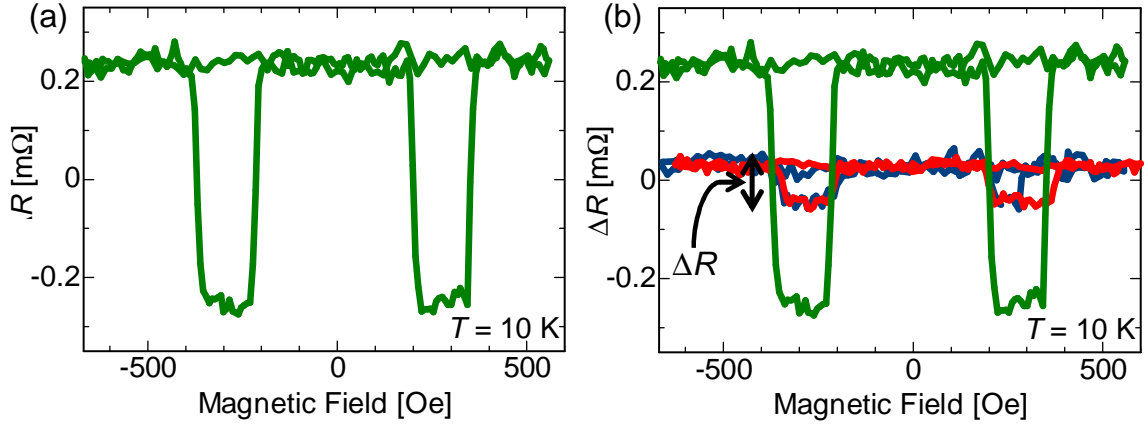


Figure 4.5: NLSV signals at 10 K, above T_C , obtained from sample with or without the Nb middle wire. (a): a signal from a sample without the Nb middle wire. The signal is typical NLSV signal. (b): signals from a sample with the Nb middle wire (red and blue curves) with the reference signal (green curve) shown in (a). Two curves both show suppressed signals compared with the green one. This explicitly demonstrates the spin absorption effect. Difference between the red and blue curve is difference in the spin injection current I . Blue: $I = 20 \mu\text{A}$ and red: $I = 100 \mu\text{A}$.

we next carry out the NLSV measurements at 10 K, above T_C . Figure 4.5(a) shows the NLSV signal obtained from the samples without the Nb middle wire. A current passing between the Py injector and the Cu bridge (spin injection current, I) is $100 \mu\text{A}$ in this measurement. As displayed in Fig. 4.5(a), it shows a typical NLSV signal. The amplitude at 10 K is $\approx 0.5 \text{ m}\Omega$, consistent with our previous studies [25]. We then perform the same measurements for samples with the Nb middle wire. Obtained signals are shown in Fig. 4.5(b) with the same signal shown in Fig. 4.5(a) for comparison. The NLSV signals from the sample with the Nb middle are explicitly suppressed, indicating that spin currents in the Cu bridge are partly absorbed into the Nb middle wire so that the spin currents detected in the Py detector is reduced, consistent with our previous studies [25, 26, 27]. The red and blue curves are both from a sample with the Nb middle wire, but different in the spin injection current I . Comparing signals with $I = 20 \mu\text{A}$ and $I = 100 \mu\text{A}$, their amplitudes are found to be almost the same. This demonstrates that the spin absorption does not depend on the spin injection current I in the normal state.

We next cool the sample down to 370 mK and measure the NLSV signals. Remarkably, as shown in Fig. 4.6 the signal from the sample with the Nb middle wire with $I = 20 \mu\text{A}$ becomes much larger than that with $I = 100 \mu\text{A}$. This behavior is observed only at temperatures below T_C thus specific to the superconducting state.

To elucidate the details of this anomalous behavior, we measure the I dependence of the NLSV signals ΔR . The results are shown in Fig. 4.7. At 10 K, above T_C ,

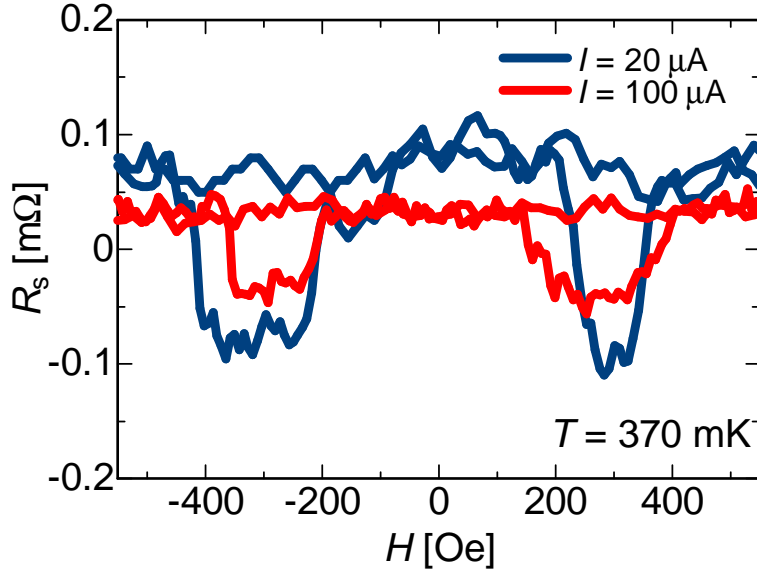


Figure 4.6: NLSV signals taken at 370 mK from a sample with the Nb middle wire. Blue curve is with $I = 20 \mu\text{A}$ and red one is with $I = 100 \mu\text{A}$. ΔR in the blue curve is explicitly larger than that in the red one.

ΔR is almost independent of I . However, at 370 mK as I decreases ΔR dramatically increases and at $I = 10 \mu\text{A}$, ΔR becomes more than twice larger than those for $I > 100 \mu\text{A}$. Increasing ΔR with decreasing I indicates that for smaller I the spin absorption is suppressed.

In order to investigate how superconductivity plays a role to the anomalous I dependence of the NLSV signals, we measure the resistance close to the Nb/Cu interface because the interface is the most sensitive part for the spin absorption effect. We first show the temperature dependence of the resistance in Fig. 4.8(a) with the measurement setup in the inset. The resistance R_{I} is defined as $R_{\text{I}} \equiv (V_+ - V_-)/i$. At $T \sim T_{\text{C}}$, R_{I} shows a sharp peak, and above T_{C} $R_{\text{I}} < 0$ and below T_{C} , on the other hand, $R_{\text{I}} > 0$. $R_{\text{I}} < 0$ above T_{C} is an artifact and originated from the current inhomogeneity at the transparent interface between the Nb and Cu. We note that similar "negative resistance" effect has been reported for giant magnetoresistance measurements with the metallic interface [73, 74]. The peak structure at $T = T_{\text{C}}$ and an extra resistance added for $T < T_{\text{C}}$ is explained by the charge imbalance effect as previously observed at the transparent superconductor/normal metal interface [75, 76, 77]. We next fix the sample temperature to 370 mK, and measured the I dependence of R_{I} . The measurement setup is also shown in the inset of Fig. 4.8(b). Surprisingly, the I dependence of R_{I} shows the same curve as Fig. 4.8(a). This correspondance between the T and I dependence of R_{I} indicates that with increasing I , the effective temperature at the Nb/Cu interface deviates from the temperature of the bath. In the next subsection, we

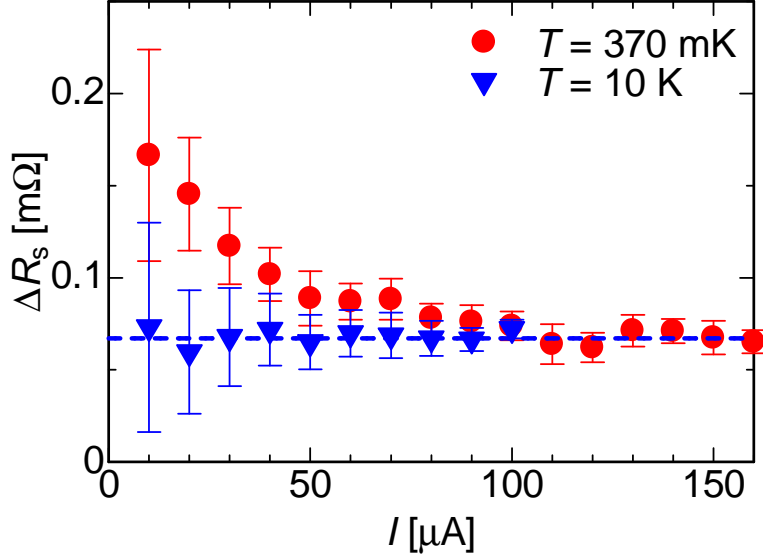


Figure 4.7: Spin injection current I dependence of the NLSV signals ΔR . At 10 K (blue triangles), ΔR is almost independent of I . However, at 370 mK (red circles), as I decreases ΔR dramatically increases, and at $I = 10 \mu\text{A}$, the magnitude of ΔR becomes more than those at $I > 100 \mu\text{A}$.

will explain how we analyze the experimental data including this effective temperature increase at the Nb/Cu interface.

4.3 Analysis

By comparing Fig. 4.8(a) and (b), we can estimate the effective temperature T_{eff} at the Nb/Cu interface for each I . The relation between T_{eff} and I is plotted in Fig. 4.9, where experimental results are shown with blue dots. To analyze these data, we then make a model of the system: Increase of the temperature at the Nb/Cu interface can be assumed to be caused by the spin injection current I . When I is passing between the Py spin injector and the Cu bridge, the Joule heating effect can occur. When a current I is flowing through the resistance R for time t , the Joule heating Q is expressed as

$$Q = RI^2t. \quad (4.5)$$

We note that the resistivity of 20 nm-thick Py is almost ten times larger than that of 100 nm-thick Cu ($\rho_{\text{Py}} = 20 \mu\Omega \text{ cm}$, $\rho_{\text{Cu}} = 2 \mu\Omega \text{ cm}$, at 10 K). Moreover, the thickness of the Py spin injector is five times smaller than that of Cu. Therefore, the Py spin injector has even larger R than that of the Cu bridge, and most of the contribution to the Joule heating should come from the Py spin injector. Hence for R in (4.5), we substitute that of the Py spin injector R_{Py} . Since electrons move diffusively in the Py

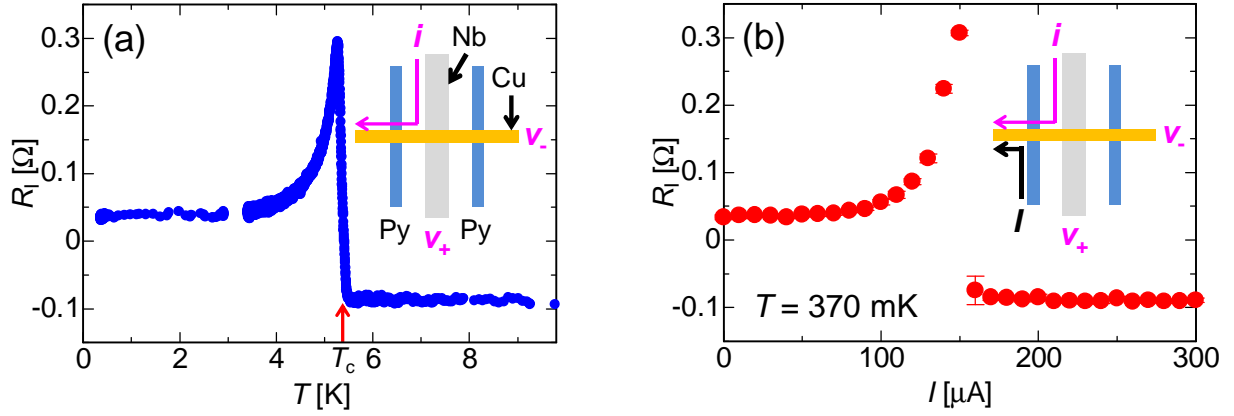


Figure 4.8: Temperature (T) and the spin injection current I dependence of the resistance close to the Nb/Cu interface (R_I). (a): T dependence of R_I . At T_C , the sharp peak is observed. Below T_C , an extra resistance is added. Both of these effects are attributed to the charge imbalance effect. (b): I dependence of R_I . The curve is exactly the same as the one in (a). Insets: the experimental setup for each measurement.

spin injector, we thus consider the diffusive equation to evaluate t in (4.5) then t can be written as

$$t = \frac{L^2}{D}, \quad (4.6)$$

where L is the length of the Py spin injector where I flows, and D is the diffusion constant of the Py. In our case $L = 90$ nm, and the diffusion constant D can be derived from the Einstein's relation $\sigma = e^2 N(0) D$, where σ is the conductivity, e the electrostatic constant and $N(0)$ is the density of states at the Fermi energy. Using the experimental value $\sigma = 5 \times 10^6 \Omega^{-1} \text{m}^{-1}$ and $N(0) = 1.0 \times 10^{48} \text{J}^{-1} \text{m}^{-3}$ for Py [78], we can obtain t .

Heat generated in the Py wire is transferred through the Cu bridge. By integrating the heat capacity of Cu, we can express temperature dependence of energy per volume in Cu as

$$\varepsilon = \gamma T^2 + AT^4, \quad (4.7)$$

where γ is the electronic heat capacity constant of Cu, A is the heat capacity for phonons. At low temperatures, we can neglect the second term. By using this approximation and equating (4.5) and (4.7), we find that

$$R_{\text{Py}} I^2 \frac{L^2}{D} = \gamma V T^2, \quad (4.8)$$

where V is the volume of the part of the Cu bridge which contributes to transfer heat flow. We can then obtain a linear relation between I and T_{eff} as

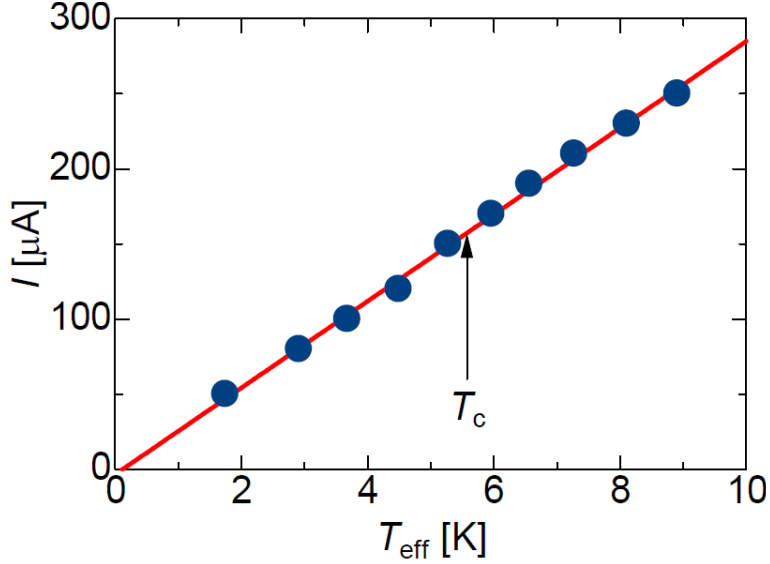


Figure 4.9: Relation between I and T_{eff} . Blue dots are from experimental results. Red curve is from the analysis. The red curve reproduces well the experimental data.

$$I = \sqrt{\frac{G}{Rt}} T_{\text{eff}}, \quad (4.9)$$

where $G \equiv \gamma V$. With $\gamma = 1.6 \times 10^{-4} \text{ cal-mole}^{-1}\text{-K}^{-2}$ [79] and $G = 3.2 \times 10^{-19} \text{ JK}^{-2}$, we obtain

$$\sqrt{\frac{G}{Rt}} = 2.9 \times 10^{-5} \text{ AK}^{-1}. \quad (4.10)$$

The relation (4.10) is plotted in Fig. 4.9. It is easily found that the calculational data reproduces the experimental data well, implying the validity of our analysis.

Accounting for an effective increase of temperature at the Nb/Cu interface, we next calculate the spin transport between the Nb middle wire and the Cu bridge to explain the anomalous behavior of the spin absorption. We can calculate the amount of absorbed spin currents into the middle wire from the reduced NLSV signal. Details of equations follow [26]. The ratio of the NLSV signal between the sample with/without the middle wire is written as

$$\frac{\Delta R_s^{\text{with}}}{\Delta R_s^{\text{without}}} = \frac{2Q_{\text{Nb}} \left\{ \sinh(L/\lambda_{\text{sf}}^{\text{Cu}}) + 2Q_{\text{Py}} e^{L/\lambda_{\text{sf}}^{\text{Cu}}} + 2Q_{\text{Py}}^2 e^{L/\lambda_{\text{sf}}^{\text{Cu}}} \right\}}{\left\{ \cosh(L/\lambda_{\text{sf}}^{\text{Cu}}) - 1 \right\} + 2Q_{\text{Nb}} \sinh(L/\lambda_{\text{sf}}^{\text{Cu}}) + 2Q_{\text{Py}} \left\{ e^{L/\lambda_{\text{sf}}^{\text{Cu}}} (1 + Q_{\text{Py}})(1 + 2Q_{\text{Nb}}) - 1 \right\}}, \quad (4.11)$$

where Q_{Nb} and Q_{Py} are the ratio between the spin resistance of the Nb (Py) and the Cu, namely $Q_{\text{Nb(Py)}} = \mathcal{R}_{\text{Nb(Py)}}/\mathcal{R}_{\text{Cu}}$, and $\lambda_{\text{sf}}^{\text{Cu}}$ is the spin diffusion length of Cu. The

Material	Spin diffusion length λ_{sf} [nm]	Resistivity ρ [$\mu\Omega\text{cm}$]
Py	5	20
Cu	1300	2
Nb	6	110

Table 4.1: Values of parameters used in (4.11). All of these values are at 10 K.

spin resistance for the material X is written as $\mathcal{R}_X = \rho_X \frac{\lambda_{\text{sf}}^X}{A_X}$ with the electrical resistivity ρ_X , the spin relaxation length λ_{sf}^X and the cross sectional area of the wire A_X (we note that for Nb and Py, we take the junction area with Cu due to their small λ_{sf}^X). L is the distance between the two Py wires. We show some values of parameters which appear in (4.11) in Table 4.1. From (4.11) with using these values, we can obtain a value of Q_{Nb} thus $\lambda_{\text{sf}}^{\text{Nb}}$. The spin current injected into the middle wire I_s is, on the other hand, expressed as

$$I_s = \frac{2PQ_{\text{Py}} (\sinh(L/2\lambda_{\text{sf}}^{\text{Cu}}) + Q_{\text{Py}} \exp(L/2\lambda_{\text{sf}}^{\text{Cu}}))}{\{\cosh(L/\lambda_{\text{sf}}^{\text{Cu}}) - 1\} + 2Q_{\text{Nb}} \sinh(L/\lambda_{\text{sf}}^{\text{Cu}}) + 2Q_{\text{Py}} \left\{ e^{L/\lambda_{\text{sf}}^{\text{Cu}}} (1 + Q_{\text{Py}})(1 + 2Q_{\text{Nb}}) - 1 \right\}} I, \quad (4.12)$$

where P is the spin polarization of Py, I the spin injection current. We use $P = 0.30$ [26] for Py. Thus we can associate (4.11) with (4.12) as

$$\frac{\Delta R_s^{\text{with}}}{\Delta R_s^{\text{without}}} = \frac{2Q_{\text{Nb}} \left\{ \sinh(L/\lambda_{\text{sf}}^{\text{Cu}}) + 2Q_{\text{Py}} e^{L/\lambda_{\text{sf}}^{\text{Cu}}} + 2Q_{\text{Py}}^2 e^{L/\lambda_{\text{sf}}^{\text{Cu}}} \right\} I_s}{2PQ_{\text{Py}} (\sinh(L/2\lambda_{\text{sf}}^{\text{Cu}}) + Q_{\text{Py}} \exp(L/2\lambda_{\text{sf}}^{\text{Cu}}))} \frac{1}{I}. \quad (4.13)$$

The equation above, the only unknown parameter is Q_{Nb} when Nb is in the superconducting state. Thus for a certain I , Eq. (4.13) can be written as

$$\Delta R_s^{\text{with}} = \text{const.} \times Q_{\text{Nb}} \frac{I_s}{I} \quad (4.14)$$

The constant is the same both for the superconducting and the normal state of Nb. Thus the ratio $\Delta R_s^{\text{super}}/\Delta R_s^{\text{normal}}$ with the Nb middle wire for a certain I becomes

$$\frac{\Delta R_s^{\text{super}}}{\Delta R_s^{\text{normal}}} = \frac{Q_{\text{Nb}}^{\text{super}} I_s^{\text{super}}}{Q_{\text{Nb}}^{\text{normal}} I_s^{\text{normal}}}. \quad (4.15)$$

The injected spin current, on the other hand, is expressed with the density of states as

$$I_s = \mathcal{A} \int_{-\infty}^{\infty} |\mathcal{T}|^2 N_{\text{N}}(E) N_{\text{S}}(E) (f^{\uparrow}(E) - f^{\downarrow}(E)) dE, \quad (4.16)$$

where \mathcal{A} is the geometry factor related to the junction, \mathcal{T} the transmission coefficient, $N_{N(S)}(E)$ the density of states (DOS) of Cu (Nb), $f^{\uparrow(\downarrow)}$ the nonequilibrium distribution function in Nb for upspin (downspin). By approximating the nonequilibrium distribution function $f^{\uparrow(\downarrow)}(E) \sim f_0(E - \sigma\delta\mu) \sim f_0(E) - \sigma\delta\mu \frac{\partial f_0}{\partial E}$ [35, 80], where $f_0(E) = 1/(\exp(E/k_B T) + 1)$ and σ is $+(-)$ for upspin (downspin) electrons $\delta\mu$ the spin accumulation. We can transform (4.16) into

$$I_s = 2\delta\mu\mathcal{A}N_N(0) \int_{-\infty}^{\infty} |\mathcal{T}|^2 N_S(E) \left(-\frac{\partial f_0(E)}{\partial E} \right) dE. \quad (4.17)$$

This equation shows that the DOS in the superconducting state strongly affects the transmission probability of electrons between the Nb and Cu wire, and we assume $N_N(E) \sim N_N(0)$ for the Cu wire. Thus the ratio of the injected spin current between superconducting/normal Nb can be written as

$$\frac{I_s^{\text{super}}}{I_s^{\text{normal}}} = \int_{-\infty}^{\infty} n_S(E) \left(-\frac{\partial f_0(E)}{\partial E} \right) dE, \quad (4.18)$$

where $n_S(E) = N_S(E)/N(0)$. We can relate the amount of the NLSV signals and the DOS of Nb using (4.15) and (4.18):

$$\frac{\Delta R_s^{\text{super}}}{\Delta R_s^{\text{normal}}} = \frac{Q_{\text{Nb}}^{\text{super}} I_s^{\text{super}}}{Q_{\text{Nb}}^{\text{normal}} I_s^{\text{normal}}} = \frac{Q_{\text{Nb}}^{\text{super}}}{Q_{\text{Nb}}^{\text{normal}}} \int_{-\infty}^{\infty} n_S(E) \left(-\frac{\partial f_0(E)}{\partial E} \right) dE. \quad (4.19)$$

To reproduce $\Delta R_s^{\text{super}}/\Delta R_s^{\text{normal}}$ therefore $n_S(E)$ and $Q_{\text{Nb}}^{\text{super(normal)}}$ have to be determined. $Q_{\text{Nb}}^{\text{super(normal)}}$ can be calculated by the ratio of $\Delta R_s^{\text{with}}/\Delta R_s^{\text{without}}$. In the following, we describe how to calculate $n_S(E)$ in our system.

We next calculate the DOS of the superconducting Nb, $n_S(E)$. Because of the transparent interface between the Nb and Cu, we have to consider superconducting proximity effect [81, 82]. The proximity effect causes smearing of the DOS in the Nb, and induces a finite pair potential in the Cu. The DOS including the proximity effect can be calculated by using the Usadel equation [83, 84, 85], which consists of two equations [86]:

$$\frac{\hbar D}{2} \frac{\partial^2 \theta}{\partial x^2} + \left(iE - \frac{\hbar}{2\tau_{\text{sf}}} \cos \theta \right) \sin \theta + \Delta(x) \cos \theta = 0, \quad (4.20)$$

where D is the diffusion constant, τ_{sf} the spin relaxation time and $\Delta(x)$ the pair potential, and

$$\Delta(x) = N_S(0)V \int_0^{\hbar\omega_D} \tanh \left(\frac{E}{2k_B T} \right) \text{Im}[\sin \theta] dE, \quad (4.21)$$

where $N_S(0)$, V and ω_D are the DOS of Nb in normal state, the pairing interaction strength, and the Debye frequency respectively. θ is the order parameter, and the

normalized DOS $n_S(E)$ in the superconducting state is written as $n_S(E) = \text{Re}[\cos \theta]$. We take $x = 0$ at the Nb/Cu interface and $x < 0$ in the Nb side. The point of the Usadel equation (4.20) is that it contains a term with τ_{sf} , the spin relaxation time of Nb. $I_s^{\text{super}}/I_s^{\text{normal}}$ can be numerically evaluated by calculating $n_S(E)$ through the Usadel equation. $I_s^{\text{super}}/I_s^{\text{normal}}$ can be also experimentally obtained by using $\Delta R_s^{\text{super}}/\Delta R_s^{\text{normal}}$ and the equation (4.15). Therefore we calculate $n_S(E)$ so that the calculated $I_s^{\text{super}}/I_s^{\text{normal}}$ corresponds to that of the experimental values.

Below we show how to calculate the Usadel equation and reproduce the experimental data. First we start with a simple one-dimensional Usadel equation expressed as

$$\pi \frac{\partial^2}{\partial x^2} \theta + iE \sin \theta = 0, \quad (4.22)$$

where θ is an order parameter and complex. We divide θ into a real part θ_r and an imaginary part θ_i , thus we can write

$$\theta = \theta_r + i\theta_i. \quad (4.23)$$

Substituting (4.23) into (4.22), we obtain two equations for θ_r and θ_i ,

$$\pi \frac{\partial^2}{\partial x^2} \theta_r - E \cos \theta_r \sinh \theta_i = 0 \quad (4.24)$$

$$\pi \frac{\partial^2}{\partial x^2} \theta_i + E \sin \theta_r \cosh \theta_i = 0. \quad (4.25)$$

Boundary conditions at the S/N interface can be expressed as follows [87]:

$$\begin{aligned} \theta_r(+0) = \\ \theta_r(-0) + \arcsin \sqrt{\frac{1}{2} \left(\sqrt{b^2 a^2 - \frac{\sqrt{a^4 b^4 - 2a^4 b^2 + a^4 + 2a^2 b^4 + 2a^2 b^2 + b^4}}{a^2}} + b^2 + 1 \right)} \end{aligned} \quad (4.26)$$

$$\theta_i(+0) = \theta_i(-0) - \text{arcsinh} \left[\frac{\gamma_B}{\gamma} \frac{\theta_i'(-0)}{\cos[\theta_r(-0) - \theta_r(+0)]} \right], \quad (4.27)$$

where

$$a = \frac{\theta_r'(-0)}{\theta_i'(-0)}, b = \frac{\gamma_B}{\gamma} \theta_i'(-0), \quad (4.28)$$

θ_r' and θ_i' are both first derivatives of θ_r and θ_i , respectively. γ_B and γ are parameters which characterize the amplitude of the superconducting proximity effect. Condition for θ in the S side is taken $\theta = \theta_{\text{BCS}}$ [86] where θ_{BCS} is defined as

$$\tan \theta_{\text{BCS}} = i \frac{\Delta}{E} \quad (4.29)$$

where Δ is the superconducting gap. This condition can be divided into two parts,

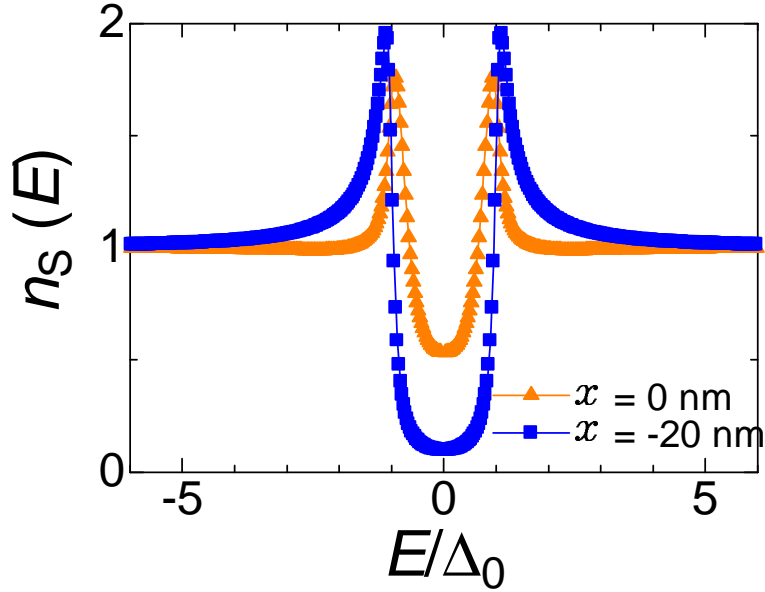


Figure 4.10: The calculated DOS in the Nb middle wire side. $x = 0$ at the Nb/Cu interface and $x < 0$ is the Nb side. Orange dots are the DOS at the interface and blue dots are at the surface of the Nb wire.

namely, for θ_r and θ_i by expressing E with a real and an imaginary part separately as

$$E = E' + iE'' . \quad (4.30)$$

Substituting (4.30) into (4.29) we can write down the condition as

$$\theta_r = \frac{\pi}{2} + \frac{1}{2} \arctan \left(\frac{-2E''^2}{1 - E'^2 - E''^2} \right) \quad (4.31)$$

$$\theta_i = -\frac{1}{4} \ln \left(\frac{(1 - E'^2 - E''^2)^2 + 4E''^2}{[(1 + E')^2 + E''^2]^2} \right) , \quad (4.32)$$

with $E'' = \hbar/\tau_{sf}$. Substituting (4.30) into (4.22), we obtain

$$\pi \frac{\partial^2}{\partial x^2} \theta_r - E' \cos \theta_r \sinh \theta_i - E'' \sin \theta_r \cosh \theta_i = 0 \quad (4.33)$$

$$\pi \frac{\partial^2}{\partial x^2} \theta_i + E' \sin \theta_r \cosh \theta_i - E'' \cos \theta_r \sinh \theta_i = 0 . \quad (4.34)$$

We note that on the N side far from the interface with the superconductor $\theta = 0$. The superconducting gap Δ is calculated using the equation

$$\Delta(x) = N_S(0)V \int_0^{\hbar\omega_D} \tanh \left(\frac{E}{2k_B T} \right) \text{Im}[\sin \theta] dE . \quad (4.35)$$

The scheme for our calculations is as follows:

- (1): We first assume a certain value for $\partial_x \theta_r$ and $\partial_x \theta_i$ at the surface of the supercon-

ducting Nb, and by using the Runge-Kutta method we solve (4.33) and (4.34). Initial conditions for θ_r and θ_i is determined from (4.29). For Δ , we include the approximated temperature dependence, written as [88]

$$\Delta(T) = \Delta_0 \left(1 - \frac{T}{T_C}\right)^{1/2}, \quad (4.36)$$

where Δ_0 is the superconducting gap at $T = 0$.

(2): At the interface between the superconducting Nb and the Cu, we use the boundary conditions (4.26) and (4.27) and keep the calculation also for the Cu side.

(3): In the region $x \gg \xi_N$, where ξ_N is the coherence length of the Cu, the order parameter $\theta = 0$. The boundary condition for the Cu wire is that at the surface of the Cu $\theta = 0$.

(4): To fulfill the condition in (3), we appropriately choose the initial condition for the first derivative of θ_r and θ_i .

(5): We calculate $\Delta(x)$ in each n th step using the value of θ for $n - 1$ step, and the resulting $\Delta(x)$ is reflected to E and the calculations in the n th step.

We show in Fig. 4.10 the DOS calculated based on this scheme. We show the DOS at $x = 0$ nm (at the S/N interface) and that at $x = -20$ nm (at the surface of the superconducting Nb wire). Using the calculated DOS and the equations (4.17) and (4.18), we can obtain τ_{sf} for each I in the superconducting Nb. In Fig. 4.11 we show τ_{sf} normalized by that at the normal state ($\tau_{sf}^{\text{normal}}$) as a function of I . It is easily found that with decreasing I , τ_{sf} increases and for $I = 10 \mu\text{A}$, τ_{sf} is more than four times larger than that in the normal state. Considering the correspondance between I and T at the Cu/Nb interface, this result is an experimental demonstration of increasing τ_{sf} with decreasing T in the superconducting state as predicted by [28].

4.4 Interface effects: shadow evaporation vs sputtering

In the above experiments we exploit the shadow evaporation technique to fabricate the lateral spin valves with the Nb middle wire. The shadow evaporation technique is very useful to make devices with all processes *in situ*, therefore highly transparent contact is achievable between a superconductor (S) and a normal metal (N). However, there are some limitations in the shadow evaporation technique to design complex

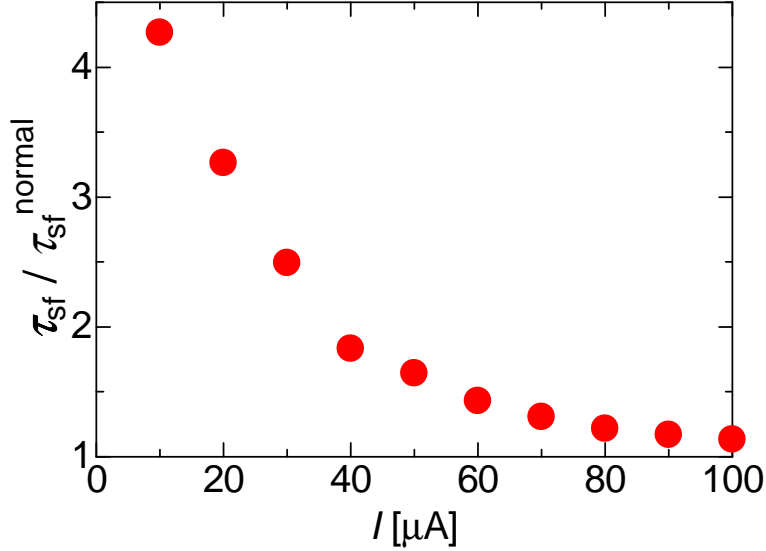


Figure 4.11: Spin injection current I dependence of the spin relaxation time in superconducting Nb (τ_{sf}) normalized by that in the normal state ($\tau_{sf}^{\text{normal}}$). As I decreases, τ_{sf} increases and becomes more than four times larger than that in the normal state with $I = 10 \mu\text{A}$. [90]

structures. For example, for devices used in the spin absorption experiments shown above it is impossible to make long Nb middle wires without any other materials above or below the Nb wires because in the fabrication process, Cu or Py is inevitably deposited above or below the Nb wire. We note here that Cu nor Py is contacted to the part of the Nb middle wire which contributes to the spin absorption and spin relaxation. Direct contact between ferromagnets and superconductors induces the strong inverse proximity effect [82] and reduces T_C . It also causes an additional spin relaxation [89]. For a similar reason, putting electrodes directly to the Nb middle wires is also impossible with the shadow evaporation technique. To detect the spin Hall effect (SHE) or the inverse spin Hall effect (ISHE) in superconductors, however, we have to place voltage probes which contact to a superconductor directly [35, 80]. To do this, we have to give up fabricating samples *in situ* and take out samples from the chamber between the evaporation of different materials. In the following we discuss difference between these two processes and how it affects the spin absorption into superconductors. Since we do not use the shadow evaporation, we can also use the sputtering technique to deposit Nb layers. The problem of the EB evaporation of Nb is that properties of Nb strongly depends on the deposition rate, and it is technically difficult to keep the high deposition rate. On the other hand, sputtering is more stable to deposit Nb. Thus in the new process we attempt to deposit Nb both by the sputtering and the EB evaporation. We first coat the PMMA resist onto Si/SiO₂

substrates then do the EB lithography. After depositing Py, we take out the substrate from the chamber and then again put the resist (ZEP520A) onto the substrates and do the lithography. Subsequently, Nb layer is sputtered or EB-evaporated. Finally we deposit Cu by the thermal evaporation after the lithography using the PMMA resist. We note that before depositing Cu, Ar-ion milling is carried out to clean the surface of the deposited metals. These fabrication procedures enable us to design more complex device structures, which is impossible through the shadow evaporation technique. One of the devices we have fabricated using these procedures is shown in Fig. 4.12(a). We first measured the temperature (T) dependence of the resistance R of a sputtered Nb and compared T_C with that of samples fabricated through the shadow evaporation technique. However, as shown in Fig. 4.12(b), Nb wires deposited by sputtering do not show superconducting transition at least down to 4 K. Even at room temperature, resistivity is much higher than that of Nb wires deposited by the EB evaporation. This might be due to contamination of Nb wires by the ZEP resist. During sputtering, Ar-ion plasma is generated in the process chamber, and this plasma can strip a fraction of the resist off the surface, which can be contained in Nb wires as impurities. Contamination of superconductors deposited by sputtering is also found to be a problem as seen in the next chapter.

We therefore next deposit Nb by using the EB evaporation in place of sputtering.

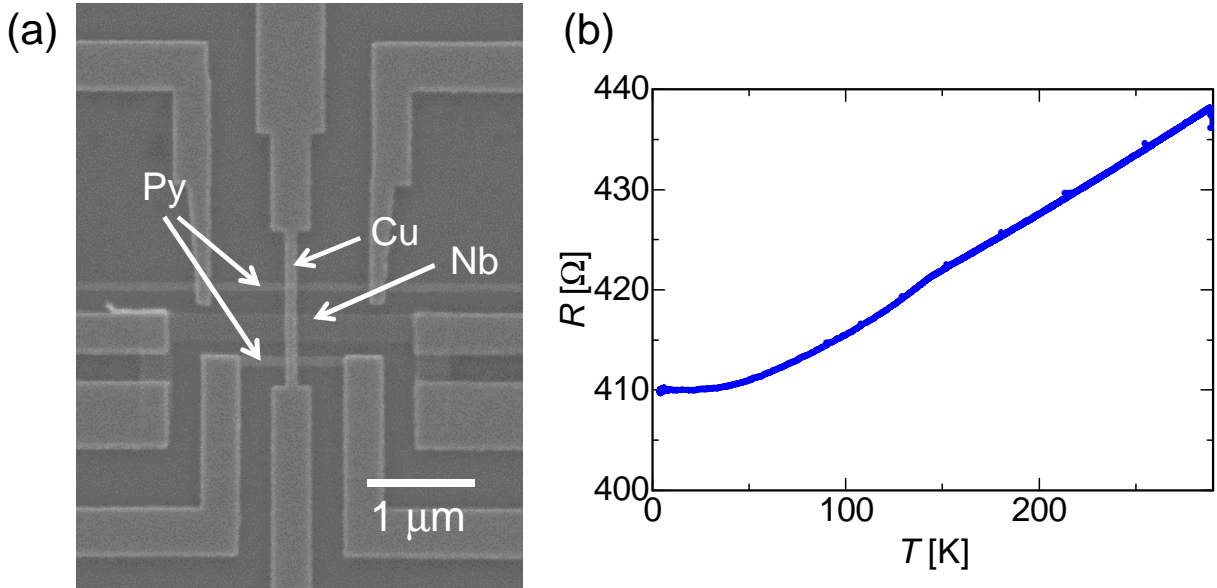


Figure 4.12: (a): SEM image of a device fabricated using sputtering technique to fabricate the Nb wire. (b): temperature (T) dependence of resistance (R) of the Nb middle wire. We cooled the sample down to 4 K, but R does not drop to zero. Similar behavior was reproduced for many samples prepared under the same condition.

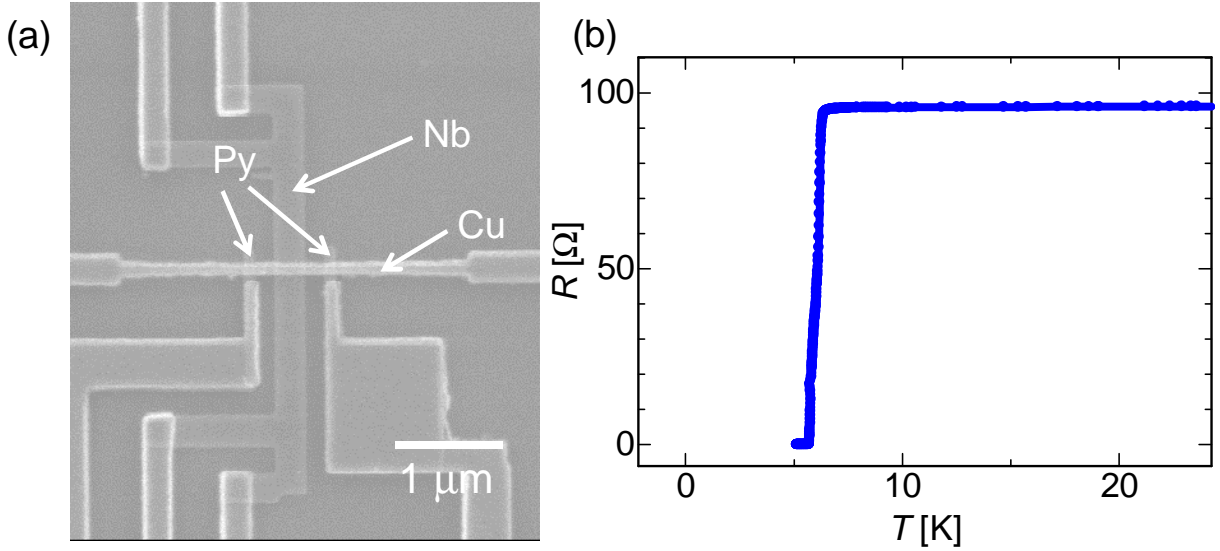


Figure 4.13: a): SEM image of a device fabricated using the EB evaporation technique to fabricate the Nb wire. (b): temperature (T) dependence of resistance (R) of the Nb middle wire. R shows a sharp drop at around 5.5 K, the same as T_C for samples prepared by the shadow evaporation technique.

Fabrication processes are the same as explained above apart from the Nb wires, but we note the design of the structure is slightly different (see Fig. 4.13). Nb is deposited normal to substrates in this case, while in the shadow evaporation it is evaporated to substrates at an angle of 45° from the surface of the substrate.

To enhance T_C of Nb, the deposition rate is a critical factor. In the shadow evaporation, the deposition rate inevitably becomes smaller than that of the normal evaporation. When we define an angle θ as the angle between the surface of the substrate and the direction of the beam of deposited particles, the deposition rate is reduced to $\cos \theta$. Thus we expect that Nb deposited normal to a substrate has higher T_C than that fabricated through the shadow evaporation because the deposition rate is nominally higher. However, T_C of Nb wires evaporated normal to the substrate shows almost the same as that of Nb deposited through the shadow evaporation. This signifies that the shadow evaporation does not affect superconductivity of Nb drastically. For these samples, we measured the spin injection current (I) dependence of the spin absorption into the Nb wires below T_C . Results are shown in Fig. 4.14. While the spin absorption of Nb wires fabricated by the shadow evaporation technique strongly depend on I below T_C , I dependence of ΔR_s is rather moderate. We note that the biggest difference between two sample fabrication processes is the transparency of the Nb/Cu interfaces. As explained above, in the shadow evaporation different materials can be deposited without breaking vacuum, thus Nb/Cu interface is almost perfectly trans-

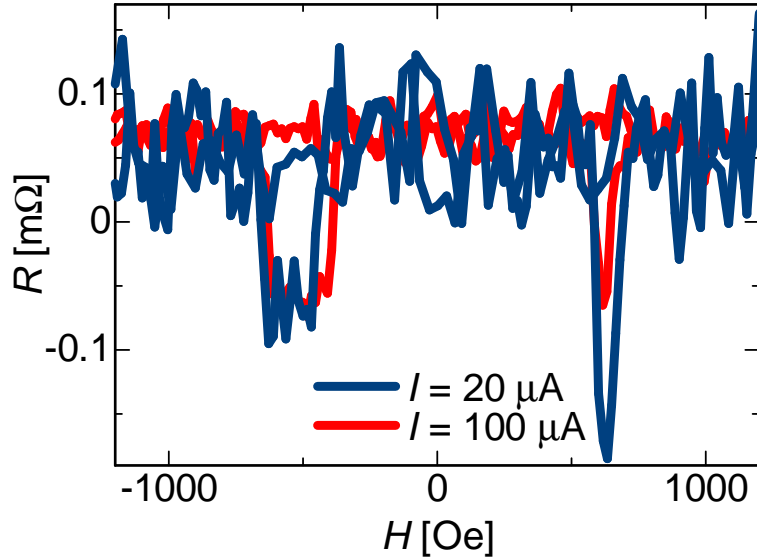


Figure 4.14: NLSV signals obtained from the sample with the Nb middle wire deposited by the EB evaporation and with breaking vacuum between two evaporation processes. Difference in the spin injection current I between the blue ($I = 20 \mu\text{A}$) and red ($I = 100 \mu\text{A}$) is not so clear compared with that from the sample fabricated through the shadow evaporation technique.

parent. On the other hand, in the fabrication process we use for the samples shown here the surface of materials is exposed to the atmosphere between the evaporation of different materials. Before the deposition of Cu, we carefully carry out the Ar-ion milling to remove contaminations or oxidized layers on the surface of Nb and Py wires. However, even if we do milling before depositing Cu, the interface between Cu and Nb is less transparent than that made without breaking vacuum [91]. To characterize the Nb/Cu interface, we measure the resistance of the region close to the interface between Nb and Cu (R_I), as we have done for samples made through the shadow evaporation technique. Figure 4.15(a) shows the T dependence of R_I . Clear peak at T_C is observed even for this interface, but absolute values of R_I both below and above T_C are much higher than those we observe for samples made through the shadow evaporation. The peak structure itself is also less sharp. These results indicate that Nb/Cu interface is less transparent for these samples. Based on these findings we can conclude that the interface between a normal metal and a superconductor is an important factor for I dependence of the spin absorption to occur. This is reasonable because we have found that the superconducting proximity effect is significant of this anomalous I dependence of the spin absorption, which is severely sensitive to the transparency of the interface between a normal metal and a superconductor. We note that Nb is known as a hydrogen-absorbed metal, thus once you expose Nb to the atmosphere, hydrogen

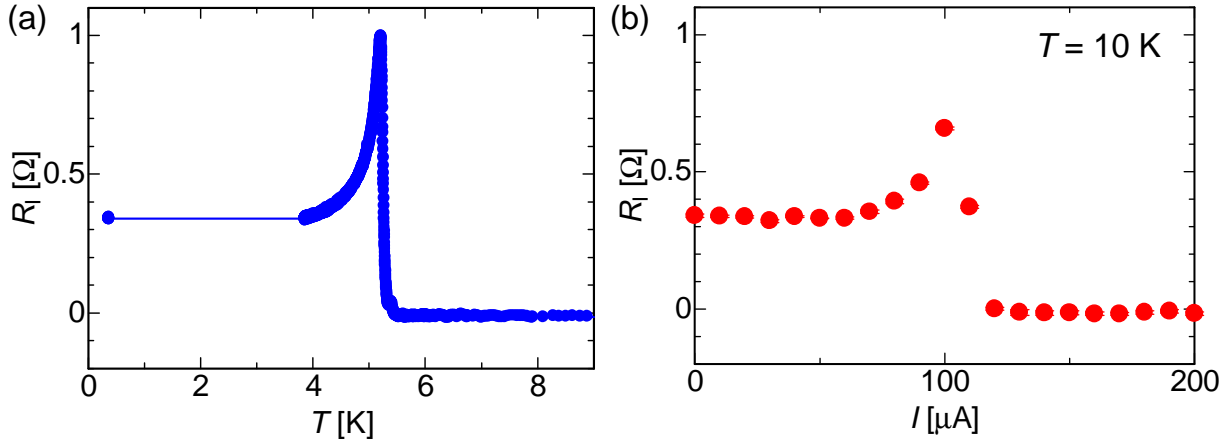


Figure 4.15: The resistance close to the Nb/Cu interface as a function of the temperature (T) in (a) and also the spin injection current (I) in (b).

adsorbes [92]. Properties of an hydrogen-absorbed interface should degrade, which might be one of the reasons why we cannot observe a clear I dependence of the spin absorption with *non in situ* samples. Interface transparency should be a critical problem for the spin injection into superconductors, and more studies are necessary for future work.

4.5 Brief summary

We have experimentally demonstrated the enhancement of the spin relaxation time τ_{sf} in a superconducting niobium. Our results show the more than four times enhancement in the superconducting state in comparison with that in the normal state. This order of magnitude is in good agreement with the theoretical calculation [28], but much smaller than that in the experimental value with aluminium [70], which shows million-folds enhancement. This considerable difference does not arise from the difference in materials, because another experiments on a superconducting Al [32] shows similar magnitude of enhancement when one focuses on the spin relaxation time in the zero magnetic field limit and large magnetic field limit (see Fig. 4c in [32]). Therefore some spurious effects may play a role in estimating τ_{sf} in [70]. Novel points in this study are summarized as follows:

(1) Spin transport properties are investigated in a superconductor with strong spin orbit coupling, niobium

In almost all previous studies on spin transport in superconductors, they used aluminum as a superconductor because it is easy to fabricate nanostructure with this superconducting material. However, aluminium has smaller SOI and is not attractive for

observing phenomena relevant to the SOI such as the SHE. In our study, we evaluate a fundamental spin transport property, spin relaxation time, in a superconducting niobium, which has much larger SOI than that of aluminium. This material is a good candidate for observing the SHE, and our results for niobium prompt studies on spin transport using different kinds of superconductors.

(2) Spin relaxation time is determined without spurious effects, and heating effect is precisely taken accounted.

In previous measurements, spurious effects like direct contact between a superconductor and a ferromagnet induced underestimation or overestimation of τ_{sf} . In our device structure, those effects are excluded, and heating effects due to the spin injection current, which are not evaluated in [71], are also considered. Our method to evaluate heating effects by means of the charge imbalance effect at the superconductor/normal metal interface is novel, and can be applied to other systems with superconductors.

(3) Spin relaxation time is evaluated by the Usadel equation.

There have never been reports which exploit the Usadel equation to estimate τ_{sf} . In this regard, our study opens a new way to calculate τ_{sf} in superconductors.

Chapter 5

Quasiparticle-mediated spin Hall effect in a superconductor

5.1 Introduction and Motivation

In the previous chapter we have investigated the spin injection and the spin relaxation in a superconducting Nb [90]. Experimental demonstrations of the enhanced spin relaxation time in the superconducting state are important both for science and future applications, and clearly indicates that distinctive phenomena can occur in su-

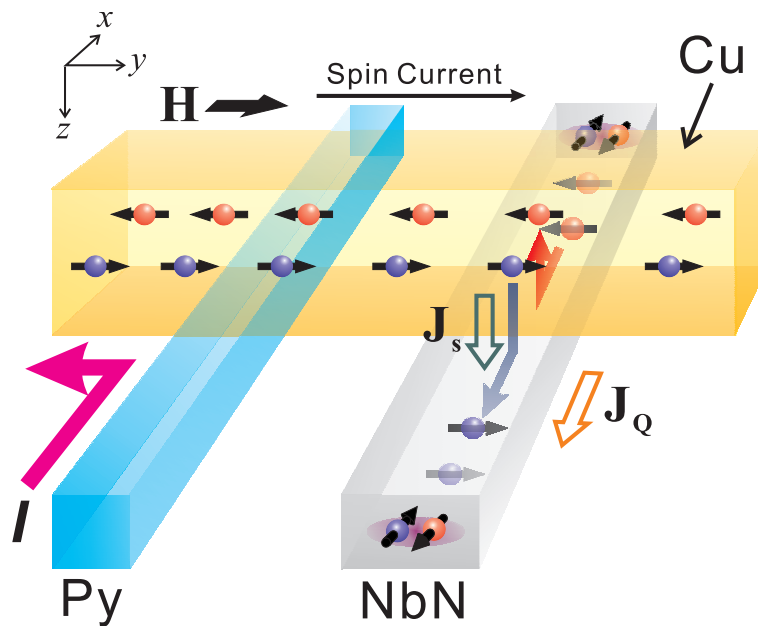


Figure 5.1: Schematic illustration of the device structure and experimental setup for the SHE measurements of a NbN superconductor. A Py spin injector and a NbN wire are bridged by a nonmagnetic Cu wire. By passing a current (spin injection current) between the Py and Cu wire, a pure spin current is generated in the Cu wire. This pure spin current is partly absorbed into the NbN wire and converted into charge currents. The ISHE signals are detected by the voltage probes at the edges of the NbN wire.

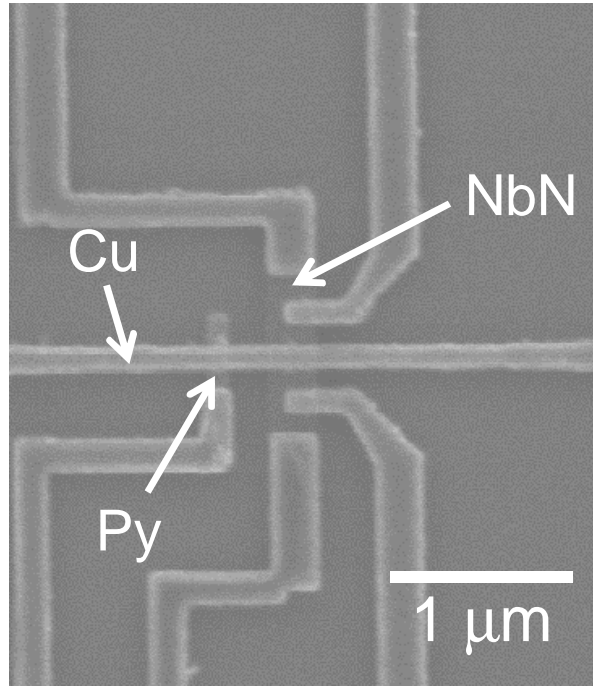


Figure 5.2: SEM image of the device for the SHE measurements.

perconductors not only for charge transport but also for spin transport. As discussed in the introductory chapters, the spin Hall effect (SHE), one of the most important phenomena in spintronics, is also predicted to exhibit drastically different behaviors in superconductors in comparison to that in normal metals. Theoretical work done by Takahashi and Maekawa [30] has proposed that in superconductors the SHE becomes dramatically large due to reduced superconducting quasiparticles, which mediate spin transport in superconductors. Very recently similar theoretical study on enhanced spin Hall conductivity in superconductors has been carried out by Gradhand *et al.* [93]. The SHE in superconductors is therefore highly intriguing and has potentiality to become a basis to discover many other novel phenomena for spintronics [94, 95, 96], but there have been no experimental reports on systematic study of the SHE in superconductors.

To detect the SHE in our system, we have to change the device structure from the one we used in the previous study. In the previous study, we utilized the shadow evaporation technique to fabricate devices *in situ*. However, the shadow evaporation technique severely limits the design of devices. For example, it is difficult to place voltage probes directly on the Nb middle wire using the shadow evaporation, because most part of the Nb is covered with Cu layer except in the region sufficiently close to the Nb/Cu interface (see the SEM image of the device in the previous chapter). As explained below, to detect the inverse spin Hall signals in superconductors, one has to put the voltage probes made by normal metal on top of superconductors. Therefore

to design device structures more flexibly and to detect the SHE, in this study we fabricate samples using sputtering and liftoff techniques. As shown in the last chapter, the superconductor/normal metal interface fabricated through these processes is less transparent than that prepared via the shadow evaporation, but the spin absorption experiments can be carried out as demonstrated by our previous studies [25, 26, 27]. In the fabrication process, we first do the electron beam (EB) lithography to a substrate with a resist. Each material is deposited after the EB lithography, then the sample is taken out from the chamber. After liftoff of the resist, we again do the EB lithography and repeat the same procedures for materials deposition. Details will be described below.

In this study we use niobium-nitride (NbN) as a superconductor. NbN is a type II superconductor [97]. The biggest advantage of using NbN is that its critical temperature (T_C) is much higher than that of Nb. The value from textbooks is $T_C = 9.2$ K (Nb) and $T_C = 16$ K (NbN) [97, 98]. Another advantage of NbN is that it is more stable in the atmosphere. Nb is known as a hydrogen adsorbing metal thus when exposed to the atmosphere, the surface of Nb absorbs hydrogen and its properties degrade. Weaker dependence of the spin absorption on the spin injection current for Nb superconductors fabricated by the evaporation and liftoff methods as shown in the last section may also be attributed to the hydrogen adsorption [92]. This is a severe problem also for our SHE measurements because we use the spin absorption technique and the surface of the wire (NbN) is the most sensitive part for the spin absorption effect.

We show in Fig. 5.2 the device structure and setup for measurements. A ferromagnetic Py and superconducting NbN wire are bridged by a nonmagnetic Cu wire. By passing a charge current (the spin injection current, I) between the Py and the Cu wire, we can generate a pure spin current in the Cu bridge. This pure spin current is partly absorbed into the NbN wire because it can relax faster in the NbN due to a large spin-orbit interaction (SOI) of NbN, than flowing in the Cu bridge. Since spin currents are nonequilibrium in nonmagnet, it is energetically favorable for spin currents to relax faster in the NbN wire. Through this process, we can inject a pure spin current into the NbN wire. The injected spin current is converted into a charge current via the inverse spin Hall effect (ISHE) so that a finite voltage difference is generated between the two edges of the NbN wire. The relation among the direction of the spin currents \mathbf{J}_S , the spin polarization of the spin currents \mathbf{s} and the charge currents generated by the ISHE \mathbf{J}_C is expressed as

$$\mathbf{J}_C \propto \mathbf{J}_S \times \mathbf{s}. \quad (5.1)$$

We note here that the direction of \mathbf{J}_S is normal to the NbN/Cu interface because ma-

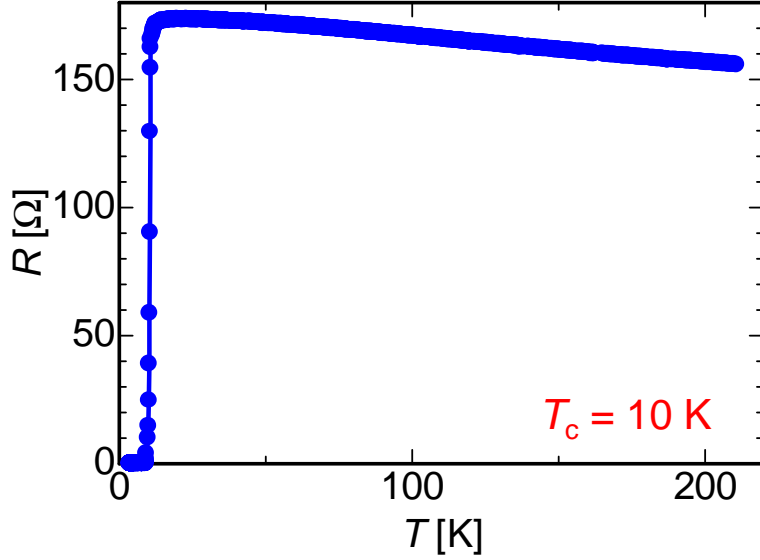


Figure 5.3: Temperature T dependence of the resistance R of the NbN wire. The resistance is slightly increasing with decreasing temperature, similar to the semiconductor regime. The sharp drop of R at 10 K indicates the onset of superconductivity.

materials with large SOI like NbN have smaller spin relaxation length than the thickness of the middle wire. In this regime, injected spin currents relax in the NbN wire within a short range from the interface with the Cu wire and do not spread out laterally. Considering the relation (5.1), to detect the voltage generated via the ISHE with the probe setup as shown in Fig. 5.2 s has to be directed normal to the longitudinal axis of the Py spin injector. To acquire s normal to the Py spin injector, during measurements we apply an inplane magnetic field perpendicular to the Py wire because s is parallel to the magnetization of the Py spin injector.

5.2 Experimental results

Devices are prepared by using the EB lithography, the EB or thermal evaporation and sputtering techniques. We first coated a thermally oxidized silicon substrate with the ZEP520A resist. After patterning by the EB lithography, a NbN film with 20 nm thickness was deposited by reactive sputtering technique. The base pressure was kept less than 8.0×10^{-5} Pa. These NbN films are deposited by reactive DC-magnetron sputtering in a mixture of Ar and N_2 gas. Sputtering of NbN is carried out by Prof. Akaike in Nagoya University. After liftoff we again do the EB lithography and Py was deposited using an EB evaporator normal to the substrate. Following the liftoff process, 100 nm of Cu was thermally evaporated onto the substrate. Before deposition of the Cu layer Ar-ion milling is performed to clean the interfaces. During the deposition the

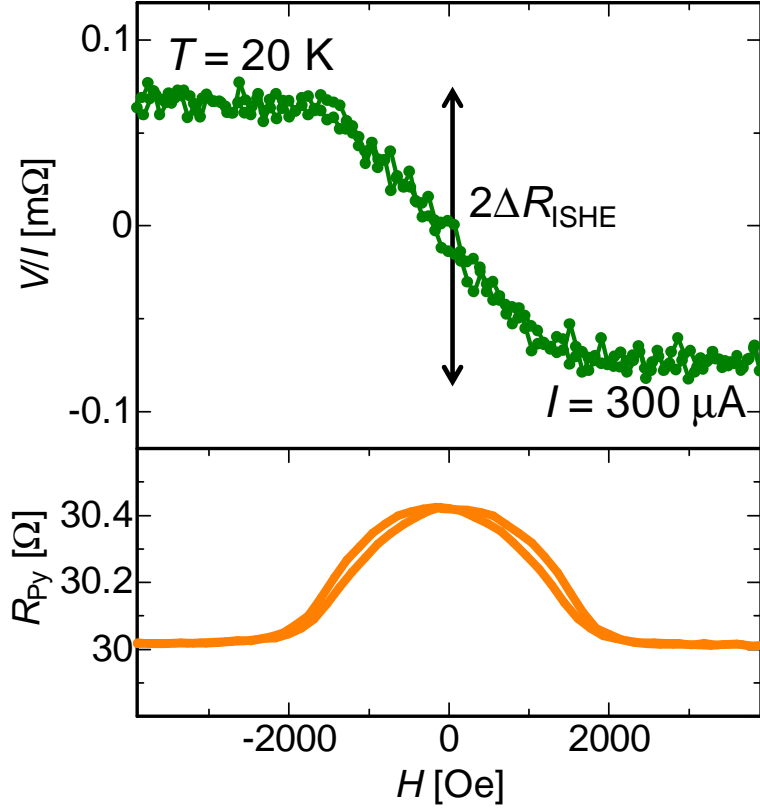


Figure 5.4: ISHE at $T = 20$ K, above T_C . The upper figure shows the observed voltage difference between the two edges of the NbN wire (V) divided by the spin injection current I as a function of the magnetic field H . The inverse spin Hall signal $2\Delta R_{\text{ISHE}}$ is defined as a difference between two saturated values in the large positive and negative H region. We note that $I = 300 \mu\text{A}$ in this measurement. The lower figure shows the AMR signal obtained with the Py spin injector. H is applied normal to the longitudinal axis of the Py. It is clear that the inverse spin Hall signal reflects the magnetization of the Py injector.

base pressure was kept less than 10^{-9} Torr. The SEM image of a device is shown in Fig. 5.2. The Width of the Py, NbN and Cu wires is 100 nm, 300 nm, and 100 nm, and 20 nm, 20 nm and 100 nm in thickness, respectively. Transport measurements are done by using a typical lockin technique with excitation currents of 173 Hz. Samples are equipped in a cryostat and cooled down by a flow of ^4He .

We first measure superconducting properties of the NbN wires. Figure 5.3 shows the temperature (T) dependence of the resistance (R) obtained from a NbN wire. R is slightly increasing with decreasing temperature, as a semiconductor-like behavior. This semiconductor-like behavior can be explained by the thermal hopping between grains in the NbN layer. Sharp drop of R to zero at 10 K then is observed, explicitly indicating a transition into the superconducting state of the NbN wire. From this T dependence of R of the NbN wire, we define the critical temperature (T_C) of this NbN

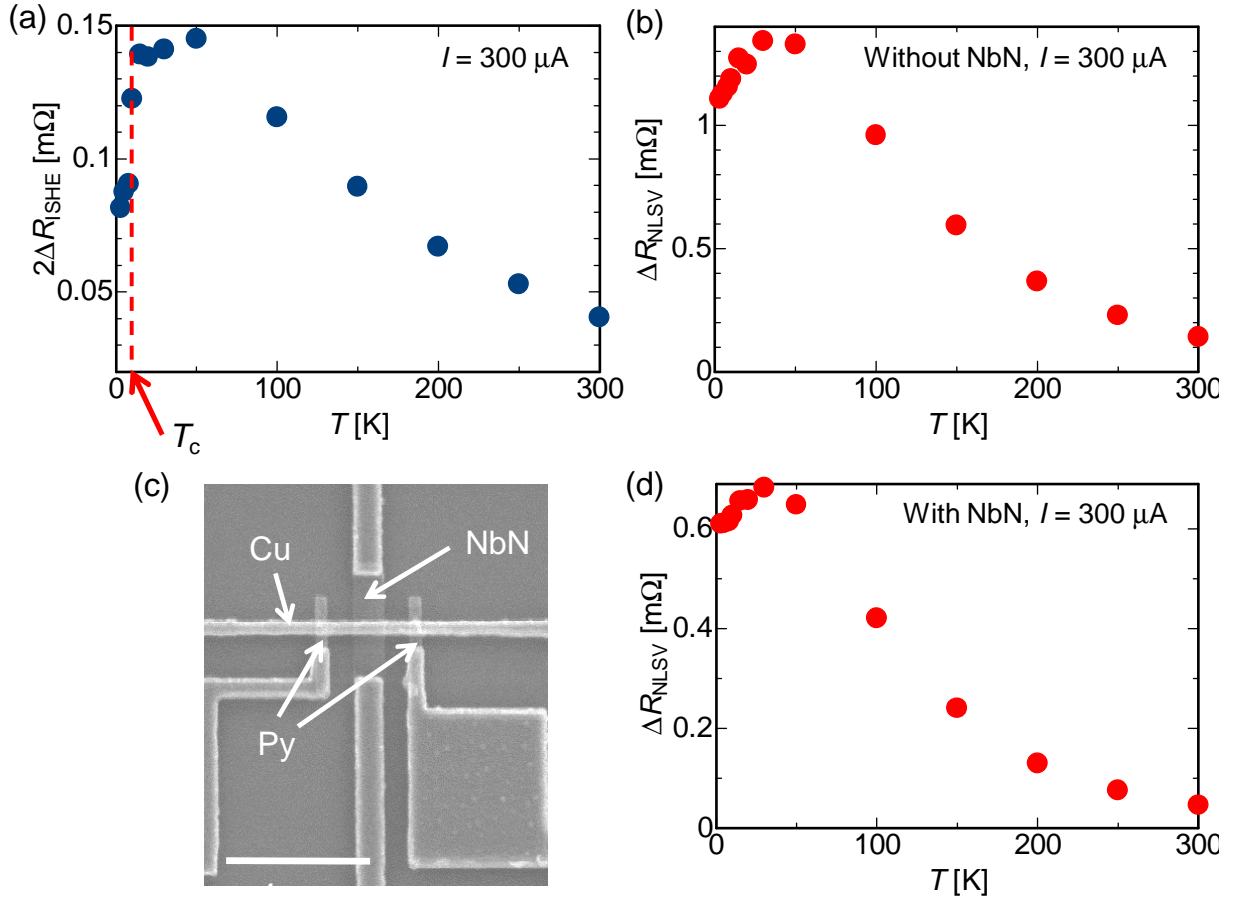


Figure 5.5: Temperature (T) dependence of ΔR_{ISHE} (a), ΔR_{NLSV} without (b) and with (d) the NbN middle wire. For the NLSV measurements we prepared an additional Py wire as a spin detector as shown in (c).

as 10 K. The resistivity ρ_{NbN} is $220 \mu\Omega\text{cm}$ slightly above T_c .

We then measure the ISHE at 20 K, above T_c . The obtained signal is shown in Fig. 5.4 with an anisotropic magnetoresistance (AMR) signal from the Py spin injector. H is an external magnetic field applied inplane and perpendicular to the Py spin injector. Because of the relation (5.1), by applying the inplane magnetic field we can control the direction of s , thus a finite voltage difference is generated between the two edges of the NbN wire in a large H region. The generated voltage difference becomes antisymmetric to $H = 0$ and changes its sign according to the positive or negative H regime (see Fig. 5.4). For $H > 2000$ Oe, the magnetization of the Py spin injector saturates, thus the inverse spin Hall signal also saturates. The inverse spin Hall signal $2\Delta R_{\text{ISHE}}$ is defined as $V/I(H = 2000 \text{ Oe}) - V/I(H = -2000 \text{ Oe})$ as indicated in Fig. 5.4. It can be clearly seen that the inverse spin Hall signal reflects the magnetization of the Py spin injector by comparing the inverse spin Hall signal with the AMR. We note that the spin injection current I is $300 \mu\text{A}$ in the measurements at 20 K.

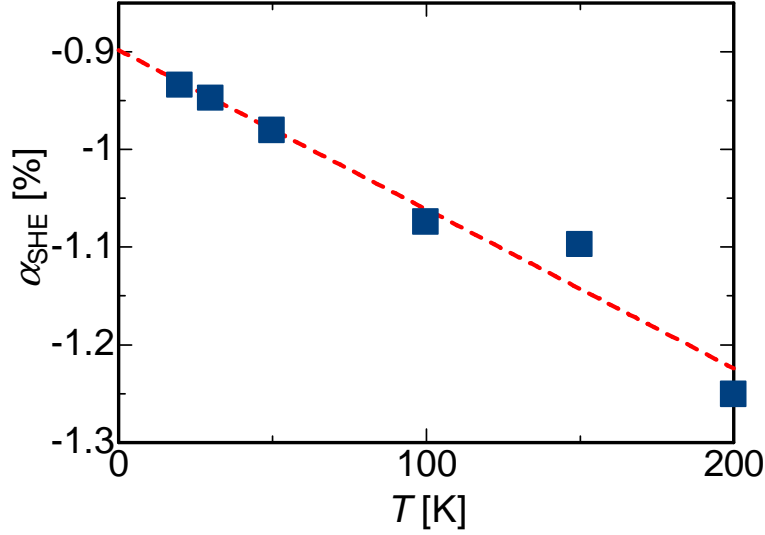


Figure 5.6: SH angle α_{SH} as a function of temperature. Linear relation between α_{SH} and T can be seen as guided by the red broken line.

To evaluate the magnitude of the SHE in materials, an important quantity is the spin Hall (SH) angle $\alpha_{\text{SH}} \equiv \rho_{\text{SHE}}/\rho_{xx}$, where ρ_{SHE} is the SH resistivity. ρ_{SHE} is related to the detected ΔR_{ISHE} through the equation [35]

$$\rho_{\text{SHE}} = \frac{w_{\text{M}}}{\zeta} \left(\frac{I}{I_{\text{s}}} \right) \Delta R_{\text{ISHE}}, \quad (5.2)$$

where w_{M} , ζ and I are the width of the NbN middle wire, a shunting factor and the spin injection current, respectively [26, 27]. I_{s}/I can be determined from the experimental values of the ratio of the NLSV signal with the NbN middle wire and without the middle wire by using the two equations written as (as already introduced in the previous chapter)

$$I_{\text{s}} = \frac{2PQ_{\text{Py}} (\sinh(L/2\lambda_{\text{sf}}^{\text{Cu}}) + Q_{\text{Py}} \exp(L/2\lambda_{\text{sf}}^{\text{Cu}}))}{\{\cosh(L/\lambda_{\text{sf}}^{\text{Cu}}) - 1\} + 2Q_{\text{NbN}} \sinh(L/\lambda_{\text{sf}}^{\text{Cu}}) + 2Q_{\text{Py}} \{e^{L/\lambda_{\text{sf}}^{\text{Cu}}} (1 + Q_{\text{Py}})(1 + 2Q_{\text{NbN}}) - 1\}} I, \quad (5.3)$$

and

$$\frac{\Delta R_{\text{s}}^{\text{with}}}{\Delta R_{\text{s}}^{\text{without}}} = \frac{2Q_{\text{NbN}} \left\{ \sinh(L/\lambda_{\text{sf}}^{\text{Cu}}) + 2Q_{\text{Py}} e^{L/\lambda_{\text{sf}}^{\text{Cu}}} + 2Q_{\text{Py}}^2 e^{L/\lambda_{\text{sf}}^{\text{Cu}}} \right\} I_{\text{s}}}{2PQ_{\text{Py}} (\sinh(L/2\lambda_{\text{sf}}^{\text{Cu}}) + Q_{\text{Py}} \exp(L/2\lambda_{\text{sf}}^{\text{Cu}}))} \frac{1}{I}, \quad (5.4)$$

where Q_{NbN} is the ratio of the spin resistance of NbN to that of Cu, namely, $Q_{\text{NbN}} = \mathcal{R}_{\text{NbN}}/\mathcal{R}_{\text{Cu}}$ and the other notations are the same as shown in the previous chapter.

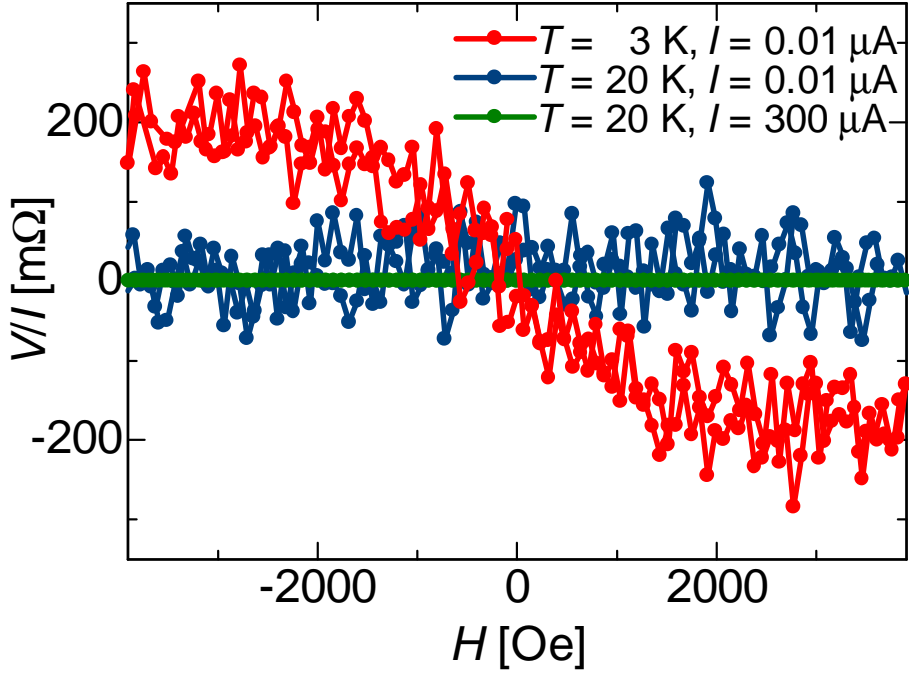


Figure 5.7: ΔR_{ISHE} taken at 3 K (red curve) in comparison with that at 20 K (blue and green curves). The signal at 3 K with $I = 0.01 \mu\text{A}$ shows enormously large value compared with that at 20 K with $I = 300 \mu\text{A}$. At 20 K, however, the signal is suppressed even if I is modulated to $0.01 \mu\text{A}$.

To estimate the SH angle of NbN above T_C , we measure the temperature dependence of ΔR_{ISHE} as shown Fig. 5.5(a). Temperature dependence of $\Delta R_{\text{NLSV}}^{\text{without}}$ and $\Delta R_{\text{NLSV}}^{\text{with}}$ are also shown in Fig. 5.5(b) and (d), respectively with the device SEM image in Fig. 5.5(c). Using these experimental values, we can plot the relation between the SH angle α_{SH} and T as in Fig. 5.6. As T decreases, α_{SH} linearly increases. The SH resistivity ρ_{SHE} is composed of two terms:

$$\rho_{\text{SHE}} = a\rho_{xx} + b\rho_{xx}^2, \quad (5.5)$$

where ρ_{xx} is the longitudinal resistivity and a and b are both constants. The first term is ascribed to the skew scattering contribution and the second term to the intrinsic and/or side-jump contribution (see Section 2). By dividing both sides by ρ_{xx} , we obtain

$$\alpha_{\text{SH}} = a + b\rho_{xx}. \quad (5.6)$$

From the temperature dependence of the resistance of NbN, we can find the linear relation between ρ_{xx} and T , namely, $\rho_{xx} \propto T$ from slightly above T_C . By substituting this relation into (5.6), we can determine the constants a and b .

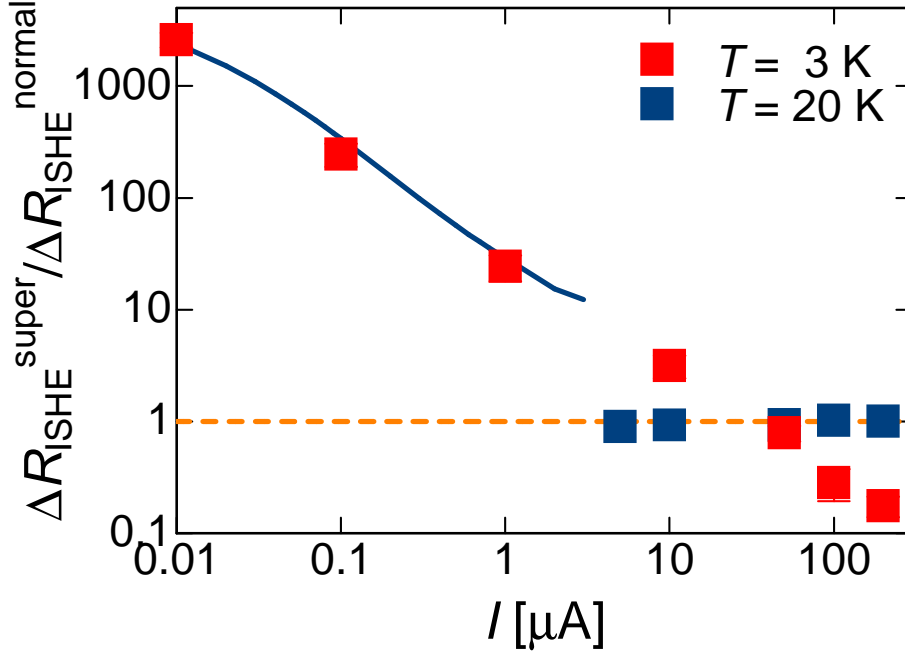


Figure 5.8: Inverse spin Hall signals ΔR_{ISHE} as a function of the spin injection current I taken at 3 K (red squares) and 20 K (blue squares). At 20 K ΔR_{ISHE} is almost independent of I . On the contrary, at 3 K, ΔR_{ISHE} gigantically increases with decreasing I . The error bars are evaluated with the standard deviations of ΔR_{ISHE} for $H > 2000$ Oe and $H < -2000$ Oe. The solid line is obtained from the calculations (see the main text).

By using the temperature dependence of α_{SH} we may decide a dominant contribution to the SHE. While (5.5) is a typical notation to express the Hall angle with ρ_{xx} , there are controversies to deal with extrinsic contributions (skew scattering and side-jump contribution) with temperature-dependent ρ_{xx} [99]. Hence we do not discuss this issue further.

To investigate the SHE in the superconducting state, we next cool the sample down to 3 K, much below T_C and carry out the same measurements. We fix the sample temperature to 3 K, and change the spin injection current I . With $I = 300 \mu\text{A}$, as we used for $T > T_C$, the signal ΔR_{ISHE} slightly suppresses. With $I = 100$ and $200 \mu\text{A}$, ΔR_{ISHE} becomes more suppressed. However, when we decrease I further, the signal then increases again. For $I < 100 \mu\text{A}$, ΔR_{ISHE} shows an order of magnitude enhancement for each I , and with $I = 0.01 \mu\text{A}$, the signal becomes more than 2000 times larger than that in the normal state (at 20 K). Signals taken at 3 K are shown in Fig. 5.7 in comparison with that obtained at 20 K as an example. Compared with ΔR_{ISHE} at 20 K with $I = 300 \mu\text{A}$, that at 3 K with $I = 0.01 \mu\text{A}$ clearly exhibits a much larger value. On the other hand, even if I is modulated to $0.01 \mu\text{A}$ at 20 K, the signal is still suppressed and does not show any enhancement. Relation between

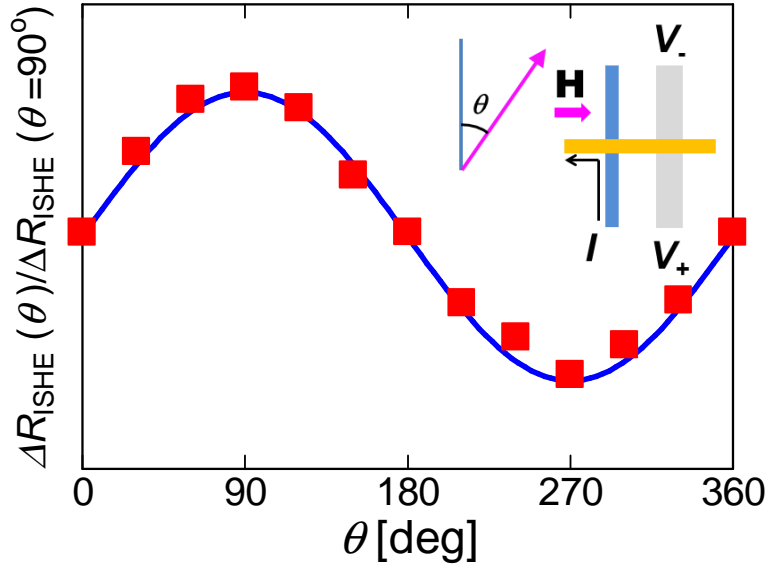


Figure 5.9: Angular dependence of ΔR_{ISHE} . Angle θ is defined as the angle between \mathbf{H} and the longitudinal axis of the Py spin injector (see the inset). Experimental data (red squares) show the sinusoidal dependence on θ as expected for the inverse spin Hall signals.

ΔR_{ISHE} and I is shown in Fig. 5.8 both at 3 K and 20 K. At 20 K, the signals are almost independent of I . However, at 3 K ΔR_{ISHE} , strongly depends on I and shows enhancement with decreasing I .

To confirm that the obtained signals are originated from the ISHE, we measure dependence of ΔR_{ISHE} on the direction of \mathbf{H} . Taking into account the relation (5.1), ΔR_{ISHE} changes when the direction of \mathbf{s} is controlled by \mathbf{H} . We take the angle θ as an angle between \mathbf{H} and the longitudinal axis of the Py spin injector (as shown in the inset of Fig. 5.9), if the signals are from the ISHE, from (5.1) they should follow the relation as

$$\Delta R_{\text{ISHE}} = \Delta R_{\text{ISHE}}(\theta = 90^\circ) \sin \theta. \quad (5.7)$$

We change the angle θ and measure $\Delta R_{\text{ISHE}}(\theta)$. Results are shown in Fig. 5.9. The red squares are experimental data, and the blue curve is a function $\sin \theta$. Experimental signals follow well the sinusoidal relation to θ , which corroborates that the signals are derived from the ISHE.

We next investigate how superconductivity plays a role to this anomalously gigantic SHE. The biggest difference between the ISHE in normal metals and that in superconductors is that in normal metals injected spin currents are converted into electrical currents via the ISHE, but in superconductors they are converted into quasiparticles currents because in superconductors quasiparticles mediate spin transport [80, 30]. Superconducting (Bogoliubov) quasiparticles are regarded as a superposition

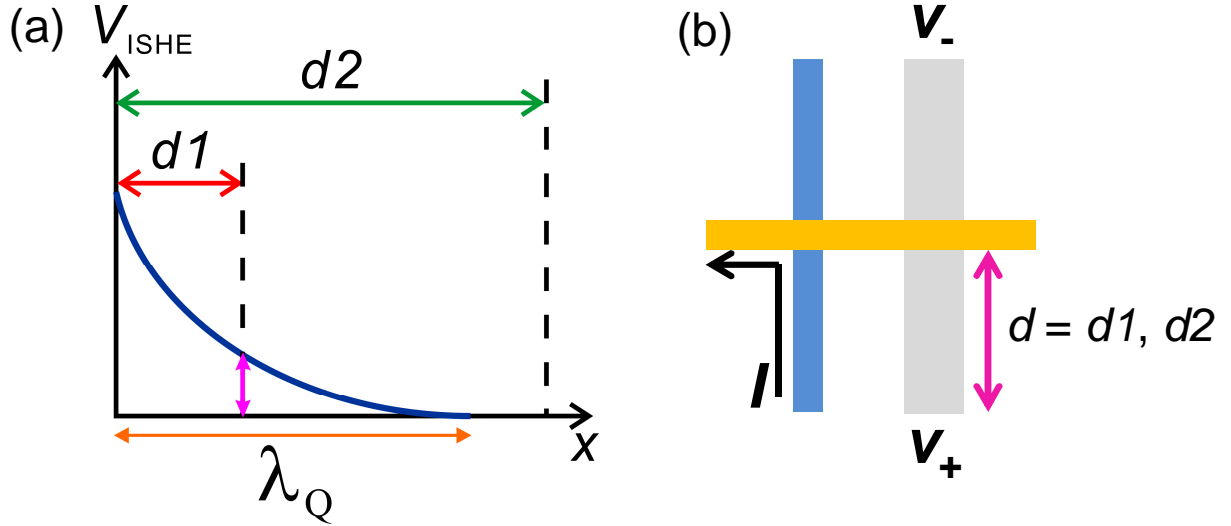


Figure 5.10: Schematic image of the relation among λ_Q , $d1$ and $d2$. (a): the voltage generated by the ISHE (V_{ISHE}) decays in λ_Q . For $d1 \ll \lambda_Q$, V_{ISHE} can be detected, while at $d2 \gg \lambda_Q$ V_{ISHE} is severely suppressed. (b): $d = d1, d2$ is defined as a distance between the NbN/Cu crossjunction and a voltage probe at an edge of NbN.

of electron-like and hole-like excitations. At equilibrium and at finite temperature, the number of quasiparticles in the electron-like branch and hole-like branch is balanced [88]. However, when electrons are externally injected or the ISHE occurs, the balance between the branches is broken and the system is brought into a nonequilibrium state [80, 30]. Since this is a nonequilibrium state, the system has to relax into the equilibrium state. During this relaxation process, there is a charge accumulation process called the charge imbalance (CI) effect [75]. The charge imbalance effect originates from the imbalance between electron-like and hole-like excitations of quasiparticles. The CI relaxes in a certain time or length scale. The length within which the CI relaxes is called the charge imbalance length and expressed with λ_Q . λ_Q for typical superconductors is well investigated, and for Al, for example, λ_Q^{Al} is $\sim 5 \mu\text{m}$ [100]. We note that the temperature dependence of λ_Q is expressed as

$$\lambda_Q = \frac{\lambda_Q^0}{(1 - T/T_C)^{1/4}} \quad (5.8)$$

as discussed in [101].

The CI generated by the ISHE can be detected by voltage probes made by normal metals. We note that in this nonequilibrium state we can assume the chemical potential (CP) of quasiparticles and Cooper pairs [76, 77]. The CP of quasiparticles can be measured only by normal metal voltage probes while that of Cooper pairs is detected by superconducting voltage probes [80, 30]. Thus to detect the CI signal generated by

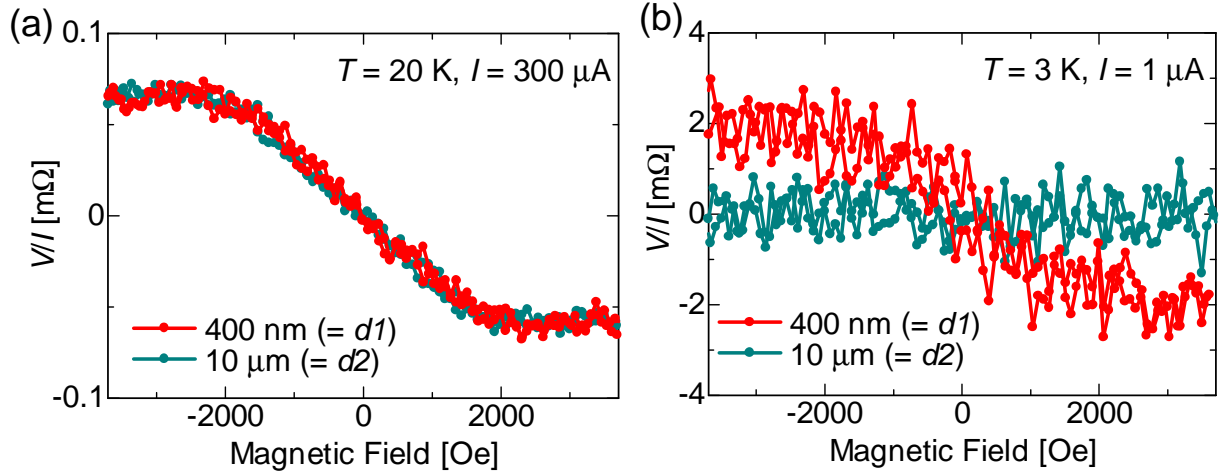


Figure 5.11: Inverse spin Hall signals from the samples with $d = d1$ and $d = d2$ taken at both 3 K and 20 K. (a): Signals at 20 K. Both samples show almost the same value of the signals. (b): Data at 3 K. While ΔR_{ISHE} from the sample with $d1$ shows $m\Omega$ order large value, that from the device with $d2$ is strongly suppressed.

the ISHE, one has to use normal metal voltage probes, which must be placed within the CI length from the region where the ISHE occurs because of the relaxation of the CI. In our NbN devices, due to the small λ_{sf} of NbN, the ISHE occurs just below the NbN/Cu crossjunction, so the distance between the crossjunction and a voltage probe ($\equiv d$) should be less than λ_Q^{NbN} to detect the inverse spin Hall signal through the CI effect. We prepare two samples with different d to confirm that the ISHE is mediated by the CI effect, specific to superconductors. One of the two samples has $d = 0.4 \mu m$ ($\equiv d1$), and the other is $d = 10 \mu m$ ($\equiv d2$). The CI length for NbN λ_Q^{NbN} is not well investigated, and for reference we take the value of that for Al $\lambda_Q^{Al} = 5 \mu m$ [100]. Compared with this CI length, $d1 \ll \lambda_Q$ and $d2 \gg \lambda_Q$. Relation among λ_Q , $d1$ and $d2$ is schematically shown in Fig. 5.10(a), and the definition of $d1$ and $d2$ is also described in Fig. 5.10(b).

We measure the ISHE for the two samples both at 20 K and at 3 K. Results are shown in Fig. 5.11. At 20 K, these two signals show almost the same values. However, at 3 K, while the signal from the sample with $d1$ is an order of $m\Omega$, that from the sample with $d2$ is strongly suppressed. These results clearly demonstrate that the ISHE is mediated by quasiparticles and the CI effect, both of which are derived from superconductivity of NbN.

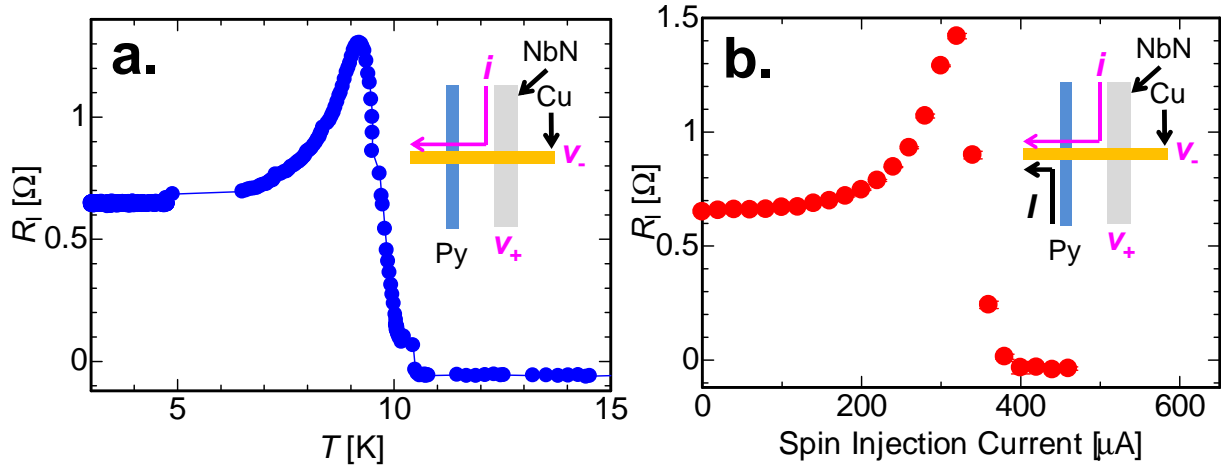


Figure 5.12: Resistance close to the NbN/Cu interface R_I as a function of temperature T (a) and the spin injection current I (b). These curves show the same shape as in results for the Nb/Cu interface measurements.

5.3 Analyses

To explain the anomalously large enhancement of the ISHE in a superconducting NbN, we first investigate the resistance close to the NbN/Cu interface ($\equiv R_I$) as we have done in the previous study for the spin absorption into Nb. Figure 5.12 (a) and (b) show the T and I dependence of R_I , respectively. Insets display the measurement setups for each experiment. As observed in the previous study, the T dependence and I dependence of R_I correspond to each other. By comparing these two curves we can derive the relation between the effective temperature at the NbN/Cu interface (T_{eff}) and I . In this study, measurements are carried out at higher temperature (3 K) than that of the previous experiments for Nb (370 mK). Thus we consider contributions from both electrons and phonons to temperature dependence of energy in the Cu bridge:

$$\varepsilon = \gamma T^2 + AT^4, \quad (5.9)$$

where T_0 is the environmental temperature, here 3 K. When the temperature T deviates from the bath temperature T_0 , the net increase of ε is written as

$$\Delta\varepsilon = \gamma(T^2 - T_0^2) + A(T^4 - T_0^4). \quad (5.10)$$

Heat generated by the Py spin injector can be expressed as

$$Q = R_{\text{Py}} I^2 t, \quad (5.11)$$

where $t = L^2/D$ with the length of the Py injector L and the Py diffusion constant D . By equating (5.10) times the volume of the Cu bridge V and (5.11), we obtain

$$I^2 = \frac{\gamma V}{R_{\text{Py}} t} (T^2 - T_0^2) + \frac{AV}{R_{\text{Py}} t} (T^4 - T_0^4). \quad (5.12)$$

We plot the experimental data of relation between I and T as shown in Fig. 5.13. Fitting for I^2 with $(T - T_0)^2$ and $(T - T_0)^4$ reproduces well the experimental results as shown with the blue curve. From the fitting, we can derive both γ and A experimentally. In the reference, the value of these quantities is $\gamma = 94 \text{ J}\cdot\text{m}^{-3}\cdot\text{K}^{-2}$ and $A = 8.7 \text{ J}\cdot\text{m}^{-3}\cdot\text{K}^{-4}$. We note that to derive A , we use the equation for the low temperature specific heat c_v based on the Debye model:

$$c_v = \frac{12\pi^4}{5} n k_{\text{B}} \left(\frac{T}{\Theta_{\text{D}}} \right)^3, \quad (5.13)$$

where n is the number of ions in a unit volume, Θ_{D} is the Debye temperature. We use $n = 6.02 \times 10^{23} \text{ mol}^{-1}$, the mass number of Cu 63.55, the density of Cu $8.96 \text{ g}/\text{cm}^3$. Experimentally obtained values, on the other hand, are $\gamma = 64 \text{ J}\cdot\text{m}^{-3}\cdot\text{K}^{-2}$ and $A = 5.1 \text{ J}\cdot\text{m}^{-3}\cdot\text{K}^{-4}$, in good agreement with the values from the reference. This result strongly supports the validity of our simple model to estimate the effective temperature increase at the NbN/Cu interface due to I .

We briefly comment on more refined models to evaluate the effective temperature at the NbN/Cu interface. Precisely speaking, it is better to consider the temperature difference in the Cu bridge based on the Wiedemann-Franz law, and also to define different temperatures for electrons, phonons and the substrate as discussed in [102]. Based on the model in [102], we roughly estimate these effects. First, the temperature difference in the Cu bridge between the Py spin injector and the NbN wire is evaluated, and found to be $< 0.1 \text{ K}$. This is because the distance between the two wires is relatively short (400 nm), and Cu is a good thermal conductor. Second, we calculate the electron-phonon length $l_{\text{e-ph}}$ in the Cu bridge. This quantity characterizes the strength of the electron-phonon coupling, and if we assume a system size L , for $l_{\text{e-ph}} \ll L$, the electron-phonon coupling is strong in this system and we can define the same temperature for electrons and phonons. If $l_{\text{e-ph}} \gg L$, electrons and phonons are decoupled in this system and different temperatures for electrons and phonons can be considered. $l_{\text{e-ph}}$ can be calculated as [102, 103]

$$l_{\text{e-ph}} = \frac{1.31}{\sqrt{T^3 \Gamma}}, \quad (5.14)$$

where Γ is a parameter for the electron-phonon coupling. For reference we use $\Gamma = 5 \times 10^9 \text{ m}^{-2} \text{ K}^{-3}$ for gold [102], we obtain $l_{\text{e-ph}} \approx 3 \mu\text{m}$. This value is larger than the system size of our device, but we assume the same temperature for electrons and phonons at 3

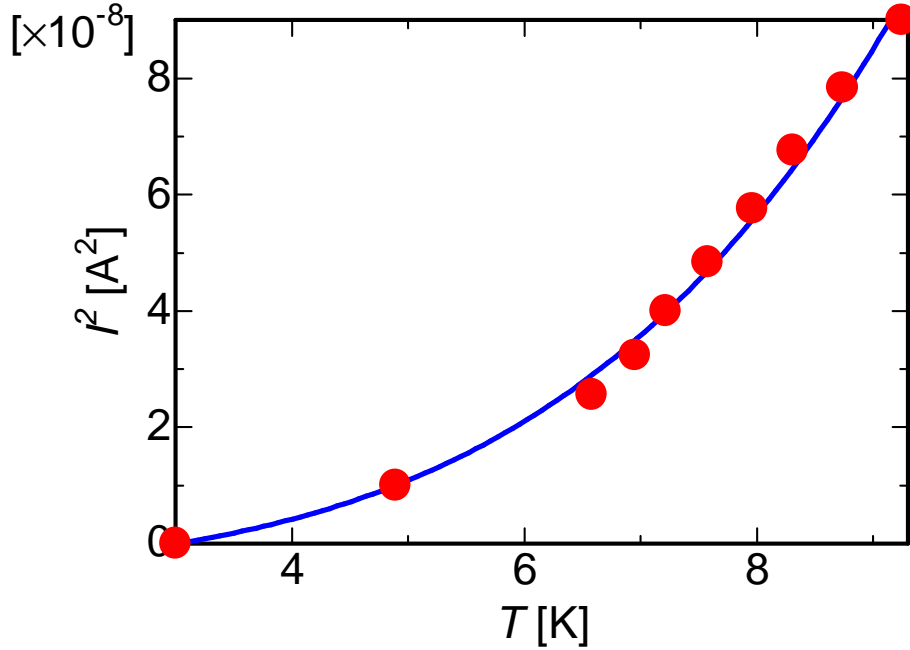


Figure 5.13: Relation between I and the effective temperature at the NbN/Cu interface T_{eff} . The red dots are the experimentally obtained values, and the blue curve is a theoretical fit using the relation $I^2 = p(T^2 - T_0^2) + q(T^4 - T_0^4)$ where p and q are both constants and fitting parameters. The calculated curve produces the experimental data very well.

K in the following reasons: In our experiments we carry out the measurements above 3 K. As many previous studies on the temperature dependence of the dephasing time in metals, above 3 K the electron-phonon coupling become stronger with increasing temperature [104]. Thus it is not reasonable to think that the phonons are decoupled from the electrons in our system and have different temperatures.

We also remark on the temperature difference between phonons and the substrate subsystem. Thermal coupling between the two systems is determined by the Kapitza resistance [102, 103]. The phonon temperature (T_{ph}) is related to the temperature of the substrate (T_{sub}) with the equation [102, 103]:

$$T_{\text{ph}} = \left(T_{\text{sub}}^4 + \frac{P}{A\sigma_K} \right)^{1/4}, \quad (5.15)$$

where P is the power, A is the area of the reservoir, and the σ_K is a parameter specific to the interface between the reservoir and the substrate. When the second term is much larger than the first term in (5.15), we can neglect the temperature difference between them, and in the opposite regime, different temperatures can be assumed for

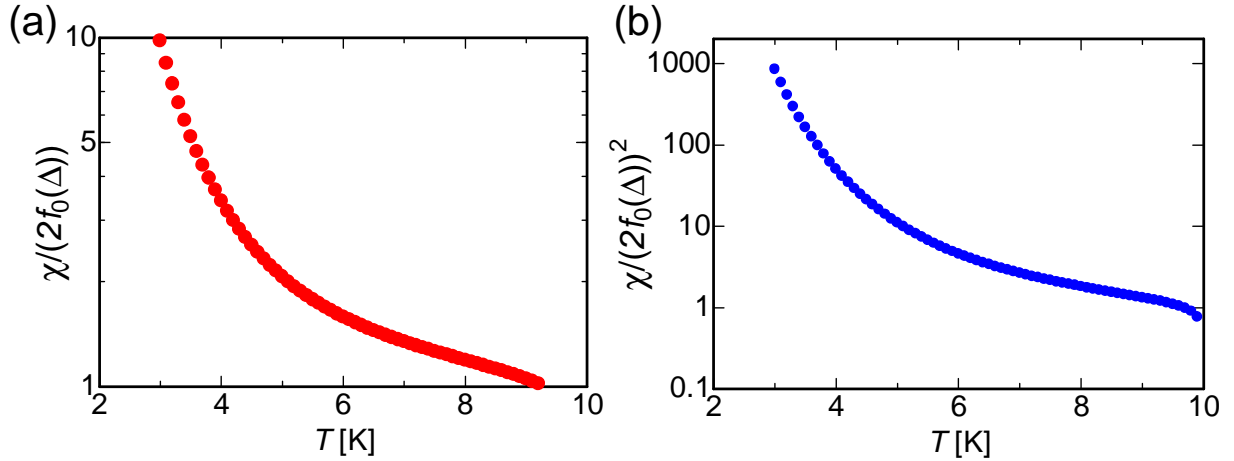


Figure 5.14: Results of numerical calculations for $\chi/f_0(\Delta)$ (a) and $\chi/(f_0(\Delta))^2$ (b).

the two systems. If we define $\Delta T^4 \equiv P/(A\sigma_K)$, σ_K is written as

$$\sigma_K = \frac{P}{A\Delta T^4}. \quad (5.16)$$

If we substitute several kelvins to ΔT , reasonable values in our measurements, and P with R_{PY} and the spin injection current I , we can obtain values of σ_K . The obtained values are much smaller than that shown in the reference [102] as the worst case ($\sigma_K = 100 \text{ W/m}^2 \text{ K}^4$). In our system we can assume the same temperature for the bath (T_{bath}) and the substrate because the relation between them can be written as [102]

$$T_{\text{sub}} = (T_{\text{bath}}^2 + aP)^{1/2} \quad (5.17)$$

where a is a parameter. When we use $a = 1.31 \times 10^5 \text{ K}^2/\text{W}$, $aP \ll T_{\text{bath}}^2$ in our measurements. Based on these facts, we can assume that T_{sub} is the same as the bath temperature, and temperature difference between the bath (namely the substrate) and the device because of the small thermal conductivity between them at low temperatures. To explain our data, we next theoretically investigate how the SHE is modulated with decreasing I below T_C . We note that the model we establish is a phenomenological model. Since spin transport is mediated by quasiparticles in superconductors, in (5.5) the longitudinal resistivity of electrons ρ_{xx} must be replaced by that of superconducting quasiparticles ρ_{qp} , which can be expressed as [29]

$$\rho_{\text{qp}} = \frac{\rho_{xx}^0}{2f_0(\Delta)}, \quad (5.18)$$

where $f_0(\Delta) = 1/(\exp(\Delta/k_B T) + 1)$ is the Fermi distribution function at the superconducting gap Δ , and ρ_{xx}^0 is the longitudinal resistivity just above T_C . By substituting

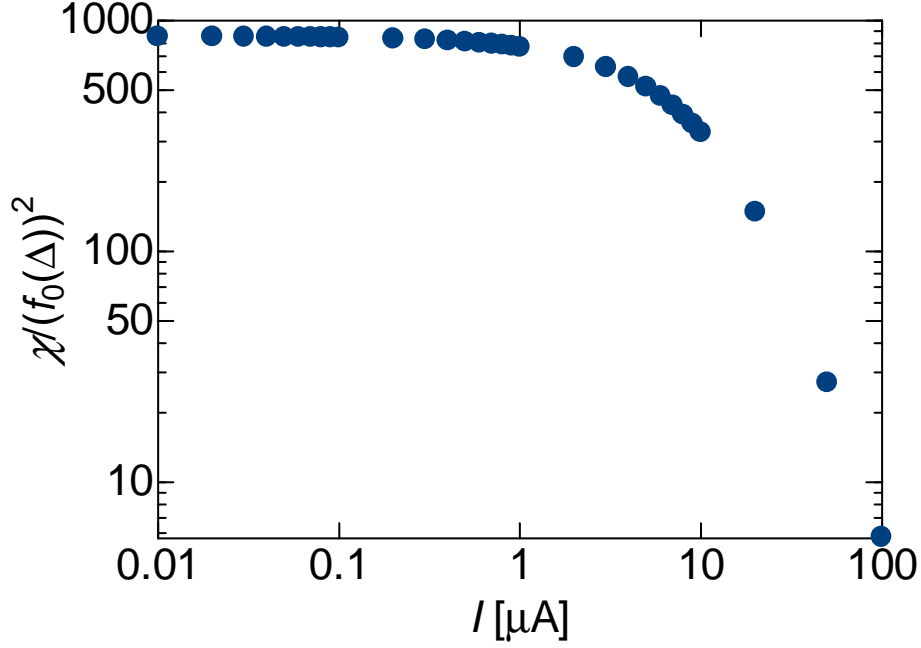


Figure 5.15: Calculated $\Delta R_{\text{ISHE}}^{\text{super}}/\Delta R_{\text{ISHE}}^{\text{normal}}$ as a function of I using the relation between I and T as shown in (5.29) directly. We cannot reproduce the experimental results due to the saturated values in a small I region.

(5.18) into (5.5), we obtain

$$\rho_{\text{SHE}}^{\text{super}} = a \frac{\rho_{xx}^0}{2f_0(\Delta)} + b \left(\frac{\rho_{xx}^0}{2f_0(\Delta)} \right)^2. \quad (5.19)$$

Using the relation (5.2) between ρ_{SHE} and ΔR_{ISHE} , in a superconducting state the inverse spin Hall signal is written as

$$\Delta R_{\text{ISHE}}^{\text{super}} = \frac{\zeta^{\text{super}}}{w_{\text{M}}} \left(\frac{I_{\text{s}}^{\text{super}}}{I} \right) \left[a \frac{\rho_{xx}^0}{2f_0(\Delta)} + b \left(\frac{\rho_{xx}^0}{2f_0(\Delta)} \right)^2 \right], \quad (5.20)$$

where ζ^{super} and $I_{\text{s}}^{\text{super}}$ are the shunting factor and the spin currents injected into the NbN wire in the superconducting state, respectively. Thus at a certain I , the ratio of $\Delta R_{\text{ISHE}}^{\text{super}}$ to $\Delta R_{\text{ISHE}}^{\text{normal}}$ becomes

$$\frac{\Delta R_{\text{ISHE}}^{\text{super}}}{\Delta R_{\text{ISHE}}^{\text{normal}}} = \frac{\zeta^{\text{super}}}{\zeta^{\text{normal}}} \frac{I_{\text{s}}^{\text{super}}}{I_{\text{s}}^{\text{normal}}} \frac{a(\rho_{xx}^0/2f_0(\Delta)) + b(\rho_{xx}^0/2f_0(\Delta))^2}{a\rho_{xx}^0 + b(\rho_{xx}^0)^2}. \quad (5.21)$$

The term $I_{\text{s}}^{\text{super}}/I_{\text{s}}^{\text{normal}}$ can be calculated using the relation

$$\frac{I_{\text{s}}^{\text{super}}}{I_{\text{s}}^{\text{normal}}} = \int_{-\infty}^{\infty} n_{\text{S}}(E) \left(-\frac{\partial f_0(E)}{\partial E} \right) dE, \quad (5.22)$$

where $n_{\text{S}}(E)$ is normalized density of states (DOS) of the NbN wire and $f_0(E) =$

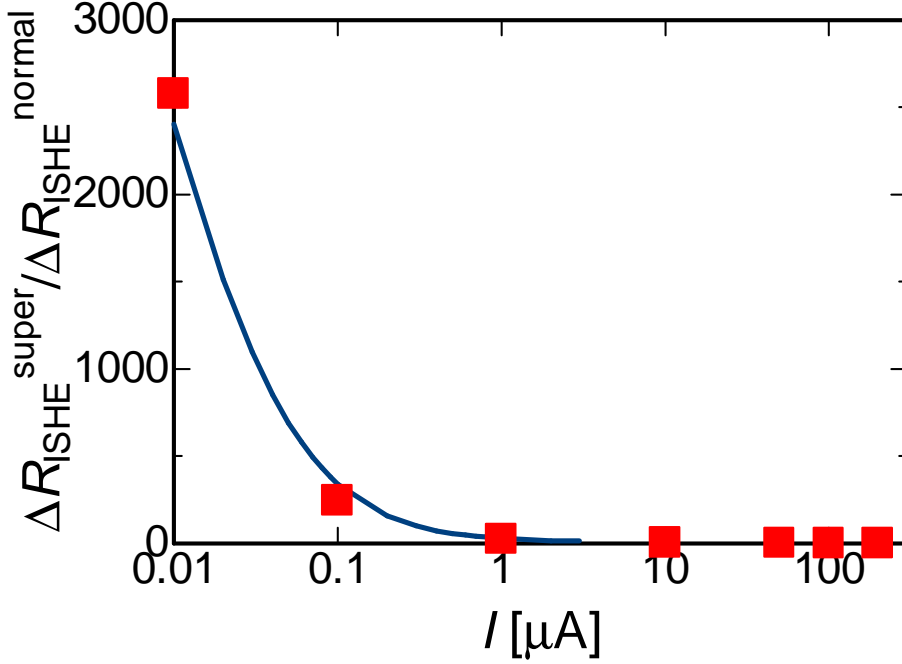


Figure 5.16: Ratio $\Delta R_{\text{ISHE}}^{\text{super}} / \Delta R_{\text{ISHE}}^{\text{normal}}$ as a function of I . Red dots are experimental values, and blue line is calculated value using the relation in (5.30). Calculated curve reproduces experimental results well in a small I region.

$1/(\exp(E/k_{\text{B}}T) + 1)$, the Fermi distribution function. According to the BCS theory, $n_{\text{S}}(E)$ can be written as [88]

$$n_{\text{S}}(E) = \frac{|E|}{\sqrt{E^2 - \Delta^2}}. \quad (5.23)$$

In our system, the superconducting NbN wire is directly attached to the normal metal Cu. Thus suppression of the superconducting gap Δ is expected. We note that as explained above, the proximity effect between the NbN and Cu wire is weak because of the less transparency at the interface between them. Moreover, Ar-ion milling we carry out before depositing Cu onto the NbN wire can cause a damage at the surface of NbN and suppress superconductivity at the interface of the NbN [105]. For these reasons, we assume that the superconducting gap is suppressed at the NbN/Cu interface. To account for this gap suppression, we assume that Δ be spatially dependent and described as

$$\Delta = \frac{x}{\xi} \Delta_0, \quad (5.24)$$

where ξ is the Pippard's coherence length and x is distance from the NbN/Cu interface. We have attempted to use different spatial dependence of $\Delta(x)$ such as quadratic in x or exponential decrease, and confirmed that these spatial dependences do not affect the final results qualitatively. In this calculation, we take $\Delta(x) = 0$ at $x = 0$. This

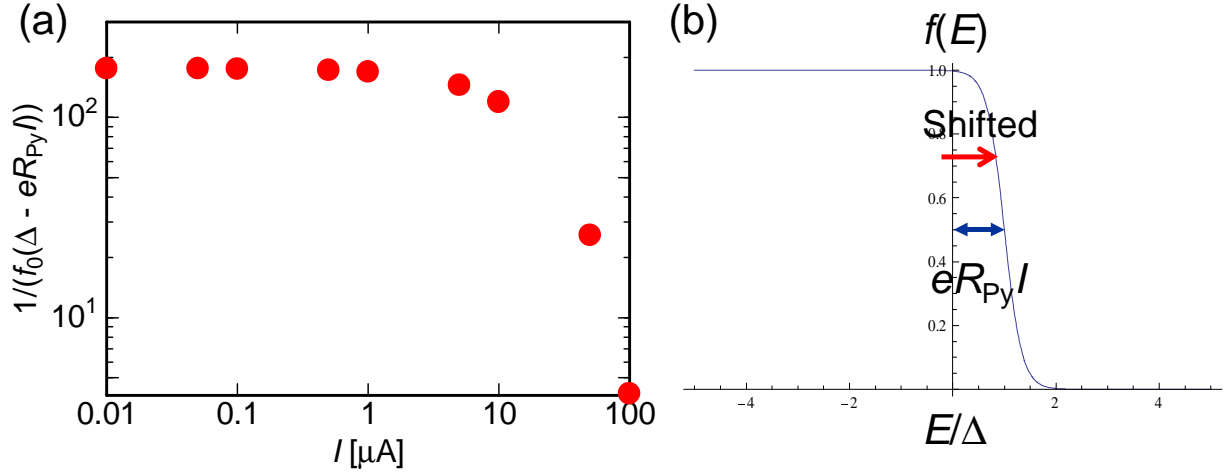


Figure 5.17: Numerically calculated values of $1/f_0(\Delta - eR_{\text{Py}}I)$ (a) and a schematic image of the shifted Fermi distribution function $f_0(E - eR_{\text{Py}}I)$. Satulated $1/f_0(\Delta - eR_{\text{Py}}I)$ in a small I region indicates saturation of $\Delta R_{\text{ISHE}}^{\text{super}}$ with smaller I .

condition does not severely effect the final results. We take $x = 0$ at the interface and $x > 0$ in the NbN wire. Δ_0 is the superconducting gap at $T = 0$, for NbN we can determine by using the relation

$$\Delta_0 = 2.2k_{\text{B}}T_{\text{C}} \quad (5.25)$$

from T_{C} because NbN is in the strong-coupling regime [97]. We account for the temperature dependence of the superconducting gap as [88]

$$\Delta(T) = \Delta_0 \left(1 - \frac{T}{T_{\text{C}}}\right)^{1/2}. \quad (5.26)$$

ξ is calculated using the relation

$$\xi = \sqrt{\frac{\hbar D}{\Delta_0}}, \quad (5.27)$$

where D is the diffusion constant of NbN. We note that ξ calculated by experimental data is $\xi \sim 4$ nm. Below, we define $\chi = I_{\text{s}}^{\text{super}}/I_{\text{s}}^{\text{normal}}$. Enhanced $\Delta R_{\text{ISHE}}^{\text{super}}$ can be originated from increasing $f_0(\Delta)^{-1}$ and $f_0(\Delta)^{-2}$ both included in the above equation [30]. On the other hand, χ is a decreasing function with decreasing T because of the superconducting gap of the NbN wire [30]. We first numerically calculate $\chi/f_0(\Delta)$ and $\chi/(f_0(\Delta))^2$ as a function of T . The results are shown in Fig. 5.14. In this calculation we use the spatially dependent Δ as in (5.24). We perform calculations for each x , and results are finally spatially averaged over x . Increasing behaviors of both $\chi/f_0(\Delta)$ and $\chi/(f_0(\Delta))^2$ are clearly found, and especially for $\chi/(f_0(\Delta))^2$ enhancement

is over thousands times as a function of T down to 3 K. Thus from (5.21), gigantic $\Delta R_{\text{ISHE}}^{\text{super}}/\Delta R_{\text{ISHE}}^{\text{normal}}$ can be explained by enormous increase in $\chi/(f_0(\Delta))^2$. We note that as discussed above, from Fig. 5.3 and Fig. 5.6 we can determine the two constants a and b and found that $a \ll b$. Henceforth we thus approximate (5.21) as

$$\frac{\Delta R_{\text{ISHE}}^{\text{super}}}{\Delta R_{\text{ISHE}}^{\text{normal}}} \sim \frac{\zeta^{\text{super}}}{\zeta^{\text{normal}}} \frac{I_s^{\text{super}}}{I_s^{\text{normal}}} \frac{1}{(2f_0(\Delta))^2}. \quad (5.28)$$

From above we can discuss the gigantic $\Delta R_{\text{ISHE}}^{\text{super}}$ as a function of decreasing T . Since in our experiments $\Delta R_{\text{ISHE}}^{\text{super}}$ increases with decreasing I , not with T , next we attempt to associate T with I . We can transform the equation (5.12) into the form

$$T = \sqrt{c_0 + \sqrt{c_1 + c_2 I^2}}, \quad (5.29)$$

where c_0, c_1 and c_2 are all constants. Let us first try to substitute this relation into (5.28). We show an example of the calculated results in Fig. 5.15. As seen in the figure, $\Delta R_{\text{ISHE}}^{\text{super}}$ saturates in the small I region and the experimental data of $\Delta R_{\text{ISHE}}^{\text{super}}$ increasing even with small I cannot be reproduced well.

To explain the anomalous enhancement of $\Delta R_{\text{ISHE}}^{\text{super}}$ attributing it to increase of T at the NbN/Cu interface, we assume that the relation between T and I be written as

$$T = T_0 + C\sqrt{I}, \quad (5.30)$$

as hinted by (5.29). In (5.30) C is a constant. By appropriately choosing C , we can reproduce the anomalous increasing of ΔR_{ISHE} with smaller I as shown in Fig. 5.16. However, the relation between I and T in (5.30) is based on the assumption, and to elucidate physical meanings more investigations are needed. We next take a different approach to explain the anomalous enhancement of $\Delta R_{\text{ISHE}}^{\text{super}}$. We assume that when electrons pass through the Py spin injector, they are excited and acquired extra energy ΔE through the spin injection current I expressed as

$$\Delta E = eR_{\text{Py}}I. \quad (5.31)$$

We assume that at low temperatures energy relaxation occurs slowly, and electrons keep ΔE till they reach the NbN/Cu interface. Due to this ΔE , the Fermi distribution function in the Cu and also in the NbN shifts and is written as

$$f_0(E) = \frac{1}{\exp\left(\frac{E - eR_{\text{Py}}I}{k_{\text{B}}T}\right) + 1}. \quad (5.32)$$

The shifted Fermi distribution function is schematically displayed in Fig. 5.17(a). We

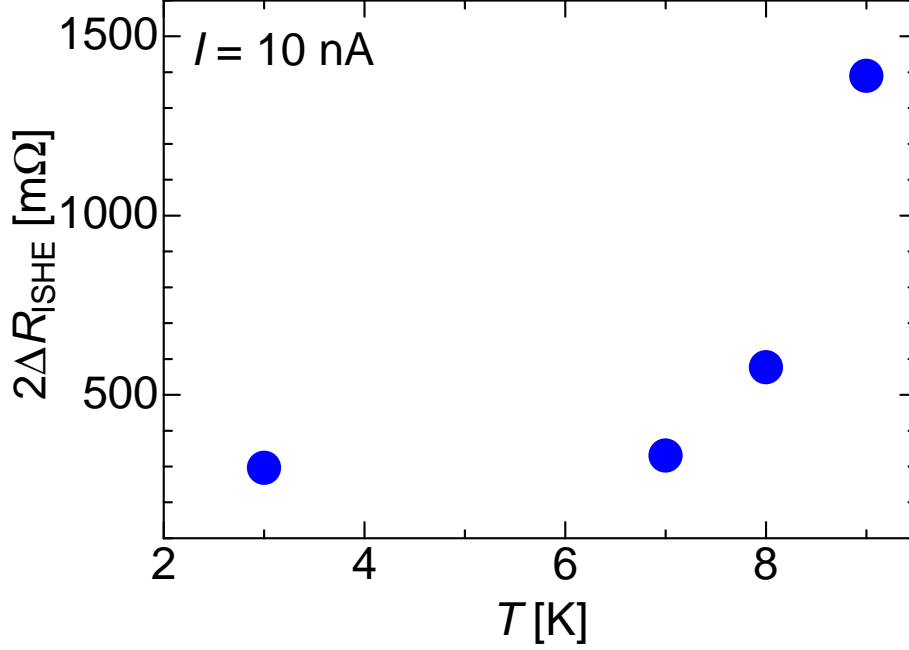


Figure 5.18: Temperature (T) dependence of ΔR_{ISHE} in the superconducting state. Spin injection current (I) is 10 nA. As T is close T_{C} , ΔR_{ISHE} is dramatically increasing.

use this shifted Fermi distribution function in (5.21). We calculate $1/f_0(\Delta)$, namely,

$$\frac{1}{f_0(\Delta)} = \exp\left(\frac{\Delta - eR_{\text{Py}}I}{k_{\text{B}}T}\right) + 1, \quad (5.33)$$

as a function of I . Results are shown in Fig. 5.17(b). $1/f_0(\Delta)$ is found out to saturate in a small I regime. This saturated $f_0(E)$ induces the saturation of $\Delta R_{\text{ISHE}}^{\text{super}}$, and we cannot reproduce experimental results using this model.

To confirm if the effective temperature increase at the NbN/Cu interface is the origin of the anomalously large $\Delta R_{\text{ISHE}}^{\text{super}}$, we carry out measurements of the temperature dependence of $\Delta R_{\text{ISHE}}^{\text{super}}$. As discussed in the introductory chapter, ΔR_{ISHE} is theoretically predicted to enhance with decreasing T due to increasing resistivity of superconducting quasiparticles [30]. In the theory [30], $\Delta R_{\text{ISHE}}^{\text{super}}$ is expected to enhance monotonically as T decreases. Our experimental results of the T dependence are shown in Fig. 5.18. When T is close to T_{C} , ΔR_{ISHE} dramatically increases, and almost diverges. This divergence should be relevant to the divergence of several parameters such as $\lambda_{\text{Q}}(T)$ close to T_{C} . It should be noted that the temperature dependence of $\lambda_{\text{Q}}(T)$ is proportional to $(1 - T/T_{\text{C}})^{-\frac{1}{4}}$ [101]. This temperature dependence is not taken into account in the theory [30]. The effect arising from the divergence of parameters such as $\lambda_{\text{Q}}(T)$ is also observed in the I dependence of ΔR_{ISHE} , where it first decreases with decreasing I for $100 \mu\text{A} < I < 300 \mu\text{A}$. This range of I is close to the transition from

the superconducting state into the normal state, which occurs for $350 \mu\text{A} < I < 400 \mu\text{A}$. The divergence of ΔR_{ISHE} is not taken into account the theory presented in [30]. We have also confirmed that these behaviors are independent of the spin injection current I .

The problem seen from Fig. 5.18 is the temperature dependence of ΔR_{ISHE} does not exactly correspond to that of I dependence. At the moment we attribute the enhancement of ΔR_{ISHE} to the effective temperature increase due to I , but by comparing the temperature dependence and I dependence of ΔR_{ISHE} , this is not necessarily true. As for the temperature dependence, we do not have sufficient data and cannot determine the complete behavior of ΔR_{ISHE} . Thus we leave the relation between the effective temperature and I for our future study.

5.4 Optimization of the NbN fabrication process

In this study we face several problems especially in the fabrication of NbN wires. In this section, we will explain the problems and how to solve them for future studies.

As shown above, the NbN superconducting wires are deposited onto substrates with the ZEP520A resist by the reactive DC sputtering. The main problem of the NbN wires fabricated in this way is that the resistivity of these wires is scattered dramatically. In measurements we have found that the resistivity of the NbN wires severely affects the SHE in the superconducting state.

We show a NbN layer deposited on top of the ZEP520A resist by sputtering in Fig. 5.19. The NbN layer has many cracks on the surface. In some cases remaining NbN wires for the SHE are also affected by the cracks. The NbN wire seems to roll up. These cracks may be due to the surface tension for the NbN from the ZEP520A resist. We next discuss resistivity (ρ_{xx}) of the NbN wires deposited by sputtering. ρ_{xx} strongly depends on devices, and as an example, we show ρ_{xx} of the NbN wires at room temperature (RT) in Table 5.1. For some wires we also show their ρ_{xx} at 20 K and T_C . ρ_{xx} is highly different from samples to samples, and the largest ρ_{xx} is more than twice larger than the smallest one. We can also find that the value of ρ_{xx} does not strongly affect T_C .

We have found that the value of ρ_{xx} strongly affects the SHE. Samples whose NbN wire has $\rho_{xx} > 300 \mu\Omega\text{cm}$ do not show clear inverse spin Hall signals even above T_C , and R_{I} is much larger than that for samples which show clear inverse spin Hall signals. For some samples, $R_{\text{I}} > 30 \Omega$ above T_C . These samples do not show dramatic enhancement of $\Delta R_{\text{ISHE}}^{\text{super}}$ below T_C . According to the measurements we have carried out so far, samples with $200 \mu\Omega\text{cm} < \rho_{xx} < 250 \mu\Omega\text{cm}$ only show the gigantic enhancement of $\Delta R_{\text{ISHE}}^{\text{super}}$ below T_C . ρ_{xx} is scattered even for samples on the same batch, and one has

Sample	ρ_{xx} ($\mu\Omega\text{cm}$, at RT)	ρ_{xx} ($\mu\Omega\text{cm}$, at 20 K)	T_C [K]
A	200	225	10
B	450	-	-
C	220	240	10
D	270	-	-
E	300	345	9.5
F	310	360	10
G	345	-	-

Table 5.1: Table of resistivity of NbN (ρ_{xx}) at RT obtained from seven different samples (A ~ G). ρ_{xx} at 20 K and T_C are also shown for some samples. Scattered values of ρ_{xx} are apparent.

to find samples which fulfill the condition of $200 \mu\Omega\text{cm} < \rho_{xx} < 250 \mu\Omega\text{cm}$.

To avoid inhomogeneity in ρ_{xx} , we attempted to fabricate NbN wires in a different way. In sputtering, the resist on a substrate may contaminate NbN wires so that ρ_{xx} increases. Thus we first deposit a NbN layer onto a substrate without the resist, and then perform the EB lithography with the ma-N2405 negative resist. After the lithography we carry out milling to remove the parts of NbN other than the wire necessary for the device. Subsequently the Py and Cu wire are fabricated in the same way as shown in the previous sections. We show in Fig. 5.20 a milling-based NbN wire whose width and thickness are 300 nm and 20 nm, respectively. To avoid shunting by residual NaN layer on the substrate, we have etched the surface of the substrate by about 30 nm, thicker than the thickness of the NbN layer. Thickness of the NbN wire

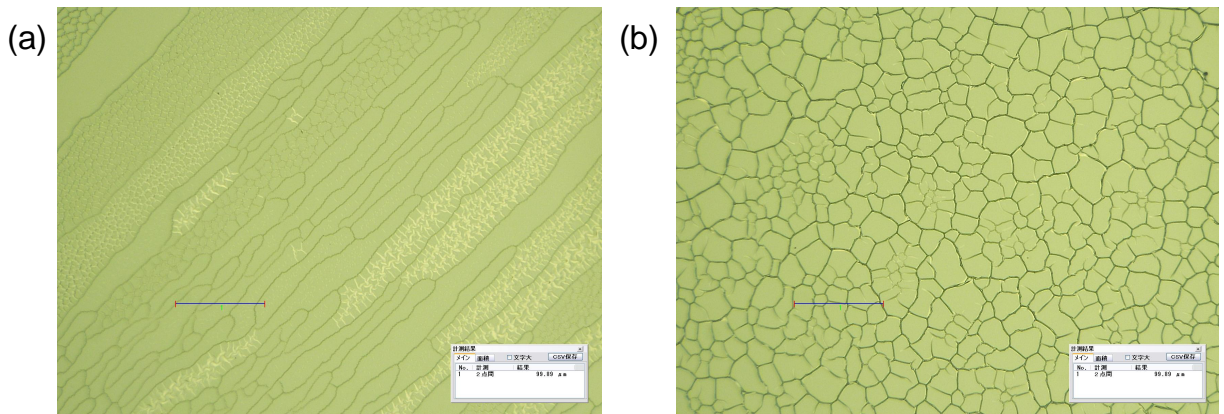


Figure 5.19: Two examples of cracks in the NbN layer sputtered onto the ZEP520A resist. The size of cracks are different in (a) and (b). The scale bar is $1 \mu\text{m}$. [105]

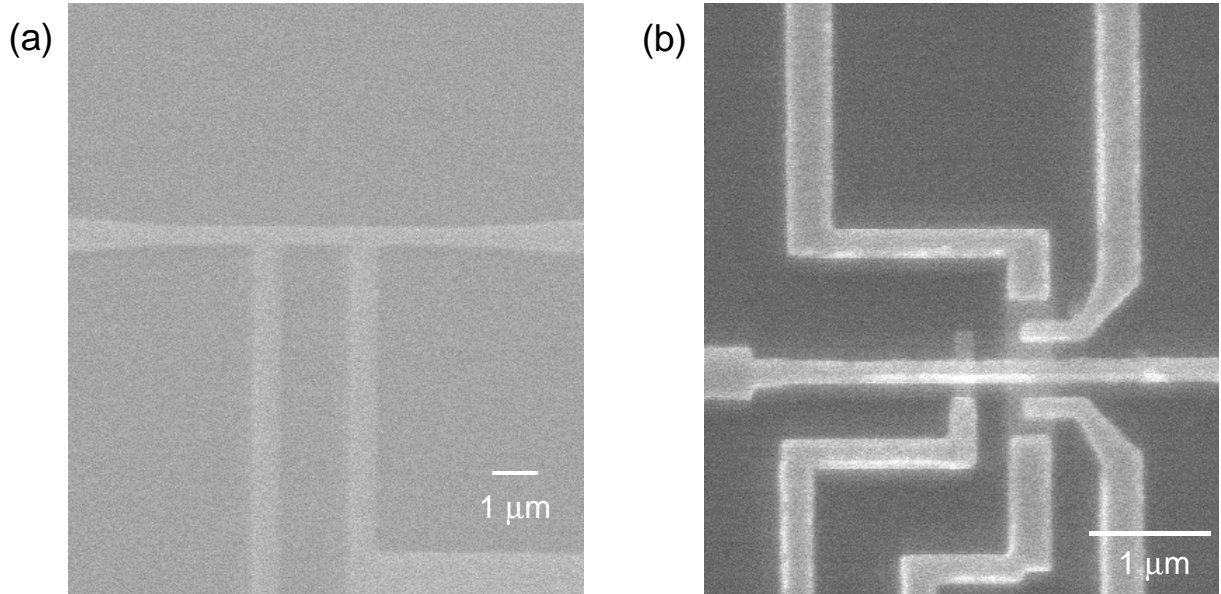


Figure 5.20: SEM images of the milling-based NbN wire for test sample (a) and one installed in the device to measure the SHE (b).

is checked by the surface profiler. Table 5.2 shows ρ_{xx} of the milling-based NbN wires with the structure as in Fig. 5.20. Scattering in ρ_{xx} is even smaller than that for NbN wires using the ZEP520A positive resist. We can also find out that ρ_{xx} is even smaller. Considering that NbN layers are sputtered in the same condition for two methods, this means that ZEP-based wires are contaminated by the resist, and milling-based NbN wires have less contaminations. We can therefore attribute inhomogeneity in ρ_{xx} for the ZEP-based wires to contamination by resists. From these results, to obtain NbN wires with uniform ρ_{xx} we should fabricate the wires using sputtering and Ar-ion milling rather than sputtering on the resist.

Sample	ρ_{xx} ($\mu\Omega\text{cm}$, at 20 K)
1	148
2	176
3	132
4	148
5	140

Table 5.2: Resistivity ρ_{xx} for the five samples of the milling-based NbN wires. Scattering in ρ_{xx} is much smaller than that for the ZEP-based samples.

5.5 Direct spin Hall effect

We finally show our results of the direct spin Hall effect (DSHE) measurements. As we have explained so far, spin transport in superconductors is mediated by the Bogoliubov quasiparticles. In superconductors, electrons form Cooper pairs and these Cooper pairs can carry currents without dissipation (supercurrents). In typical superconductors, however, Cooper pairs are in the spin-singlet state and they cannot carry spin angular momentum. Thus to induce spin currents through the SHE in superconductors, one has to generate a flow of quasiparticles currents. When currents flowing in a superconductor is below the critical current I_c of the superconductor, most of the currents are carried by Cooper pairs because it is energetically favorable. In our device, I_c of the superconducting NbN wires is $I_c \sim 20 \mu\text{A}$. Above I_c , superconductivity is destroyed. Fig. 5.21 show the results of our measurements of the DSHE by passing currents through the NbN wire and measure the voltage between the Py spin injector and the Cu bridge. We have changed the measurement temperature and the current we pass through the NbN wire. The currents are below I_c so as not to break superconductivity of the NbN wire. As seen in Fig. 5.21, we do not obtain clear signals for both conditions. This might be because currents we flow is too small to detect signals because we do not obtain the signals even at 8 K close to T_C . Therefore to observe the DSHE clearly, we have to inject electrons externally to the states of the NbN above the superconducting gap through the tunneling barrier between the probe and the superconducting NbN wire. At the time of writing this thesis we do not perform these experiments yet, but to detect the DSHE and investigate if the Onsager's reciprocity holds for the DSHE and ISHE is of great interest. We leave these measurements for our future study.

5.6 Brief summary

In this Chapter we have reported the first observation of the inverse spin Hall effect in a superconducting NbN. Even in the superconducting state, we observe clear inverse spin Hall signals (ΔR_{ISHE}) and surprisingly, as the spin injection current (I) decreases ΔR_{ISHE} dramatically increases. With $I = 0.01 \mu\text{A}$, ΔR_{ISHE} becomes more than 2000 times larger than that in the normal state. This enhancement with decreasing I can be explained by the net increase of the effective temperature at the NbN/Cu interface, but the fitting based on this idea does not reproduce experimental data well in the whole I range. While data on the T dependence of ΔR_{ISHE} is not sufficient, at present correspondance between the I dependence and T dependence of ΔR_{ISHE} is not good. These discrepancies may suggest the possibility of other effects such as nonequilibrium

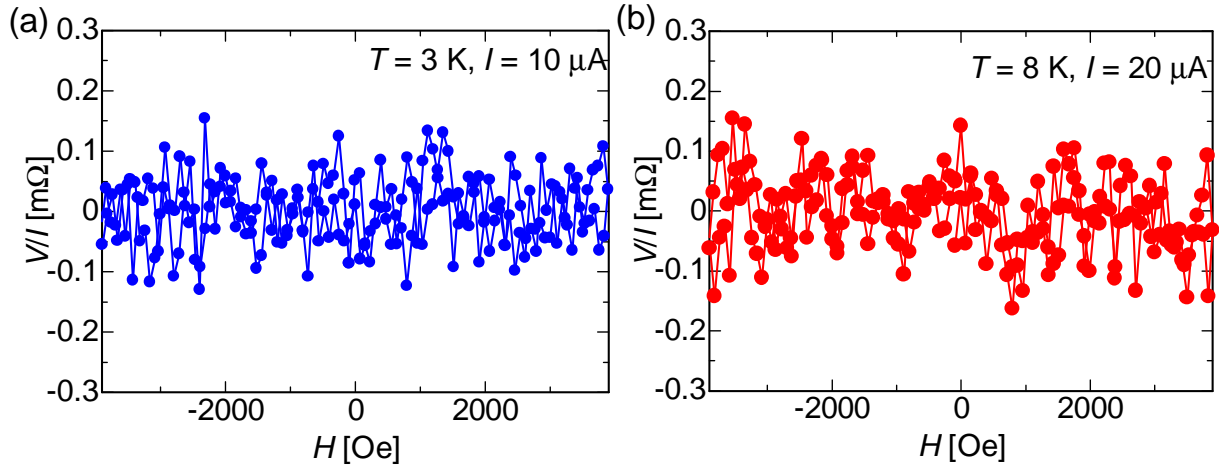


Figure 5.21: DSHE measured at different temperatures with different currents. (a): DSHE at 3 K with 10 μA current through the NbN wire. (b): DSHE at 8 K with 20 μA bias current. No clear signals are observed for both conditions.

effects play a role for this gigantic enhancement of ΔR_{ISHE} . It is difficult to take into account these nonequilibrium effects in calculations. To elucidate the effect of the spin injection current, however, more data of the T dependence of the ISHE are necessary.

In the current status, inhomogeneities in the NbN quality are the biggest problem. Argon-ion milling is one solution, and as another solution, now we are trying to use the reactive ion etching for making NbN wires from a NbN thin film. This technique may enable us to fabricate NbN wires faster and with better quality. We also have to optimize the condition of cleaning the surface of the NbN wire before depositing Cu, which is an important factor to observe the ISHE in superconductors.

The SHE in other superconductors is also intriguing. First candidates are niobium and lead. Observation of the enhancement of the SHE in these superconductors other than NbN is also our important future work.

Chapter 6

Application of odd-frequency spin-triplet supercurrent to spintronics

6.1 Motivation

As discussed in the previous chapters, in most superconductors Cooper pairs are in the spin-singlet state, therefore do not carry any spin angular momenta. However, spin-triplet Cooper pairs are possible taking into account for the Pauli's exclusion principle. Exploitation of spin-triplet supercurrents for spintronics is highly attractive in condensed matter physics, and also important for application because spin-polarized

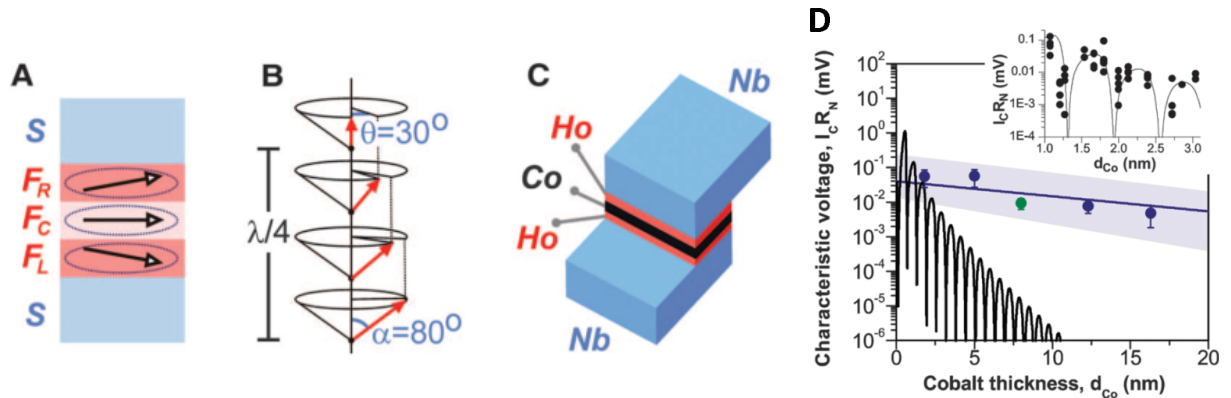


Figure 6.1: Experimental results done by Robinson *et al.* [109] with Nb/Ho/Co/Ho/Nb multilayers Josephson junctions. A: noncolinear magnetization among the Co layer and two Ho layers play an important role for spin-singlet/spin-triplet conversion. B: In Ho localized moments are cant by $\alpha = 80^\circ$ to the axis, and between neighboring sites magnetic moment rotates by 30° . C: Schematic of the device. A Co ferromagnetic layer is sandwiched between Ho layers with Nb superconductors. D: Characteristic voltage $I_c R_N$ as a function of the thickness of the Co layer. I_c represents the critical current of the Josephson junction and R_N the resistance of the junction in the normal state.

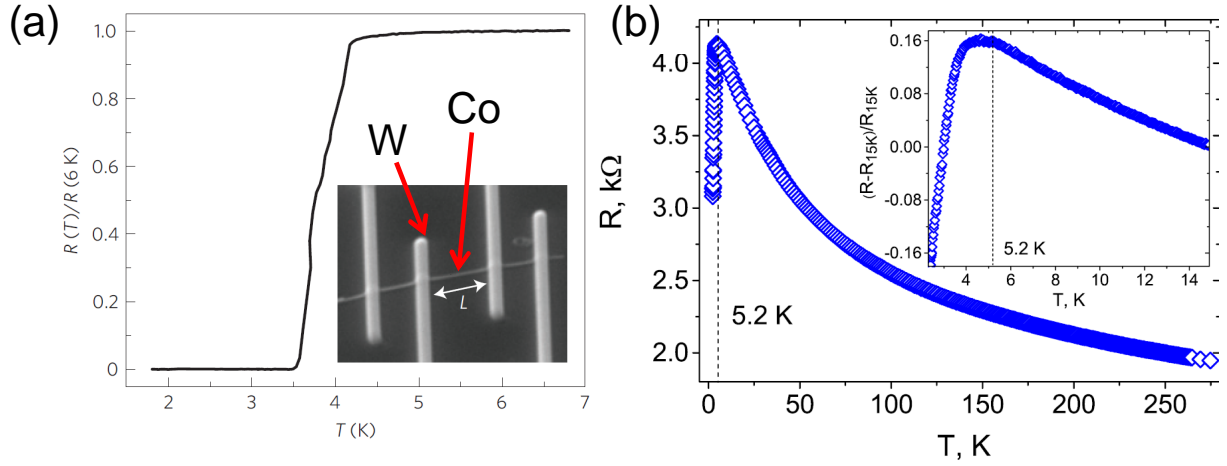


Figure 6.2: Examples of experimental studies on spin-triplet superconductivity using lateral devices. In both (a) and (b) tungsten (W) wires are deposited on the Co wire by using the FIB system.

supercurrents can carry spin currents truly without dissipation.

There are a few examples of spin-triplet pairing. The most prominent example is an oxide, Sr_2RuO_4 [106], which has the p -wave symmetry in the momentum space. There have been many theoretical proposals on using Sr_2RuO_4 for spintronics [107, 93]. However, from the view of experimentalists, this material is difficult to fabricate with sufficiently high quality. High quality is necessary because due to the Anderson's theorem [108], superconductors with the p -wave symmetry are very weak to disorders. It is also difficult to carry out nanofabrication with this material using the Focused-Ion-Beam (FIB) system or Ar-ion etching because these processes can cause a doping of Ga or Ar ions into Sr_2RuO_4 , where act as impurities. Other spin-triplet superconductors such as UPt_3 or other heavy-fermion systems, are not easily accessible. In this regard, spin-triplet superconductors with the s -wave symmetry are robust against disorders and much easier to obtain. Whereas the first report in CrO_2 ferromagnetic Josephson junction does not show good reproducibility, controlled experiments demonstrated by Robinson *et al.* in 2010 [119] inserting a conical magnet Ho in between a superconductor and a strong ferromagnet shows the importance of the inhomogeneous magnetization between a superconductor and a strong ferromagnet, and many experimental studies have been reported following this study (Fig. 6.1). In the same year, the group in the Michigan State University led by N. O. Birge also reported that in $\text{Nb}/\text{CuNi}(\text{or PdNi})/\text{Co}/\text{CuNi}(\text{or PdNi})/\text{Nb}$ Josephson junctions, supercurrents can be observed even for Co ferromagnets whose thickness is much larger than the coherence length for ferromagnets ξ_F [110, 111]. ξ_F for the spin-singlet Cooper pairs can be

written in a diffusive regime as

$$\xi_F = \sqrt{\frac{\hbar D}{E_{\text{ex}}}}, \quad (6.1)$$

where D is a diffusion constant and E_{ex} is an exchange energy. Typical length scale of ξ_F for strong ferromagnets like Ni, Fe and Co is several nm, but in the work [110, 111] they have observed supercurrents even for $t_{\text{Co}} \gg \xi_F$ and concluded that the long-living supercurrents are due to spin-triplet Cooper pairs converted from the spin-singlet Cooper pairs through the CuNi or PdNi layers.

Previous studies we have presented above are all done using multilayer structures, where each layer is grown perpendicularly to the substrate. Experiments using lateral devices have also been reported by several groups. Wang *et al.* [112] demonstrated that Co nanowires show zero resistance on top of which tungsten (W) wires are deposited by using the Focused-Ion-Beam (FIB) system (Fig. 6.2(a)). Moreover, supercurrents are conserved in more than 600 nm, much larger than ξ_F . This length is comparable to the one in Keizer *et al.*, which is estimated to be $\sim 1 \mu\text{m}$ [66]. W is a metal which shows a superconducting transition, and W deposited by FIB systems is known to have much higher critical temperature (T_C) than that of the bulk W. Sadki *et al.* reported $T_C \sim 5 \text{ K}$ [113], while T_C of bulk tungsten is as low as 12 mK [114]. One explanation for this large enhancement in T_C is proposed in [115]. According to the BCS theory, T_C of a superconductor is associated with the density of states (DOS) at the Fermi energy $N(0)$ and electron-electron interaction V through the equation as

$$T_C \propto \exp\left(-\frac{1}{N(0)V}\right). \quad (6.2)$$

W deposited by the FIB systems is amorphous [113]. Because of this amorphous state, carrier density decreases. In conductors, electron-electron interaction is screened by other electrons. Thus reducing carrier density induces reducing screening and increasing V . If we assume $N(0)$ is constant, increasing V causes an enhancement of T_C using the relation in (6.2).

The most different point in the study by Wang *et al.* than that of previous studies is that no interlayer is inserted between a superconductor (S) and a ferromagnet (F). One explanation for this result is that due to the strong spin-orbit interaction (SOI) of W [24], spin active interface is induced between Co and W [116], which induces inhomogeneous magnetization. Recently, similar results have been reported [117] using the same system with Co nanowires and FIB-deposited W superconductors. These lateral devices are more appropriate to study spin transport by the spin-triplet supercurrents in a long range, and also easy to be integrated into the lateral spin valves.

We have briefly reviewed mainly experimental studies on the odd-frequency spin-

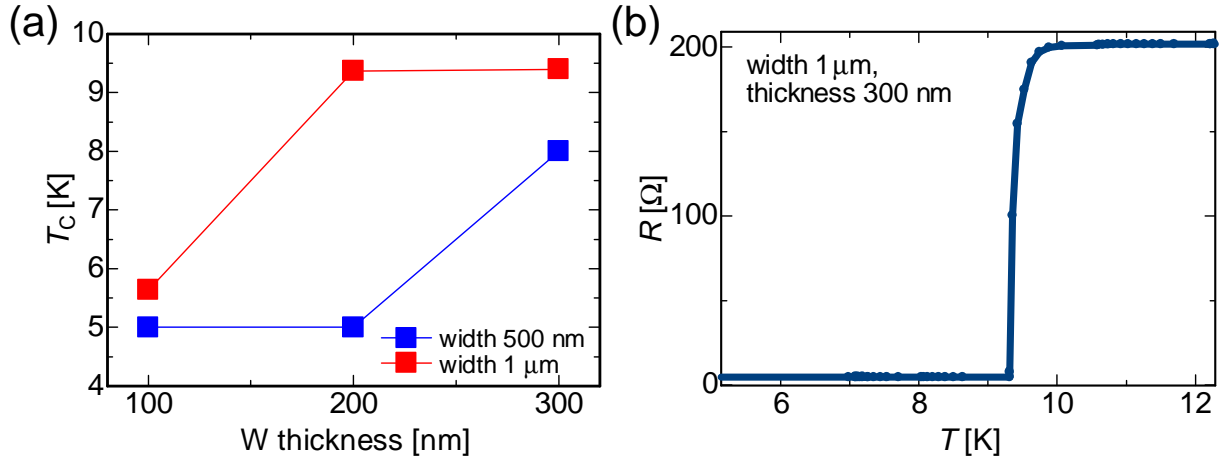


Figure 6.3: Experimental results of superconductivity in W wires. (a) Thickness (t_W) and width (w_W) dependence of T_C . With increasing t_W and w_W , T_C enhances. (b): Temperature (T) dependence of the resistance (R) of the W wire with $t_W = 300$ nm and $w_W = 1 \mu\text{m}$. $T_C \sim 9.5$ K.

triplet supercurrents in ferromagnetic Josephson junctions. This field is not mature yet, and has potential to study. We now discuss several points which are not clarified or investigated in the previous studies.

(A) Why is ferromagnet Co is often used?

In the previous studies they often used Co as a ferromagnet. Co is different from other ferromagnets like Ni or Fe in terms of the magnetic anisotropy [118]. Fe and Ni have the cubic anisotropy and Co has the uniaxial anisotropy. However, the magnetic anisotropy does not seem an important factor to observe the spin-triplet supercurrents in SFS Josephson junctions. There exist no studies which discuss relation between the magnetic anisotropy and generation of the spin-triplet supercurrents. If the magnetic anisotropy has nothing to do with spin-singlet/spin-triplet conversion, the spin-triplet supercurrents can be observed using other ferromagnets like Ni, Fe and Py. There is one study on the spin-triplet supercurrents using the Fe/Cr multilayers [119], but the device geometry is different than that of the previous study [109]. Exploring potentialities of other strong ferromagnets for generating the spin-triplet supercurrents is important to apply it to spintronics.

(B) Are supercurrents really spin-triplet and spin-polarized?

Arguments about the spin-triplet supercurrents are supported by the fact that the supercurrents decay in a much longer length than ξ_F , as expected from the scenario based on the spin-singlet Cooper pairs. However, direct observation is not reported yet

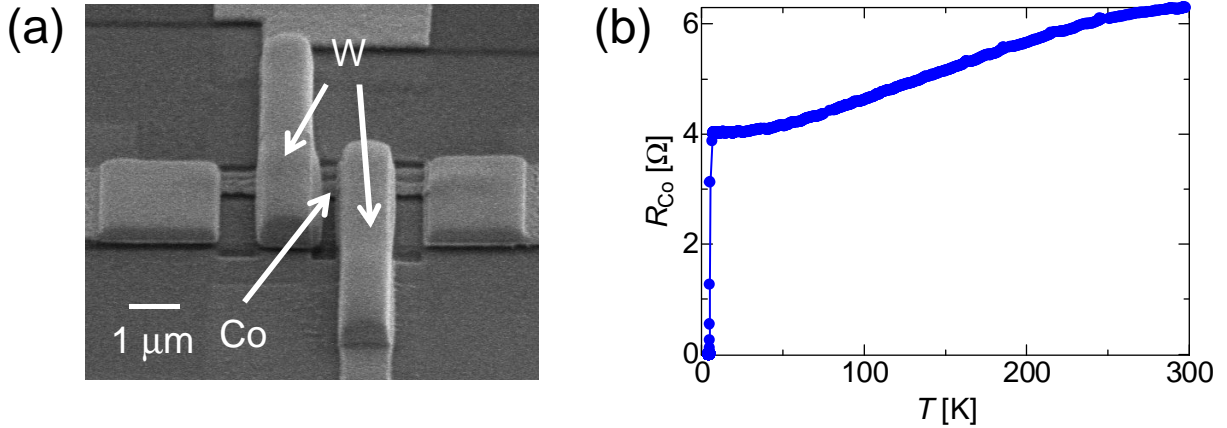


Figure 6.4: (a) SEM image of the W-Co-W Josephson junction. W is deposited by the FIB system and distance between the two W wires is ~ 400 nm. (b) T dependence of R of the W-Co-W junction shown in (a). A sharp drop in R is observed at $T \sim 7$ K, a signature of superconductivity induced in Co.

of the spin polarization of the long-range supercurrents in SFS junctions. To attain this, techniques which are often utilized in spintronics are useful [67]. For example, spin-transfer-torque (STT) by the spin-triplet supercurrents are proposed [68], and relation between the supercurrents and domain wall motions is also discussed [69]. When there are domain walls in a F part of a SFS Josephson junction, spin-triplet supercurrents can push the domain walls through STT. Then, for example, magnetoresistance of the F part above T_C should be different before and after the spin-triplet supercurrents pass through the F part. How domain wall motion affects superconductivity induced in F is also interesting.

Motivated by these points, we perform experiments and below we show some of our results we currently obtain.

6.2 Experimental results

We first attempted to fabricate SFS Josephson junctions with cobalt (Co) as a ferromagnet and tungsten (W) as a superconductor as done in the previous studies. Co wires are deposited by the EB evaporation onto thermally surface oxidized Si substrates with Au pads for electrodes. The Co nanowires is 100 nm in thickness and 500 nm in width. Then substrates are transferred into the HITACHI NB-5000 Focused-Ion-Beam (FIB) system. Using the deposition mode, W wires are written on the Co wires. Acceleration voltage of the Ga-ions beam is 40 kV and the aperture for beam current is $30 \mu\text{m}$. Thickness (t_W) and width (w_W) of W wires are controlled to obtain higher T_C . We show t_W and w_W dependence of T_C . For these samples we deposited only W

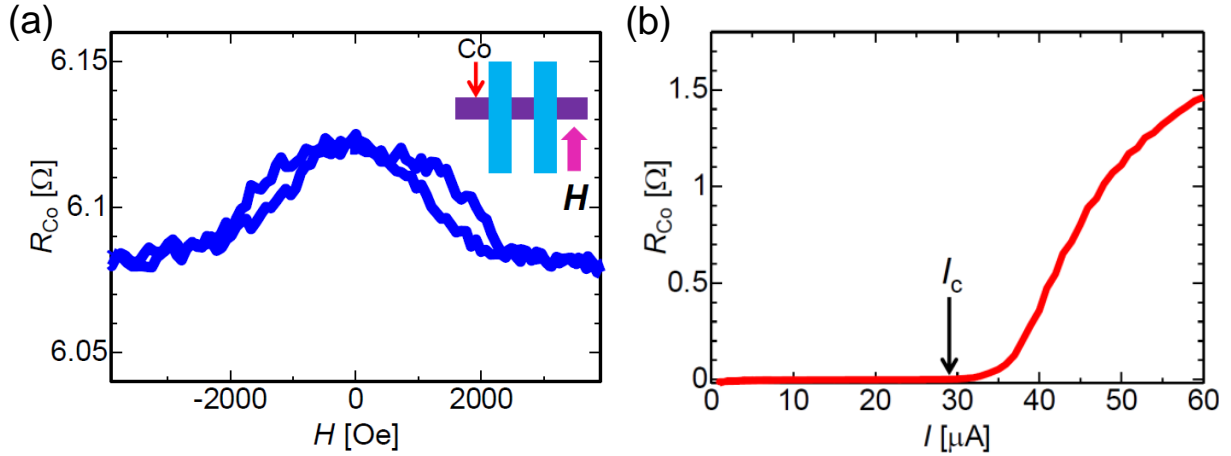


Figure 6.5: (a): AMR signal of the Co wire obtained at room temperature. (b): Resistance of the Co (R_{Co}) wire as a function of a current (I).

wires through the deposition mode of the FIB system. As shown in Fig. 6.3(a), T_C increases with increasing t_W and also w_W . In Fig. 6.3(b), we also show an example of temperature (T) dependence of resistance (R) for a sample with $t_W = 300$ nm and $w_W = 1$ μm . A sharp drop in R is observed at $T \sim 9.5$ K. This value is much higher than those previously reported [113]. To obtain higher T_C below we fix t_W and w_W as 300 nm and 1 μm , respectively.

We next fabricate ferromagnetic Josephson junctions with Co as a ferromagnet, as used in many previous studies. We found, however, that W deposition by the FIB system always accompanies a spread of W precursor ($\text{W}(\text{Co})_6$) surrounding the main W wire, which can cause a shunting effect between neighboring W wires. Thus when we flow a current through W-Co-W Josephson junctions, below T_C supercurrents pass not through the Co wire but through the W layer because it has lower resistance, which connects the two W wires directly. To avoid this shunting effect, we attempted to carry out Ga sputtering of the surface of the substrates to remove the extra W layers due to spread of the W precursor. The SEM image of a device fabricated in these procedures is displayed in Fig. 6.4(a). We note that a W layer on a Co wire is also removed by Ga sputtering to suppress the shunting effect completely. Using these devices, we measured temperature dependence of resistance of the junction. Figure 6.4(b) shows an experimental result. At $T \sim 7$ K, resistance R drops to zero, a signature of superconductivity induced in the Co wire.

In using the FIB systems, Ga ions are inevitably doped into materials like W or Co in this study. Due to this doping, Co wires might lose ferromagnetism. To confirm if ferromagnetism of Co wires is sustained, we measured anisotropic magnetoresistance (AMR) of the Co wire at room temperature. As shown in Fig. 6.5, the AMR originated

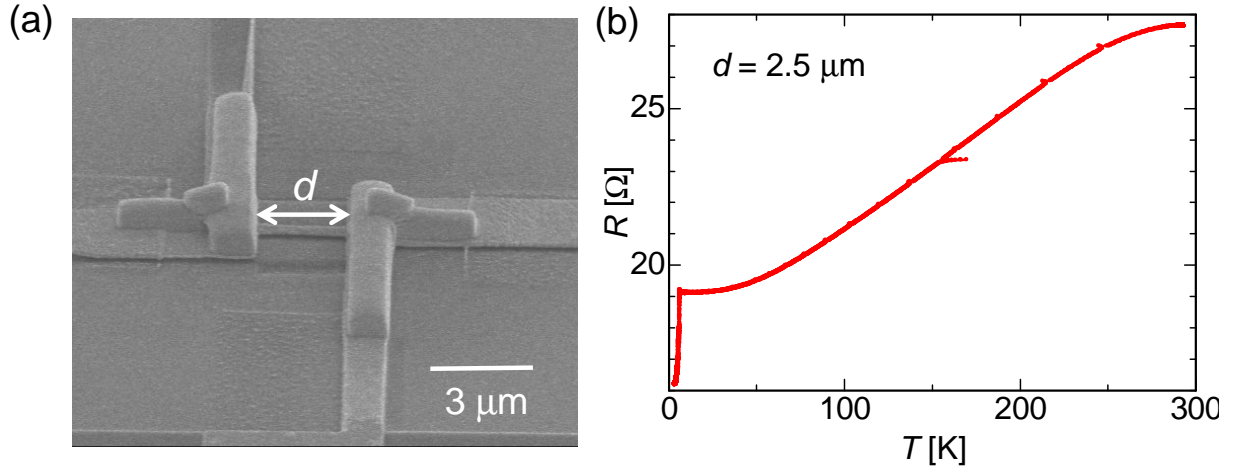


Figure 6.6: (a): SEM image of the SFS Josephson junction with the distance between two W wires of $2.5 \mu\text{m}$. (b): Temperature dependence of the resistance of the Co wire in the junction. The resistance does not drop to zero down to 4 K.

from ferromagnetism of the Co wire is clearly observed. Thus supercurrents shown in Fig. 6.4(b) flow ferromagnetic Co, not nonmagnetic Co, which provides a signature of the spin-triplet supercurrents.

6.3 Problems and future studies

In the previous section we have demonstrated supercurrents flowing in a ferromagnetic Co wire, which might be a signature of the spin-triplet Cooper pairs. However, spurious effects might play a role in this supercurrent measurement. For example, we carry out etching of extra W layer by Ga-ions beam, but direct writing of Ga wire by the FIB system is reported to show superconductivity [120]. Thus one might say observed superconductivity in our system derives from superconductivity of Ga, because Ga ions should be injected into the Co wire. However, we can exclude this possibility. Figure 6.6 shows the SEM image and temperature dependence of the resistance of a Co wire. In this device the distance between the two W wires (d) is $2.5 \mu\text{m}$, much longer than that shown in Fig. 6.4. The Co wire in this device does not show a resistance drop to zero at least down to 4 K, contrary to the previous device. This can be explained by the scenario based on spin-triplet supercurrents because d should be longer than the coherence length of the Co wire, which can be expressed as the form for the coherence length of normal metal:

$$\xi_{\text{F}}^{\text{triplet}} = \sqrt{\frac{\hbar D}{k_{\text{B}} T}}, \quad (6.3)$$

an order of a few hundreds nm in 4 K. In the Ga-doping scenario, this residual resistance of the Co wire cannot be explained, because regardless of d , doped Ga ions in the Co wire should show superconductivity, thus resistance should drop to zero.

However, to perform more controlled experiments, we are now planning to change our device fabrication method. Since the Ga-ion etching following W wires writing inevitably causes doping of Ga ions. Since Ga ions act as disorders, resistivity of the Co wires increase, and the coherence length of the Co wires decreases. Doped Ga ions might bring bad effects also on ferromagnetism of the Co wire. To avoid Ga etching, we have to suppress the spread-out of W layers. In our present fabrication conditions, the acceleration voltage (V_{acc}) and the beam current (I_{Ga}) is larger than other studies [113, 121, 122]. For example, in the work [121], they used $V_{\text{acc}}= 30$ kV and $I_{\text{Ga}}= 1$ pA, smaller than that in our study. Large V_{acc} and I_{Ga} means that a number of Ga ions with high energy sputter $\text{W}(\text{Co})_6$ onto the surface of the substrate. This causes splashing W precursor, thus extra W layers are deposited. In future studies, we will attempt to optimize the condition of V_{acc} and I_{Ga} to minimize these effects.

Chapter 7

Conclusions and future perspective

7.1 Conclusions on spin transport in superconductors

In the final chapter we briefly summarize our results and make a conclusion of our study on spin transport in superconductors.

7.1.1 Spin injection into a superconductor with strong spin-orbit coupling

As we have shown in Chapter 4, we have successfully demonstrated the enhanced spin relaxation time (τ_{sf}) in a superconducting Nb. In the previous experimental studies estimation of τ_{sf} is not consistent with each other, and some reports have shown the suppressed τ_{sf} . One paper by Yang *et al.* have shown that million-times enhancement of τ_{sf} in a superconducting Al [70]. This value, however, is much larger than that theoretically predicted [28]. This might be because in [70], strongly spin-polarized electrons are forcibly injected into a superconductor, which may cause a strong reduction of the superconducting gap than expected. We exclude these spurious effects in the previous studies which cause underestimations or overestimations of τ_{sf} . Our study is the first report to estimate τ_{sf} using the Usadel equation, and the conclusion of longer τ_{sf} in the superconducting state is also of technological interest. As we have mentioned, however, in this study we use a Nb superconductor to use the spin absorption technique and also for future studies on the spin Hall effect. When we consider only the magnitude of τ_{sf} , our obtained values are much shorter than that of graphene [10, 123, 124], for example. Among superconductors, Al has much longer τ_{sf} owing to the small SOI. Therefore to exploit enhanced τ_{sf} in the superconducting state, it might be more attractive to use these materials. Graphene does not show superconductivity itself, but it is possible to induce superconductivity via the superconducting proximity effect [82, 125]. It is of great interest to demonstrate enhanced τ_{sf} in graphene with super-

conducting proximity effect and attain longer τ_{sf} than that of graphene in the normal state. As a related topic, it is theoretically proposed that the $0-\pi$ transition is possible in a superconductor/normal-metal/superconductor Josephson junctions induced by the spin accumulation in the normal metal region [126]. On the other hand, pure spin current generation by using superconductor/graphene/superconductor Josephson junctions is also theoretically predicted [127]. These topics are also attractive for future work.

7.1.2 Quasiparticle-mediated spin Hall effect in a superconductor

In Chapter 5 we have reported the enormous enhancement of the inverse spin Hall effect (ISHE) in a superconducting NbN. An efficient spin-charge conversion via the SHE and its inverse is an important subject in spintronics, thus the enormous enhancement of the SHE in a superconductor demonstrates the great potential of superconductors for an ideal spin-charge converter.

As a matter of fact, our study on the SHE in a superconducting NbN has not been completed at all and we still have a lot of things to do. At the time of writing this thesis, the author is struggling to establish the method to fabricate NbN nanowires with homogeneous qualities to measure the temperature dependence of the inverse spin Hall signal below T_C . As discussed in the last part of Chapter 5, fabrication of NbN wires by sputtering a NbN layer on top of the ZEP resist causes an inhomogeneity of the quality of the NbN wires, which is problematic to measure the enhancement of the ISHE in the superconducting state. To avoid this, we have changed the fabrication process to use the Ar-ion milling in combined with the negative resist.

Relation between the spin injection current and the effective temperature at the NbN/Cu interface has not been completely clarified. We now attribute the enhancement to an effective temperature increase only, but it is difficult to explain all of the results we obtain from the measurements based on this scenario. For future work, we will include other effects including nonequilibrium effects relevant to superconductivity, and also construct elaborate model for estimating the temperature of electrons, phonons and the substrate separately, accounting for the Wiedemann-Franz law for the heat flow. As a first step toward this goal, more data on the temperature dependence of the inverse spin Hall signals are necessary. Direct spin Hall effect (DSHE) in a superconducting NbN is also intriguing, and indispensable when one considers future technological applications. As we have shown in Chapter 6, when one flow charge currents in a superconductor most of the currents are carried by Cooper pairs and quasiparticles currents are rather small because total currents have to be less than the

critical current of the superconductor. To detect the DSHE, hence one has to inject electrons above the superconducting gap. To do this, making a tunneling junction between a superconductor and a normal metal probe is necessary. This is also one of our future studies. It is also interesting to investigate if the Onsager's reciprocity is conserved between the DSHE and the ISHE in the superconducting state. This can also be our future work.

7.2 Future perspectives

In the final section of this thesis, we describe several interesting topics worthy of investigating, mainly focusing on those relevant to superconductors and spintronics.

7.2.1 Spin transport in high T_C superconductors

The ultimate goal of exploring new superconducting materials is to find room-temperature superconductors. If one can realize superconductivity at room temperature, energy dissipation will be dramatically suppressed and energy consumption will be highly reduced. At present room-temperature superconductors have not been discovered yet, superconductivity is even now achievable at much higher temperature than the liquid nitrogen temperature 77 K. These superconductors are called "high- T_C superconductors (HTS)". First HTS, LBCO (La-Ba-Cu-O) was discovered in 1986 by Bednorz and Müller [128], whose T_C is 35 K. Before the discovery of the LBCO, the highest T_C superconductor was NbGe₃, whose $T_C = 23$ K [129]. After this discovery, many HTSs have been reported, whose T_C exceed the BCS limit of $T_C \sim 40$ K and also the liquid nitrogen temperature 77 K. Some representative examples are YBCO (YBa₂Cu₃O_{7- δ} , $T_C = 93$ K) [130] and BSCCO (Bi₂Sr₂Ca₂Cu₃O_{10- δ} , $T_C = 110$ K) [131]. HTSs investigated for two decades after the first discovery by Bednorz and Müller are called "cuprate superconductors", because these superconductors consist of stacking layers of CuO₂. On the other hand, a new type of high- T_C superconductor was discovered in 2008. It is "iron-based layered superconductor" first reported by Kamihara *et al.* [132] for La[O_{1-x}F_x]FeAs ($x = 0.05-0.12$). Emergence of superconductivity in iron-based compounds is surprising because iron is a typical element for magnetism. Extensive research on iron-based superconductors is now being carried out [133].

The research subject that I am most interested in is to integrate such HTSs into spintronics. This is of great importance for engineering, and also highly attractive in condensed matter physics. The first relatively easier thing to do is to detect the SHE in HTSs. It is generally agreed that the symmetry of the energy gap of HTSs is d -wave, thus gigantic SHE as we observe in a typical s -wave superconductor should exhibit complex behaviors. It is also technologically promising if we can observe the

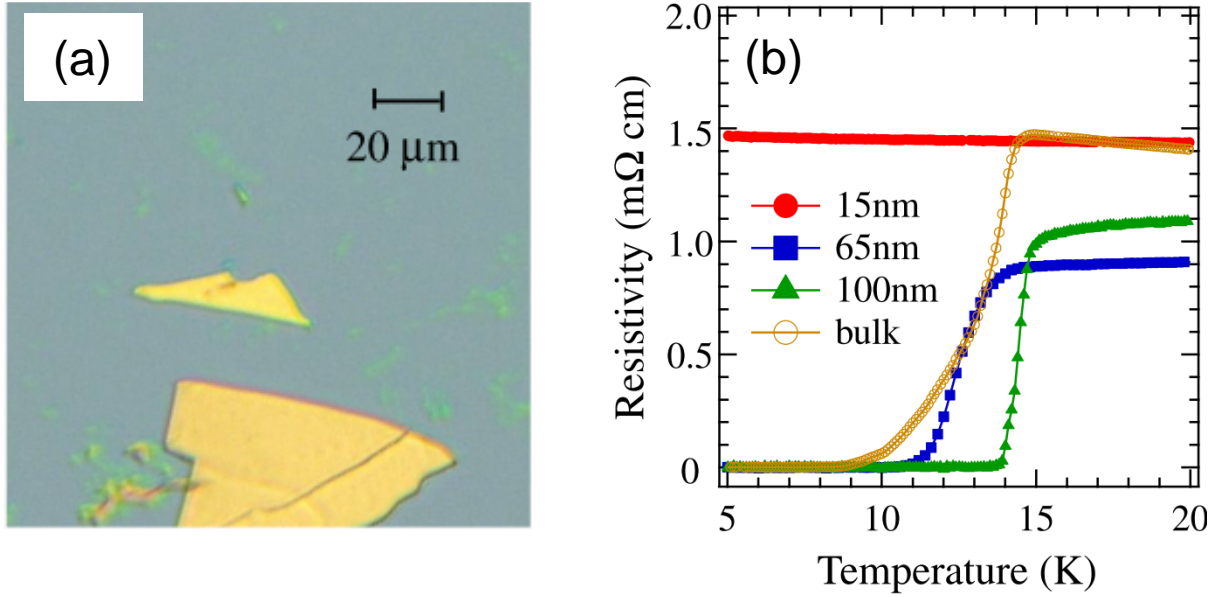


Figure 7.1: (a): Optical image of a FeTe_{0.65}Se_{0.35} thin film fabricated by the Scotch-tape method with the thickness of 65 nm. (b): Thickness dependence of the critical temperature for superconductivity. Samples other than that with 15 nm thickness show superconducting transition.

gigantic SHE in HTSs. As a candidate material, iron-based HTSs might be better than copper-based ones because of their stronger SOI [87]. For example, FeTe_{1-x}Se_x might be useful owing to the strong SOI and accessibility to thin films by the Scotch-tape method [134].

Above we have more focused on iron-based superconductors as materials for the spin injection, but it is also interesting to perform the spin injection into copper-based HTSs. Spin currents are found to be a tool to probe spin fluctuations [135]. One of the most probable pairing mechanisms of Cooper pairs in copper-based superconductors is the antiferromagnetic spin fluctuations [136]. Therefore by injecting spin currents into copper-based HTSs, one can probe these spin fluctuations or moreover, couple spin currents with the spin fluctuations to manipulate them. In this regard, copper-based superconductors are good candidates to explore the potential of spin currents to probe and control the spin fluctuations.

To attain these goals, however, we have things to overcome. First of all, we have to perform nanofabrication of HTSs to integrate them into our lateral devices. Combining the FIB and Ar-ions milling is the most appropriate method to make a nanostructure from HTSs, but it is not so easy. To avoid nanofabrication, other techniques such as the spin pumping can be exploited to inject spin currents into HTSs. However, large effective temperature increase and proximity to ferromagnets are problems [137].

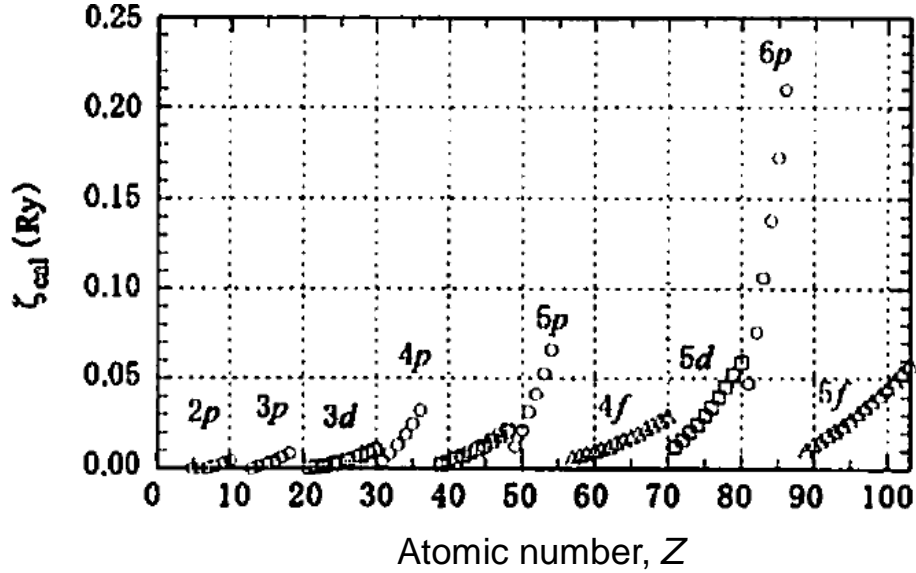


Figure 7.2: Atomic SOI ζ_{cal} from [139] as a function of the atomic number Z . It does not change monotonically with Z .

When we can overcome these technological difficulties, superconducting spintronics will surely be more active research field.

7.2.2 Spin Hall effect in $6p$ metals

As shown in the previous chapters, spin-orbit interaction (SOI) plays a central role in the spin Hall effect (SHE). Finding materials which exhibit large SHE is a key subject in spintronics because they enable us to convert efficiently charge currents into spin currents and *vice versa*. Taking into account the origin of the SHE, materials with strong SOI are therefore the best candidates.

Magnitudes of SOI for metals are often misunderstood: it is often said that SOI is proportional to an atomic number Z or Z^4 thus heavy atoms have large SOI [138]. However, the magnitude of SOI in real materials does not change so simply. In Fig. 7.2 we show results of numerical calculations on atomic SOI (ζ_{cal}) [139]. It is easily found that ζ_{cal} does not monotonically increase with increasing Z , and it changes in a more complex way than that generically recognized. For example, some of the $5p$ metals have stronger SOI than $5f$ metals. The point to note is that $6p$ elements (Tl, Pb, Bi, Po, At and Rn) exhibit remarkably stronger SOI. Among them, we specifically focus on two materials, lead (Pb) and bismuth Bi below.

Pb has been one of the very important materials in our history and is often used in our daily lives. It also becomes superconducting and is a type-I superconductor with relatively higher $T_C = 7.2$ K [98] among metals. Since Pb is expected to have strong

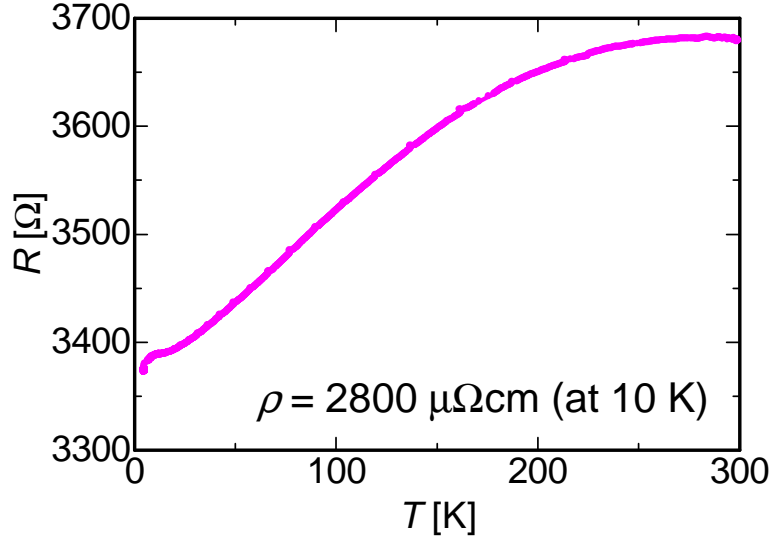


Figure 7.3: Temperature dependence of the resistance of the Bi wire. At 10 K, the resistivity $\rho = 2800 \mu\Omega\text{cm}$, much higher than that for high quality bulk samples.

SOI and also becomes superconducting, it can be a good candidate to observe even larger SHE in the superconducting state than that of NbN, and we can also explore novel effects induced from the competition between superconductivity and SOI on spin transport properties. Bi, on the other hand, is a semimetal with unusual electronic properties due to the highly anisotropic Fermi surface, low carrier concentrations and the small effective mass. Since the Fermi wavelength [140] and mean free path are very long, quantum size effects are expected [141]. Bi is also one of the candidates for the topological insulator [142, 143, 144].

In regard to spintronics, large magnetoresistance in Bi has previously been observed [145, 146], and recently some groups have reported the SHE in Bi [147, 148, 149]. However, the reported spin Hall angles α_{SH} in these previous studies are even smaller than that expected from the strong SOI of Bi. For example, Hou *et al.* has reported $\alpha_{\text{SH}}^{\text{Bi}} = 0.019 \pm 0.002$ at room temperature. This value is comparable to that of Pt [25].

One of the problems for small α_{SH} in the previous studies is the quality of Bi. In [149], for example, the resistivity ρ of Bi is $\rho > 1000 \mu\Omega\text{cm}$ at room temperature, one order of magnitude larger than that of the high quality bulk samples [150]. It is known that it is difficult to fabricate high quality Bi. To evaluate the spin Hall angle of Bi correctly, however, high quality Bi is preferable and dispensable. It is also good to investigate the quantum size effect [151] and its effects on spin transport.

For these reasons, we have started to investigate the SHE in *6p* metals Pb and Bi. We deposit these two materials by the thermal evaporation, under the base pressure $< 10^{-6}$ Torr. In Fig. 7.3 we show the temperature dependence of the resistance of a

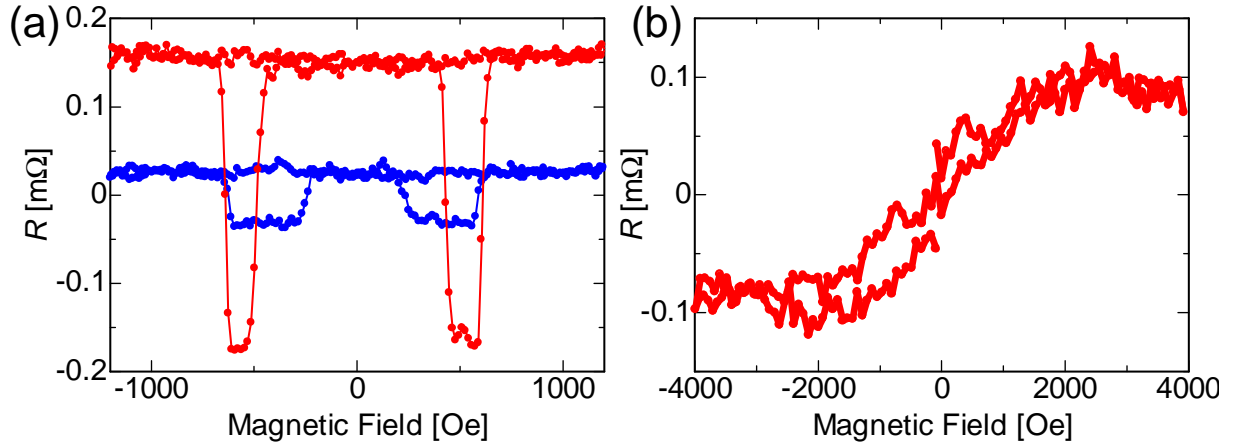


Figure 7.4: (a): NLSV signals with (blue) and without (red) the Bi middle wire at 10 K. Suppressed signal for the blue curve shows the spin absorption effect. (b): ISHE for the Bi wire taken at 10 K.

Bi wire, whose thickness and width are 20 nm and 300 nm, respectively. At 10 K, the resistivity ρ of the Bi wire is $2800 \mu\Omega\text{cm}$, much higher than that of high quality bulk samples.

We next measured the nonlocal spin valve (NLSV) signals and also the inverse spin Hall effect (ISHE) using the Bi wire. Figure 7.4(a) shows the NLSV signals with and without the Bi middle wire. The inverse spin Hall signal is shown in Fig. 7.4(b). By using Fig. 7.4(a) and (b), we evaluate the spin Hall angle (α_{SH}) and the spin relaxation length (λ_{sf}) of the Bi wire. The estimated values at 10 K are $\alpha_{\text{SH}}^{\text{Bi}} = 12.5 \%$ and $\lambda_{\text{sf}}^{\text{Bi}}$ is 0.08 nm, respectively. $\alpha_{\text{SH}}^{\text{Bi}}$ is much larger than those previously reported [148, 149], but λ_{sf} is too short.

At the time of writing this thesis, we have measured the ISHE with only one device, because it is difficult to make a good electrical contact between the probe and the Bi wire. This might be because of the quality of our Bi wires. We do not attempt to fabricate high quality Bi films. In the previous study [145, 146], they used the electro-deposition technique to fabricate high quality Bi. To improve the quality of Bi films, we are planning to change the deposition technique. Since the electro-deposition is not accessible in our group, the candidates are to use the electronbeam (EB) evaporation or sputtering. One of the reasons for high resistivity of our Bi films is that in the thermal evaporation, Bi atoms do not acquire sufficient energy and are immobile on the substrate. Because of the small mobility on the substrate, a Bi layer is not densely packed [152]. Sputtering is in this sense more appropriate since it can control the energy of deposited particles, and these particles can acquire large energy than the thermal evaporation. Modulating the temperature of substrates might also

be important in the sputtering technique.

We briefly remark the future perspectives relevant to Bi and spintronics. Bi has been a significant material in the history of condensed matter physics and there is a growing interests in spintronics these days. Bi itself is sufficiently intriguing, but interface effects with Bi and other materials are also attractive. Large Rashba spin-orbit splitting at the Bi/Ag(111) interface has been reported [153], and using this giant Rashba splitting at the Bi/Ag interface, spin-charge conversion via the Rashba-Edelstein has been recently demonstrated [154]. Signs of the Rashba SOI are also discussed [155, 156, 157]. This kind of interface effects is interesting, and can be one of the candudates for future studies.

We now also attempt to fabricate devices using the other $6p$ metal, Pb. Our main finding for $6p$ metals in general is that it is difficult to make devices with these materials. Pb is fragile, and Pb wires are easily crumbled. Our studies on spin transport in Pb is still ongoing and we have to struggle to make high quality Pb films because it is an ideal material to investigate influence of the competition between superconductivity and strong SOI on regard to spin transport.

Appendix A

Berry phase and Berry curvature

The Berry phase and the Berry curvature are becoming important concepts to understand not only the AHE but also many novel topics in condensed matter physics such as topological insulators or Skyrmions. In this Appendix we briefly explain the theoretical derivation of the Berry phase and the Berry curvature [48]. We recommend a Japanese textbook to learn the derivation of the Berry curvature [158]

The Berry phase is a phase that a quantum mechanical wave function acquires when parameters are adiabatically changed on a closed loop. This phase is determined only by the itinerary therefore can be regarded as a geometric phase. The Berry curvature is derived from the concept of the Berry phase.

Assume a Hamiltonian \mathcal{H} which depends on multiple parameters $\mathbf{R} = (R_1, R_2, \dots)$, namely,

$$\mathcal{H} = \mathcal{H}(\mathbf{R}). \quad (7.1)$$

We can then consider a set of eigen functions and eigen values which depend on \mathbf{R}

$$\mathcal{H}(\mathbf{R})|\phi_n(\mathbf{R})\rangle = E_n(\mathbf{R})|\phi_n(\mathbf{R})\rangle. \quad (7.2)$$

Below we assume that each $E_n(\mathbf{R})$ does not degenerate.

Let us think about a time evolution of parameter \mathbf{R} . We define $|\Phi(t)\rangle$ as an eigenstate of $\mathcal{H}(\mathbf{R}(t))$. We start at the n th eigenvalue $|\phi_n(\mathbf{R})\rangle$

$$|\Psi(t=0)\rangle = |\phi_n(\mathbf{R}(t=0))\rangle. \quad (7.3)$$

Since parameters are changed adiabatically, the eigenstate is expected to stay in the n th eigenstate. The time-dependent Schrödinger equation becomes

$$i\hbar \frac{\partial}{\partial t} |\Psi(t)\rangle = \mathcal{H}(\mathbf{R}(t)) |\Psi(t)\rangle. \quad (7.4)$$

We then assume that the state remain in the n th eigenstate and put an extra phase dependent on t

$$|\Psi(t)\rangle = e^{i\theta(t)} |\phi_n(\mathbf{R}(t))\rangle. \quad (7.5)$$

We substitute this term into the Schrödinger equation

$$\hbar e^{i\theta(t)} \left(-\frac{d\theta(t)}{dt} |\phi_n(\mathbf{R}(t))\rangle + i \frac{\partial}{\partial t} |\phi_n(\mathbf{R}(t))\rangle \right) = E_n(\mathbf{R}(t)) e^{i\theta(t)} |\phi_n(\mathbf{R}(t))\rangle. \quad (7.6)$$

Multiplied by $\langle \phi_n(\mathbf{R}(t)) |$ from the left

$$\frac{d\theta(t)}{dt} = i \langle \phi_n(\mathbf{R}(t)) | \frac{\partial}{\partial t} | \phi_n(\mathbf{R}(t)) \rangle - \frac{1}{\hbar} E_n(\mathbf{R}(t)). \quad (7.7)$$

Therefore $\theta(t)$ can be expressed as

$$\theta(t) = -\frac{1}{\hbar} \int_0^t dt' E_n(\mathbf{R}(t')) + i \int_0^t dt' \langle \phi_n(\mathbf{R}(t')) | \frac{\partial}{\partial t'} | \phi_n(\mathbf{R}(t')) \rangle. \quad (7.8)$$

We define $\gamma(t)$ as

$$\gamma(t) = i \int_0^t dt' \langle \phi_n(\mathbf{R}(t')) | \frac{\partial}{\partial t'} | \phi_n(\mathbf{R}(t')) \rangle, \quad (7.9)$$

then $|\Psi(t)\rangle$ is written as

$$|\Psi(t)\rangle = e^{i\gamma(t)} e^{-i \int_0^t dt' E_n(\mathbf{R}(t'))/\hbar} |\phi_n(\mathbf{R}(t))\rangle. \quad (7.10)$$

The $\gamma(t)$ term is originated from the adiabatical change of \mathbf{R} with t and called the Berry phase.

Let us assume that at $t = T$ parameters become the same as those at $t = 0$, namely, $\mathbf{R}(T) = \mathbf{R}(0)$. In this situation $\gamma(t)$ becomes

$$\begin{aligned} \gamma(T) &= i \int_0^T dt' \langle \phi_n(\mathbf{R}(t')) | \frac{\partial}{\partial t'} | \phi_n(\mathbf{R}(t')) \rangle \\ &= i \oint_C d\mathbf{R} \cdot \langle \phi_n(\mathbf{R}) | \frac{\partial}{\partial \mathbf{R}} | \phi_n(\mathbf{R}) \rangle \\ &= \oint_C d\mathbf{R} \cdot \mathbf{A}_n(\mathbf{R}), \end{aligned} \quad (7.11)$$

where

$$\mathbf{A}_n(\mathbf{R}) = i \langle \phi_n(\mathbf{R}) | \frac{\partial}{\partial \mathbf{R}} | \phi_n(\mathbf{R}) \rangle \quad (7.12)$$

is the Berry connection. The Berry phase is also described as

$$\gamma(t) = \oint_C d\mathbf{R} \cdot \mathbf{A}_n(\mathbf{R}) = \int_S d\mathbf{S} \cdot \mathbf{B}_n(\mathbf{R}), \quad (7.13)$$

where

$$\mathbf{B}_n(\mathbf{R}) = \nabla_{\mathbf{R}} \times \mathbf{A}_n(\mathbf{R}) \quad (7.14)$$

is the Berry curvature. Using (7.12), $\mathbf{B}_n(\mathbf{R})$ is expressed as

$$\mathbf{B}_n(\mathbf{R}) = i \left\langle \frac{\partial \phi_n}{\partial \mathbf{R}} \left| \times \right| \frac{\partial \phi_n}{\partial \mathbf{R}} \right\rangle. \quad (7.15)$$

When we focus on the i component of $\mathbf{B}_n(\mathbf{R})$, it is written as

$$B_{n,i}(\mathbf{R}) = i\varepsilon_{ijk} \left\langle \frac{\partial \phi_n}{\partial R_j} \middle| \frac{\partial \phi_n}{\partial R_k} \right\rangle \quad (7.16)$$

$$= i\varepsilon_{ijk} \sum_m \left\langle \frac{\partial \phi_n}{\partial R_j} \middle| \phi_m \right\rangle \left\langle \phi_m \middle| \frac{\partial \phi_n}{\partial R_k} \right\rangle, \quad (7.17)$$

where ε_{ijk} is the Einstein notation. Since $|\phi_n\rangle$ is normalized, $\langle \phi_n | \phi_n \rangle = 1$. By taking the derivative to R_k for each hand, we find that

$$\left\langle \frac{\partial \phi_n}{\partial R_k} \middle| \phi_n \right\rangle = - \left\langle \phi_n \middle| \frac{\partial \phi_n}{\partial R_k} \right\rangle. \quad (7.18)$$

Thus for $m = n$, (7.17) is zero. When $m \neq n$, by taking the derivative of $\mathcal{H}|\phi_n\rangle = E_n|\phi_n\rangle$ to R_k ,

$$\frac{\partial \mathcal{H}}{\partial R_k} |\phi_n\rangle + \mathcal{H} \left| \frac{\partial \phi_n}{\partial R_k} \right\rangle = \frac{\partial E_n}{\partial R_k} |\phi_n\rangle + E_n \left| \frac{\partial \phi_n}{\partial R_k} \right\rangle. \quad (7.19)$$

Multiplied by $\langle \phi_m |$ for $m \neq n$,

$$\left\langle \phi_m \middle| \frac{\partial \phi_n}{\partial R_k} \right\rangle = \frac{1}{E_n - E_m} \left\langle \phi_m \middle| \frac{\partial \mathcal{H}}{\partial R_k} \middle| \phi_n \right\rangle. \quad (7.20)$$

Similarly,

$$\left\langle \frac{\partial \phi_n}{\partial R_j} \middle| \phi_m \right\rangle = \frac{1}{E_n - E_m} \left\langle \phi_n \middle| \frac{\partial \mathcal{H}}{\partial R_j} \middle| \phi_m \right\rangle. \quad (7.21)$$

Substituting these equations into (7.17), we obtain

$$B_{n,i}(\mathbf{R}) = i\varepsilon_{ijk} \sum_{m \neq n} \frac{\langle \phi_n | \frac{\partial \mathcal{H}}{\partial R_j} | \phi_m \rangle \langle \phi_m | \frac{\partial \mathcal{H}}{\partial R_k} | \phi_n \rangle}{(E_n - E_m)^2}. \quad (7.22)$$

In the equation (7.22) we can easily find that when the n th band is in proximity to the m th band, the Berry curvature $\mathbf{B}_n(\mathbf{R})$ becomes large. The effect of this large Berry curvature close to the band crossing point is extensively studied in many reports and proposed as a dominant mechanism for the anomalous Hall effect [159, 160].

Appendix B

Green's function method to describe superconductivity

In this appendix we briefly review how to express superconductivity with the Green's functions. We can calculate various physical quantities by using the Green's functions, and here we introduce the fundamental equations of motion for the Green's function necessary for calculations on superconductivity. To write this appendix we refer to the famous textbook by Abrikosov, Gor'kov and Dzyaloshinski [161] and lecture notes by Dr. Nagai [162].

Gor'kov equation

Using the field operator, we can write the BCS Hamiltonian as

$$\hat{\mathcal{H}} = \int \psi^\dagger(\mathbf{r})h(\mathbf{r})\psi(\mathbf{r})d^3\mathbf{r} + \frac{1}{2} \int \int \psi_\alpha^\dagger(\mathbf{r})\psi_\beta^\dagger(\mathbf{r}')v(\mathbf{r} - \mathbf{r}')\psi_\beta(\mathbf{r}')\psi_\alpha(\mathbf{r})d^3\mathbf{r}d^3\mathbf{r}'. \quad (7.23)$$

In the BCS theory, the potential $v(\mathbf{r} - \mathbf{r}')$ is assumed as $v(\mathbf{r} - \mathbf{r}') = g\delta(\mathbf{r} - \mathbf{r}')$, where $g \leq 0$ is a constant and $\delta(\mathbf{r})$ is the delta function. Therefore,

$$\hat{\mathcal{H}}_{\text{BCS}} = \int \psi^\dagger(\mathbf{r})h(\mathbf{r})\psi(\mathbf{r})d^3\mathbf{r} + \frac{1}{2}g \int \psi_\alpha^\dagger(\mathbf{r})\psi_\beta^\dagger(\mathbf{r})\psi_\beta(\mathbf{r})\psi_\alpha(\mathbf{r})d^3\mathbf{r}. \quad (7.24)$$

For a generic potential $v = v(\mathbf{r} - \mathbf{r}')$, the equation of motion of the Green's function is expressed as

$$\left[\frac{\partial}{\partial \tau} - (h(\mathbf{r}) - \mu) \right] G_{\alpha\beta}(x, x') = \delta_{\alpha\beta}\delta^{(4)} - \int d^3\mathbf{r}'v(\mathbf{r} - \mathbf{r}')\langle T_\tau[\psi_\gamma^\dagger(\mathbf{r}', \tau)\psi_\gamma(\mathbf{r}', \tau)\psi_\alpha(x)\psi_\beta^\dagger(x')] \rangle. \quad (7.25)$$

Assuming $v(\mathbf{r} - \mathbf{r}') = g\delta(\mathbf{r} - \mathbf{r}')$ and substituting $h(\mathbf{r}) = -\frac{\nabla^2}{2m}$, then

$$\left[-\frac{\partial}{\partial \tau} + \frac{\nabla^2}{2m} + \mu \right] G_{\alpha\beta}(x, x') = \delta_{\alpha\beta}\delta^{(4)}(x - x') - g\langle T_\tau[\psi_\gamma^\dagger(\mathbf{r}, \tau)\psi_\gamma(\mathbf{r}, \tau)\psi_\alpha(x)\psi_\beta^\dagger(x')] \rangle. \quad (7.26)$$

The second term in the rhs is the two-body Green's function, and we approximate it with the single body Green's function using the Wick's theorem;

$$\begin{aligned}
& \langle T_\tau[\psi_\gamma^\dagger(\mathbf{r}, \tau)\psi_\gamma(\mathbf{r}, \tau)\psi_\alpha(x)\psi_\beta^\dagger(x')] \rangle \\
&= -\langle T_\tau[\psi_\gamma(\mathbf{r}, \tau)\psi_\gamma^\dagger(\mathbf{r}, \tau)] \rangle \langle T_\tau[\psi_\alpha(x)\psi_\beta^\dagger(x')] \rangle \\
&+ \langle T_\tau[\psi_\alpha(\mathbf{r}, \tau)\psi_\gamma^\dagger(\mathbf{r}, \tau)] \rangle \langle T_\tau[\psi_\gamma(x)\psi_\beta^\dagger(x')] \rangle \\
&- \langle T_\tau[\psi_\alpha(\mathbf{r}, \tau)\psi_\gamma(\mathbf{r}, \tau)] \rangle \langle T_\tau[\psi_\gamma^\dagger(x)\psi_\beta^\dagger(x')] \rangle \\
&= -G_{\gamma\gamma}(x, x)G_{\alpha\beta}(x, x') \\
&+ G_{\alpha\gamma}(x, x)G_{\gamma\beta}(x, x') \\
&- \langle T_\tau[\psi_\alpha(\mathbf{r}, \tau)\psi_\gamma(\mathbf{r}, \tau)] \rangle \langle T_\tau[\psi_\gamma^\dagger(x)\psi_\beta^\dagger(x')] \rangle.
\end{aligned} \tag{7.27}$$

In (7.27), $G_{\gamma\gamma}(x, x)$ and $G_{\alpha\gamma}(x, x)$ are the self-energy terms. We neglect the first and the second terms and reexpress third term as

$$\begin{aligned}
& -\lim_{\epsilon \rightarrow +0} \langle T_\tau[\psi_\alpha(\mathbf{r}, \tau + \epsilon)\psi_\gamma(\mathbf{r}, \tau - \epsilon)] \rangle \langle T_\tau[\psi_\gamma^\dagger(x)\psi_\beta^\dagger(x')] \rangle \\
&= -\lim_{\epsilon \rightarrow +0} \langle \psi_\alpha(\mathbf{r}, \tau + \epsilon)\psi_\gamma(\mathbf{r}, \tau - \epsilon) \rangle \langle T_\tau[\psi_\gamma^\dagger(x)\psi_\beta^\dagger(x')] \rangle \\
&= -\langle \psi_\alpha(\mathbf{r}, \tau)\psi_\gamma(\mathbf{r}, \tau) \rangle \langle T_\tau[\psi_\gamma^\dagger(x)\psi_\beta^\dagger(x')] \rangle.
\end{aligned} \tag{7.28}$$

We can define $\langle \psi_\alpha(\mathbf{r}, \tau)\psi_\gamma(\mathbf{r}, \tau) \rangle$ as the order parameter;

$$\Delta_{\alpha\beta} = g\langle \psi_\alpha(\mathbf{r}, \tau)\psi_\beta(\mathbf{r}, \tau) \rangle, \tag{7.29}$$

and the anomalous Green's function is defined as

$$F_{\alpha\beta}(x, x') \equiv \langle T_\tau[\psi_\alpha(x)\psi_\beta(x')] \rangle \tag{7.30}$$

$$F_{\alpha\beta}^\dagger(x, x') \equiv \langle T_\tau[\psi_\alpha^\dagger(x)\psi_\beta^\dagger(x')] \rangle. \tag{7.31}$$

Using the above equations, (7.26) becomes

$$\left[-\frac{\partial}{\partial\tau} + \frac{\nabla^2}{2m} + \mu \right] G_{\alpha\beta}(x, x') + \Delta_{\alpha\gamma}(x)F_{\gamma\beta}^\dagger(x, x') = \delta_{\alpha\beta}\delta^{(4)}(x - x'). \tag{7.32}$$

To derive an equation for $F_{\alpha\beta}^\dagger(x, x')$, we can easily find the relation

$$\frac{\partial}{\partial\tau} F_{\alpha\beta}^\dagger(x, x') = -\langle T_\tau[[K, \psi^\dagger(x)]\psi^\dagger(x')] \rangle. \tag{7.33}$$

From the Heisenberg's equation of motion, we can also find

$$-[K, \psi^\dagger(\mathbf{r})] = (h(\mathbf{r}) - \mu)\psi^\dagger(\mathbf{r}, t) + \int \psi^\dagger(\mathbf{r}', t)v(\mathbf{r} - \mathbf{r}')\psi(\mathbf{r}', t)d^3\mathbf{r}'\psi^\dagger(\mathbf{r}, t) \tag{7.34}$$

From (7.33) and (7.34), we can obtain

$$\left[\frac{\partial}{\partial \tau} + \frac{\nabla^2}{2m} + \mu \right] F_{\alpha\beta}^\dagger(x, x') = -g \langle T_\tau [\psi_\gamma^\dagger(\mathbf{r}, \tau) \psi_\gamma(\mathbf{r}, \tau) \psi_\alpha^\dagger(x) \psi_\beta^\dagger(x)] \rangle. \quad (7.35)$$

Using the same approximation as for G , (7.35) is

$$\left[\frac{\partial}{\partial \tau} + \frac{\nabla^2}{2m} + \mu \right] F_{\alpha\beta}^\dagger(x, x') - \Delta_{\alpha\gamma}^*(x) G_{\gamma\beta}(x, x') = 0. \quad (7.36)$$

From (7.32) and (7.36), the Gor'kov equation is

$$\begin{pmatrix} -\frac{\partial}{\partial \tau} + \frac{\nabla^2}{2m} + \mu & -\Delta(x) \\ \Delta^*(x) & \frac{\partial}{\partial \tau} + \frac{\nabla^2}{2m} + \mu \end{pmatrix} \begin{pmatrix} G(x, x') & F(x, x') \\ -F^\dagger(x, x') & G(x, x') \end{pmatrix} = \delta(x - x') I \quad (7.37)$$

Quasiclassical approximation

In the last section we have derived the Gor'kov equation. The Gor'kov equation is easy to solve when the Green's function is relatively spatially homogeneous and without a magnetic field. However, when it is inhomogeneous spatially, analytical solutions for the Gor'kov equation are difficult to derive.

Let us represent a mean value of a physical quantity Q , which becomes

$$\langle Q \rangle = \int \int d^3 \mathbf{r}_1 d^3 \mathbf{r}_2 \delta(\mathbf{r}_1 - \mathbf{r}_2) q(\mathbf{r}_1) \lim_{\tau' \rightarrow \tau} G(\mathbf{r}_1, \mathbf{r}_2; \tau) \quad (7.38)$$

We perform the Fourier transformation to the frequency space and also to the momentum space, namely,

$$\begin{aligned} \langle Q \rangle &= \frac{1}{\beta} \lim_{\tau \rightarrow 0^+} \sum_n \int d^3 \mathbf{r}_1 d^3 \mathbf{r}_2 \frac{d^3 \mathbf{p}_1}{(2\pi)^3} \frac{d^3 \mathbf{p}_2}{(2\pi)^3} q(\mathbf{r}_1) \delta(\mathbf{r}_1 - \mathbf{r}_2) e^{i\mathbf{p}_1 \cdot \mathbf{r}_1} e^{-i\mathbf{p}_2 \cdot \mathbf{r}_2} e^{-i\omega_n \tau} G(\mathbf{p}_1, \mathbf{p}_2; i\omega_n) \\ &= \frac{1}{\beta} \sum_n \int d^3 \mathbf{r}_1 d^3 \mathbf{r}_2 \frac{d^3 \mathbf{p}_1}{(2\pi)^3} \frac{d^3 \mathbf{p}_2}{(2\pi)^3} q(\mathbf{r}_1) \delta(\mathbf{r}_1 - \mathbf{r}_2) e^{i\frac{1}{2}(\mathbf{p}_1 + \mathbf{p}_2) \cdot (\mathbf{r}_1 - \mathbf{r}_2)} e^{i\frac{1}{2}(\mathbf{p}_1 - \mathbf{p}_2) \cdot (\mathbf{r}_1 + \mathbf{r}_2)} \\ &\quad G(\mathbf{p}_1, \mathbf{p}_2; i\omega_n) \\ &= \frac{1}{\beta} \sum_n \int d^3 \mathbf{R} d^3 \mathbf{r} q(\mathbf{R} + \bar{\mathbf{r}}/2) \frac{d^3 \mathbf{p}}{(2\pi)^3} \frac{d^3 \mathbf{k}}{(2\pi)^3} G(\mathbf{p}, \mathbf{k}; i\omega_n) e^{i\mathbf{p} \cdot \bar{\mathbf{r}}} e^{i\mathbf{k} \cdot \mathbf{R}} \delta(\bar{\mathbf{r}}), \end{aligned} \quad (7.39)$$

where $\mathbf{p}_1 = \mathbf{p} + \mathbf{k}/2$, $\mathbf{p}_2 = \mathbf{p} - \mathbf{k}/2$, $\mathbf{r}_1 = \mathbf{R} + \bar{\mathbf{r}}/2$, $\mathbf{r}_2 = \mathbf{R} - \bar{\mathbf{r}}/2$.

We note that variation of the Green's function on \mathbf{p} is much stronger than that of other integrands. The heart of the quasiclassical approximation is to neglect the $|\mathbf{p}|$ dependence of the integrands other than the Green's function and assume that they depend only on the solid angle of \mathbf{p} , $\Omega_{\mathbf{p}}$. Based on this approximation, we can approximate as

$$\frac{d^3 \mathbf{p}}{(2\pi)^3} = \frac{p_F^2}{(2\pi)^3 v_F} d\xi_{\mathbf{p}} d\Omega_{\mathbf{p}}. \quad (7.40)$$

In the equation above we also used the assumptions that for $\Delta \ll E_F$, the Fermi surface is approximately a sphere and that due to the gap anomaly, the states close to the Fermi energy is dominant for the integrands. We can finally obtain

$$\langle Q \rangle = \frac{p_F^2}{\beta(2\pi)^3 v_F} \sum_n \int d^3 \mathbf{R} q(\mathbf{R}) \frac{d^3 \mathbf{k}}{(2\pi)^3} \int d\Omega_{\mathbf{p}} e^{i\mathbf{k} \cdot \mathbf{R}} \int d\xi_{\mathbf{p}} G(\mathbf{p}, \mathbf{k}; i\omega_n). \quad (7.41)$$

Eilenberger equation

The Eilenberger equation is the equation for the quasiclassical Green's functions. We first define the semiclassical anomalous Green's functions as

$$\oint_{E_F} \frac{d\xi_{\mathbf{p}}}{\pi i} F(\mathbf{p}_+, \mathbf{p}_-; i\omega_n) \equiv f(\hat{\mathbf{p}}, \mathbf{k}; i\omega_n), \quad (7.42)$$

$$\oint_{E_F} \frac{d\xi_{\mathbf{p}}}{\pi i} F^\dagger(\mathbf{p}_+, \mathbf{p}_-; i\omega_n) \equiv f^\dagger(\hat{\mathbf{p}}, \mathbf{k}; i\omega_n), \quad (7.43)$$

where $\hat{\mathbf{p}}$ is parallel to \mathbf{r} . We note that the anomalous semiclassical Green's functions have finite values only in the superconducting state. The normal Green's function, on the other hand,

$$\oint \frac{d\xi_{\mathbf{p}}}{\pi i} G(\mathbf{p}_+, \mathbf{p}_-; i\omega_n) \equiv g(\hat{\mathbf{p}}, \mathbf{k}; i\omega_n) \quad (7.44)$$

has a finite value both in the normal state and in the superconducting state and the integral becomes divergent. This problem can be solved by dividing G into two parts, one in the normal state and that in the superconducting state. We do not specify the details of this point further. We define the matrix representation of the semiclassical Green's function as

$$\check{g}(\hat{\mathbf{p}}, \mathbf{k}; i\omega_n) = \begin{pmatrix} g(\hat{\mathbf{p}}, \mathbf{k}; i\omega_n) & f(\hat{\mathbf{p}}, \mathbf{k}; i\omega_n) \\ f^\dagger(\hat{\mathbf{p}}, \mathbf{k}; i\omega_n) & \bar{g}(\hat{\mathbf{p}}, \mathbf{k}; i\omega_n) \end{pmatrix} \quad (7.45)$$

where \bar{g} is the complex conjugate of g . Using its Fourier transformation, we can obtain the Eilenberger equation:

$$-\mathbf{v}_F \cdot \nabla \check{g}(\hat{\mathbf{p}}, \mathbf{r}; i\omega_n) = \left[\begin{pmatrix} i\omega_n + \frac{e}{c} \mathbf{v}_F \cdot \mathbf{A}(\mathbf{r}) & -\Delta(\hat{\mathbf{p}}, \mathbf{r}) \\ \Delta(\hat{\mathbf{p}}, \mathbf{r})^* & -i\omega_n - \frac{e}{c} \mathbf{v}_F \cdot \mathbf{A}(\mathbf{r}) \end{pmatrix}, \check{g}(\hat{\mathbf{p}}, \mathbf{r}; i\omega_n) \right], \quad (7.46)$$

where

$$\nabla \cdot \mathbf{A}(\mathbf{r}) = 0 \quad (7.47)$$

for the vector potential $\mathbf{A}(\mathbf{r})$.

Usadel equation

Usadel equation is the dirty limit of the Eilenberger equation, which we have introduced above. The dirty limit is characterized as $l_e \ll \xi_0$ where l_e is the mean free path and ξ_0

is the coherence length at $T = 0$. In the dirty limit, the Green's function should be spatially homogeneous and independent of the wave vector. Thus we express \check{g} as

$$\check{g}(\mathbf{r}, \mathbf{k}_F) = \check{g}_0(\mathbf{r}) + \mathbf{v}_F \cdot \check{g}_1(\mathbf{r}), \quad (7.48)$$

where the first term is isotropic and the second term expresses the deviation from it. In this regime, because of the strong impurity scattering, only s -wave symmetry is allowed for the pair potential. By substituting (7.48) into the Eilenberger equation (7.46) and taking an average of the Eilenberger equation over the Fermi surface, we can obtain the Usadel equation.

Publications list

Publications in peer-reviewed journals

- [1] T. Wakamura, H. Akaike, Y. Omori, S. Takahashi, Y. Niimi, A. Fujimaki, S. Maekawa and Y. Otani, "Observation of quasiparticles-mediated spin Hall effect in a superconductor", submitted.
- [2] T. Wakamura, N. Hasegawa, K. Ohnishi, Y. Niimi and Y. Otani, "Spin injection into a superconductor with strong spin-orbit coupling", Physical Review Letters (Editors' Suggestion) **112**, 036602 (2014).
- [3] T. Wakamura, K. Ohnishi, Y. Niimi and Y. Otani, "Large spin accumulation with long spin diffusion length in Cu/MgO/Permalloy lateral spin valves", Applied Physics Express **4**, 063002 (2011).
- [4] Y. Omori, F. Auvray, T. Wakamura, Y. Niimi, A. Fert and Y. Otani, "Inverse spin Hall effect in a closed loop circuit", Applied Physics Letters **104**, 072405 (2014).
- [5] Y. Niimi, D. H. Wei, H. Idzuchi, T. Wakamura, T. Kato and Y. Otani, "Experimental verification of comparability between spin-orbit and spin-diffusion lengths", Physical Review Letters **110**, 016805 (2013).

Publications in peer-reviewed proceedings

- [6] T. Wakamura, K. Ohnishi, Y. Niimi and Y. Otani, "Generation of large spin accumulation in S/N/S Josephson junctions", Journal of Physics: Conference Series **400**, 022130 (2012).

Conference contributions

International conferences

- [1] T. Wakamura, H. Akaike, Y. Omori, Y. Niimi, S. Takahashi, A. Fujimaki, S. Maekawa and Y. Otani, "Observation of quasiparticles-mediated spin Hall effect in a superconductor (oral)", 59th Annual Magnetism and Magnetic Materials Conference (MMM2014), Honolulu, the USA, November 2014 (accepted).
- [2] T. Wakamura, N. Hasegawa, K. Ohnishi, Y. Niimi and Y. Otani, "Enhancement of spin relaxation time in superconducting Nb (oral)", The 2014 International Magnetism Conference (INTERMAG 2014), Dresden, Germany, May 2014.
- [3] T. Wakamura, N. Hasegawa, K. Ohnishi, Y. Niimi and Y. Otani, "Spin injection into superconductor with strong spin-orbit coupling (oral)", 4th International Conference on Superconductivity and Magnetism, Antalya, Turkey, April 2014.
- [4] T. Wakamura, Y. Niimi and Y. Otani, "Spin injection into Nb through quasi-particle states (oral)", The 8th International Symposium on Metallic Multilayers (MML2013), Kyoto, Japan, May 2013.
- [5] T. Wakamura, Y. Niimi and Y. Otani, "Spin injection into superconducting Nb by quasiparticle excitation (oral)", The 12th Joint MMM/Intermag Conference, Chicago, the USA, January 2013.
- [6] T. Wakamura, K. Ohnishi, Y. Niimi and Y. Otani, "Generation of large spin accumulation and its application to superconductivity modulation (poster)", The 2nd ASRC International Workshop on Magnetic Materials and Nanostructures, Tokai, Japan, January 2012.
- [7] T. Wakamura, K. Ohnishi, Y. Niimi and Y. Otani, "Generation of large spin accumulation in S/N/S Josephson junctions (poster)", The 26th International Conference on Low Temperature Physics (LT26), Beijing, China, August 2011.
- [8] T. Wakamura, K. Ohnishi, Y. Niimi and Y. Otani, "Large spin accumulation with long spin diffusion length in Cu/MgO/Py lateral spin valves (poster)", The 6th International School and Conference on Spintronics and Quantum Information Technology (SPINTEC6), Matsue, Japan, August 2011.

Domestic conferences

- [9] T. Wakamura, Y. Niimi and Y. Otani, "Application of the odd-frequency spin-triplet superconductors to spintronics (poster)", 2014 Autumn Meeting of the Physical Society of Japan (JPS), Nagoya, Japan, September 2014.
- [10] T. Wakamura, N. Hasegawa, Y. Niimi and Y. Otani, "Spin injection into superconducting Nb through thermally-excited quasi-particle states 2 (oral)", 69th Annual Meeting of the JPS, Sagamihara, Japan, March 2014.
- [11] T. Wakamura, Y. Niimi and Y. Otani, "Attempt to detect the spin Hall effect in superconducting Nb (poster)", 2013 Autumn Meeting of the JPS, Tokushima, Japan, September 2013.
- [12] T. Wakamura, Y. Niimi and Y. Otani, "Spin injection into superconducting Nb through the quasiparticle states (oral)", The 37th Annual Conference on MAGNETICS in Japan, Sapporo, Japan, September 2013.
- [13] T. Wakamura, Y. Niimi and Y. Otani, "Spin injection into superconducting Nb through the thermally excited electrons and gap effects (oral)", 68th Annual Meeting of the JPS, Hiroshima, Japan, March 2013.
- [14] T. Wakamura, Y. Niimi and Y. Otani, "Spin injection into superconducting Nb by thermally excited quasiparticles (oral)", 2012 Autumn Meeting of the JPS, Yokohama, Japan, September 2012.
- [15] T. Wakamura, K. Ohnishi, Y. Niimi and Y. Otani, "Elucidation of the spin absorption mechanism at a superconductor-normal metal interface (poster)", 67th Annual Meeting of the JPS, Osaka, Japan, March 2012.
- [16] T. Wakamura, K. Ohnishi, Y. Niimi and Y. Otani, "Generation of large spin accumulation and its application to superconductivity modulation (oral)", 2011 Autumn Meeting of the JPS, Toyama, Japan, September 2011.
- [17] T. Wakamura, K. Ohnishi, Y. Niimi and Y. Otani, "Effect of large spin accumulation on Josephson critical current in lateral spin valve structure with MgO interface layer (oral)", 66th Annual Meeting of the JPS, Niigata, Japan, March 2011.
- [18] T. Wakamura, K. Ohnishi, Y. Niimi and Y. Otani, "Critical current modulated by no-local spin injection at superconductor/normal-metal/superconductor junction (poster)", 2010 Autumn Meeting of the JPS, Osaka, Japan, September 2010.

Acknowledgements

This work is the product of the wisdom and effort of the author, Taro Wakamura and his company.

The author first wants to express my sincere gratitude to Professor YoshiChika Otani, the advisor of the author. He gives great supports to my work: He is always busy, but spares time for giving me suggestions and instructions on my research. He gives many opportunities to present research results in domestic and international conferences. He allows me to do research as I want to do, which is a great help for me because I can attempt experiments based on my idea, even if they seem ridiculous or reckless. I am very glad to work with him for five years. I also thank to him for giving me a lot of chance to collaborate with other researchers including Professor Sadamichi Maekawa, Professor Saburo Takahashi, Professor Akira Fujimaki and Professor Hiroyuki Akaike.

I am very grateful to Assistant Professor Yasuhiro Niimi. He is a kind of a direct boss to me, and he often gives useful comments and suggestions about my work. Sometimes our opinions do not reach agreement, but his advice is always useful. I also appreciate his kind help to me when I am in trouble. During my five-year graduate-school days, he taught me many things necessary to do research, including how to write abstracts of conferences and manuscripts for journals, how to make a presentation and of course, how to carry out research and how to manipulate equipments. The things I have learned will be also useful in my carrier.

I also thank Assistant Professor Motoi Kimata. I have been working with him since 2012. My research subjects are not directly related to his topics, but I often discuss his or my research results with him. I frequently tell him about what I am wondering about research or condensed matter physics in general. He always gives me some comments even if my question is very ridiculous or strange. We also talk about many things, not only on research, and share a good time. I hope that he will make the nonlocal spin valve device made of PDOT-PSS.

Professor Sadamichi Maekawa, one of my collaborators, gives me many proposals to my research as a theoretician, even though he is always really busy. Professor Rhie in Korea University said, "Professor Maekawa is the god in spintronics." I am really

glad that I can work with the god in spintronics. His comments are always useful and can be hints for us to think profoundly about what is going on in our systems. He helps me to cooperate with other theoreticians in his group, including Dr. Ieda, Dr. Adachi, Dr. Gu, Mr. Ohnuma and an alumuna of his group, Dr. Hikino. I do sincerely appreciate great help of Professor Maekawa and also people in his group.

Professor Saburo Takahashi also helps me a lot. He gives me theoretical supports to my work and also suggestions about how to analyze our experimental data. Our work shown here is mostly based on the papers written by Professor Takahashi and Professor Maekawa. I learn how attractive superconducting spintronics is from those papers. It is also impressive for me that Professor Takahashi has given me many corrections on my manuscripts for a journal. I sincerely thank him for his kindness and warmhearted supports.

I also thank Professor Fujimaki and Professor Akaike in Nagoya University for collaboration with us for the spin Hall effect in superconducting NbN. Professor Akaike must be always very busy, nevertheless he does sputtering NbN layers for me as soon as I send him substrates. I often send him emails and ask him many questions about superconductors. He is a specialist of superconductors and has much expertise. He teaches me many things about superconductors and also experimental techniques to fabricate superconductors with better quality. Professor Fujimaki gives me many useful suggestions based on his long experience in fabrication of superconductor nanodevices.

Professor Takeo Kato gives me a lot of advice for my research. I often ask him questions about my research or general topics on condensed matter physics, and he always answers clearly to those questions. He is a kind of a theoretical advisor for our group. I also appreciate his cooperation for the summer school for students in condensed matter physics, named "BUSSEI WAKATE NATSU NO GAKKOU" in Japanese, held in 2013. He gave fantastic lectures there and shared a good time with students including me. I believe his lectures are very useful for students who are not familiar with mesoscopic physics.

Among other group members in Otani group, I first express my gratitude to two collaborators, Mr. Hasegawa and Mr. Omori. Mr. Hasegawa is really good at programming and numerical calculations. He gives me a lot of support and help for my numerical calculations. I have learned a lot of him. Mr. Omori is also good at the program "Spin-flow 3D", and helped me to carry out three dimensional calculations for spin transport.

As for alumuni, I am especially grateful to Dr. Kohei Ohnishi. He has established a basis for experiments on spin transport in superconductors in our group. We were together in the first two years and I have learned a lot from him.

I want to thank to all other members in Otani group, including Dr. Kondou,

Dr. Bivas, Dr. Kaito, Mr. Hasegawa, Mr. Karube, Mr. Omori, Mr. Takizawa, Ms. Kawamura and Ms. Ishinabe. I also have a feeling of gratitude to alumuni, Dr. Ohnishi, Dr. Sugimoto, Dr. Idzuchi, Dr. Wei, Dr. Rousseau, Prof. Rhie, Mr. Suzuki, Mr. Fujimori, Mr. Kawanishi, Mr. Auvray and Mr. Pinek. We share a good time together and I can enjoy my life in our group thanks to them.

I am also in acknowledgement of direct and indirect support by my parents, Kunio Wakamura and Tatsuko Wakamura.

I would like to acknowledge the use of the lithography to Professor Yasuhiro Iye and Professor Shingo Katsumoto. I am also grateful to technicians in the cleanroom in RIKEN, Kazuhiko Shihoyama and Hajime Kohinata for their kind help.

Finally, I appreciate finalcial supports by the Japan Society for the Promotion of Science (JSPS) and the University of Tokyo.

Bibliography

- [1] I. Zutic, J. Fabian, and S. Das Sharma, *Rev. Mod. Phys.* **76**, 323 (2004).
- [2] N. F. Mott, *Proc. R. Soc. London, Ser. A* **153**, 699 (1936).
- [3] N. F. Mott, *Proc. R. Soc. London, Ser. A* **156**, 699 (1936).
- [4] M. N. Baibach *et al.*, *Phys. Rev. Lett.* **61**, 2472 (1988).
- [5] W. P. Platt *et al.*, *Phys. Rev. Lett.* **66**, 3060 (1991).
- [6] S. Yuasa *et al.*, *Nat. Mater.* **3**, 868 (2004).
- [7] S. S. P. Parkin *et al.*, *Nat. Mater.* **3**, 862 (2004).
- [8] M. Johnson and R. H. Silsbee, *Phys. Rev. Lett.* **55**, 1790 (1985).
- [9] F. J. Jedema, A. T. Filip and B. J. van Wees, *Nature* **410**, 345 (2001).
- [10] N. Tombros *et al.*, *Nature* **448**, 571 (2007).
- [11] N. Reyren *et al.*, *Phys. Rev. Lett.* **108**, 186802 (2012).
- [12] Y. Kajiwara *et al.*, *Nature* **464**, 262 (2010).
- [13] J. Sinova *et al.*, *Phys. Rev. Lett.* **92**, 126603 (2004).
- [14] S. Murakami, N. Nagaosa and S. C. Zhang, *Science* **301**, 1348 (2003).
- [15] S. O. Valenzuela and M. Tinkham, *Nature* **442**, 176 (2006).
- [16] T. Kimura *et al.*, *Phys. Rev. Lett.* **98**, 156601 (2007).
- [17] E. Saitoh *et al.*, *Appl. Phys. Lett.* **88**, 182509 (2006).
- [18] K. Ando *et al.*, *Phys. Rev. Lett.* **101**, 036601 (2008).
- [19] K. Ando *et al.*, *Nat. Mater.* **10**, 655 (2011).
- [20] K. Ando *et al.*, *Nat. Mater.* **12**, 622 (2013).

- [21] O. Monsentz *et al.*, Phys. Rev. Lett. **104**, 046601 (2010).
- [22] L. Q. Liu *et al.*, Phys. Rev. Lett. **106**, 036601 (2011).
- [23] L. Q. Liu *et al.*, Science **336**, 555 (2012).
- [24] C. F. Pai *et al.*, Appl. Phys. Lett. **101**, 122404 (2012).
- [25] M. Morota *et al.*, Phys. Rev. B **83**, 174405 (2011).
- [26] Y. Niimi *et al.*, Phys. Rev. Lett. **106**, 126601 (2011).
- [27] Y. Niimi *et al.*, Phys. Rev. Lett. **109**, 156602 (2012).
- [28] T. Yamashita, S. Takahashi and S. Maekawa, Phys. Rev. B **73**, 144517 (2006).
- [29] S. Takahashi *et al.*, J. Mag. Mag. Mater. **240**, 100 (2002).
- [30] S. Takahashi and S. Maekawa, Jpn. J. Appl. Phys. **51**, 010110 (2012).
- [31] S. A. Kivelson and D. S. Rokhsar, Phys. Rev. B **41**, 11693 (1990).
- [32] C. H. L. Quay *et al.*, Nat. Phys. **9**, 84 (2013).
- [33] F. Hübner *et al.*, Phys. Rev. Lett. **109**, 207001 (2012).
- [34] T. Wakamura *et al.*, Appl. Phys. Exp. **4**, 063002 (2011).
- [35] S. Takahashi and S. Maekawa, Sci. & Tec. of Adv. Mater. **9**, 014105 (2008).
- [36] J. Fabian and S. Das Sharma, J. Vac. Sci. Technol. B **17** 1708 (1999).
- [37] R. J. Elliott, Phys. Rev. **96**, 266 (1954).
- [38] Y. Yafet, *Solid State Physics, Vol. 14*, edited by F. Seitz and D. Turnbull (Academic, New York, 1963).
- [39] F. Beuneu and P. Monod, Phys. Rev. B **18**, 2422 (1978).
- [40] M. I. D'yakonov and V. I. Perel', Sov. Phys. Solid State **13**, 3023 (1971).
- [41] G. L. Bir, A. G. Aronov and G. E. Pikus, Zh. Eksp. Teor. Fiz. **69**, 1382 (1975).
- [42] M. I. D'yakonov and V. I. Perel', Sov. Phys. JETP **38**, 362 (1973).
- [43] A. W. Overhauser, Phys. Rev. **89**, 689 (1953).
- [44] E. H. Hall, Am. J. Math. **2**, 287 (1879).

- [45] A. Kundt, Wied. Ann. **49**, 257 (1893).
- [46] E. M. Pugh and T. W. Lippert, Phys. Rev. **42**, 0709 (1932).
- [47] R. Karplus and J. M. Luttinger, Phys. Rev. **95**, 1154 (1954).
- [48] M. V. Berry, Proceedings of the Royal Society of London **392**, 45 (1984).
- [49] J. Smit, Physica **21**, 877 (1955).
- [50] J. Smit, Physica **24**, 39 (1958).
- [51] L. Berger, Physica **30**, 1141 (1964).
- [52] L. Berger, Phys. Rev. B **2**, 4559 (1970).
- [53] N. Nagaosa *et al.*, Rev. Mod. Phys. **82**, 1539 (2010).
- [54] M. Gradhand *et al.*, Phys. Rev. B **80**, 224413 (2009).
- [55] M. Gradhand *et al.*, Phys. Rev. B **84**, 075113 (2011).
- [56] J. Bardeen, L. N. Cooper and J. R. Schrieffer, Phys. Rev. **108**, 1175 (1957).
- [57] L. N. Cooper, Phys. Rev. **104**, 1189 (1956).
- [58] P. Fulde and R. A. Ferrell, Phys. Rev. **135**, A550 (1964).
- [59] A. I. Larkin and Y. N. Ovchinnikov, Sov. Phys. JETP **20**, 762 (1965).
- [60] V. V. Ryazanov *et al.*, Phys. Rev. Lett. **86**, 2427 (2001).
- [61] T. Kontos *et al.*, Phys. Rev. Lett. **89**, 137007 (2002).
- [62] V. A. Oboznov *et al.*, **96**, 197003 (2006).
- [63] M. Eschrig and T. Löfwander, Nat. Phys. **4**, 138 (2008).
- [64] F. S. Bergeret, A. F. Volkov and K. B. Efetov, Phys. Rev. Lett. **86**, 4096 (2001).
- [65] F. S. Bergeret, A. F. Volkov and K. B. Efetov, Rev. Mod. Phys. **77**, 1321 (2005).
- [66] R. S. Keizer *et al.*, Nature **439**, 825 (2006).
- [67] S. Hikino and S. Yunoki, Phys. Rev. Lett. **110**, 237003 (2013).
- [68] E. Zhao and J. A. Sauls, Phys. Rev. B **78**, 174511 (2008).
- [69] J. Linder and K. Halterman, arXiv:1401.5806v1.

- [70] H. Yang *et al.*, Nat. Meter **9**, 586 (2010).
- [71] Y. -S. Shin, H. -J. Lee and H. -W. Lee, Phys. Rev. B **71**, 144513 (2005).
- [72] J. Bardeen *et al.*, Phys. Rev. **113**, 982 (1959).
- [73] J. M. Pomeroy and H. J. Grube, J. Appl. Phys. **105**, 094503 (2009).
- [74] J. S. Moodera *et al.*, Appl. Phys. Lett. **69**, 708 (1996).
- [75] J. Clarke, Phys. Rev. Lett. **28**, 1363 (1972).
- [76] P. Cadden-Zimansky, Z. Jiang and V. Chandrasekhar, New. J. Phys. **9**, 116 (2007).
- [77] P. Cadden-Zimansky and V. Chandrasekhar, Phys. Rev. Lett. **97**, 237003 (2006).
- [78] D. A. Papaconstantopoulos, in *Handbook of the Band Structure of Elemental Solids* (Plenum, New York 1986).
- [79] N. W. Ashcroft and N. D. Mermin, in *Solid State Physics* Ch2 (Saunders College 1976).
- [80] S. Takahashi and S. Maekawa, Phys. Rev. Lett. **88**, 116601 (2002).
- [81] P. G. De Gennes, in *Superconductivity of Metals and Alloys* 2nd ed. (Westview Press 1999).
- [82] A. I. Buzdin, Rev. Mod. Phys. **77**, 935 (2005).
- [83] K. D. Usadel, Phys. Rev. Lett. **25**, 507 (1970).
- [84] W. Belzig, *et al.*, Superlattice and Microstructures **25**, 1251 (1999).
- [85] W. Belzig, C. Bruder and G. Schon, Phys. Rev. B **54**, 9443 (1996).
- [86] S. Gueron *et al.*, Phys. Rev. Lett. **77**, 3025 (1996).
- [87] T. Kato (private communication).
- [88] M. Tinkham, in *Introduction to Superconductivity* 2nd ed. (Dover 2004).
- [89] A. Hoffmann, IEEE Trans. Mag. **49**, 5172 (2013).
- [90] T. Wakamura *et al.*, Phys. Rev. Lett. **112**, 036602 (2014).
- [91] K. Ohnishi, PhD thesis (in Japanese).

- [92] A. Fujimaki (private communication).
- [93] M. Grandhand (private communication).
- [94] H. Kontani, J. Goryo and D. S. Hirashima, *Phys. Rev. Lett.* **102**, 086602 (2009).
- [95] S. Hikino and S. Yunoki, *Phys. Rev. B* **84**, 020512 (2011).
- [96] S. Pandey *et al.*, *Phys. Rev. B* **86**, 060507 (2012).
- [97] A. Shoji, S. Kiryu and S. Kohjiro, *Appl. Phys. Lett.* **60**, 1624 (1992).
- [98] C. Kittel, in *Introduction to Solid State Physics* 7th ed. (Wiley 1996).
- [99] Y. Tian, L. Ye and X. Jin, *Phys. Rev. Lett.* **103**, 087206 (2009).
- [100] K. Yu. Arutyunov, H. -P. Auraneva and A. S. Vasenko, *Phys. Rev. B* **83**, 104509 (2011).
- [101] H. J. Mamin, J. Clarke and D. J. Van Harlingen, *Phys. Rev. B* **29**, 3881 (1984).
- [102] M. Henny *et al.*, *Phys. Rev. B* **59**, 2871 (1999).
- [103] F. C. Wellstood, C. Urbina and J. Clarke, *Phys. Rev. B* **49**, 5942 (1994).
- [104] F. Mallet, *et al.*, *Phys. Rev. Lett.* **97**, 226804 (2006).
- [105] H. Akaike (private communication).
- [106] Y. Maeno *et al.*, *Nature* **372**, 532 (1994).
- [107] F. Romeo and R. Citro, *Phys. Rev. Lett.* **111**, 226801 (2013).
- [108] P. W. Anderson, *J. Phys. Chem. Solids* **11**, 26 (1959).
- [109] J. W. A. Robinson, J. D. S. Witt and M. G. Blamire, *Science* **329**, 59 (2010).
- [110] T. S. Khaire *et al.*, *Phys. Rev. Lett.* **104**, 137002 (2010).
- [111] C. Klose *et al.*, *Phys. Rev. Lett.* **108**, 127002 (2012).
- [112] J. Wang *et al.*, *Nat. Phys.* **6**, 389 (2010).
- [113] E. S. Sadki, S. Ooi and K. Hirata, *Appl. Phys. Lett.* **85**, 6206 (2004).
- [114] J. W. Gibson and R. A. Hein, *Phys. Rev. Lett.* **12**, 688 (1964).
- [115] M. S. Osofsky *et al.*, *Phys. Rev. Lett.* **87**, 197004 (2001).

- [116] J. Linder *et al.*, Phys. Rev. Lett. **102**, 107008 (2009).
- [117] M. Kompaniets *et al.*, Appl. Phys. Lett. **104**, 052603 (2014).
- [118] S. Chikazumi, in *Physics of Ferromagnetism* 2nd ed. (Clarendon Press 1997).
- [119] J. W. A. Robinson, N. Banerjee and M. G. Blamire, Phys. Rev. B **89**, 104505 (2014).
- [120] P. Dhakal *et al.*, arXiv:1006.2173.
- [121] R. Cordoba *et al.*, Nat. Comm. **4**, 1437 (2013).
- [122] A. Fernández-Pacheco *et al.*, Phys. Rev. B **79**, 174204 (2009).
- [123] T. Maassen *et al.*, Nano Lett. **12**, 1498 (2012).
- [124] W. Han *et al.*, Phys. Rev. Lett. **105**, 167202 (2010).
- [125] H. B. Heersche *et al.*, Nature **446**, 56 (2006).
- [126] T. Yamashita, S. Takahashi and S. Maekawa, Phys. Rev. B **73**, 144517 (2006).
- [127] D. Greenbaum, *et al.*, Phys. Rev. B **75**, 195437 (2007).
- [128] J. G. Bednorz and K. A. Müller, Z. Phys. B **64**, 189 (1986).
- [129] J. R. Gavaler, Appl. Phys. Lett. **23**, 480 (1973).
- [130] M. K. Wu *et al.*, Phys. Rev. Lett. **58**, 908 (1987).
- [131] R. M. Hansen *et al.*, Phys. Rev. Lett. **60**, 1174 (1988).
- [132] Y. Kamihara *et al.*, J. Am. Chem. Soc. **130**, 3296 (2008).
- [133] J. Paglione and R. L. Greene, Nat. Phys. **6**, 645 (2010).
- [134] H. Okazaki *et al.*, J. Phys. Soc. Jpn. **81**, 113707 (2012).
- [135] D. H. Wei *et al.*, Nat. Comm. **3**, 1058 (2012).
- [136] T. Moriya and K. Ueda, Advances in Physics **49**, 555 (2000).
- [137] E. Saitoh (private communication)
- [138] H. L. Wang *et al.*, Phys. Rev. Lett. **113**, 097202 (2014).
- [139] KOTAI BUTSURI **46**, 299 (2011) (in Japanese).

- [140] G. E. Smith, G. A. Baraff and J. M. Rowell, Phys. Rev. **135**, A1118 (1964).
- [141] M. Lu *et al.*, Phys. Rev. B **53**, 1609 (1996).
- [142] S. Murakami, Phys. Rev. Lett. **97**, 236805 (2006).
- [143] T. Hirahara *et al.*, Phys. Rev. Lett. **97**, 146803 (2006).
- [144] T. Hirahara *et al.*, Appl. Phys. Lett. **91**, 202106 (2007).
- [145] F. Y. Yang *et al.*, Science **284**, 1335 (1999).
- [146] F. Y. Yang *et al.*, Phys. Rev. Lett. **82**, 3328 (1999).
- [147] J. Fan and J. Eom, Appl. Phys. Lett. **92**, 142101 (2008).
- [148] D. Hou *et al.*, Appl. Phys. Lett. **101**, 042403 (2012).
- [149] H. Emoto *et al.*, J. Appl. Phys. **115**, 17C507 (2014).
- [150] D. L. Partin *et al.*, Phys. Rev. B **38**, 3818 (1988).
- [151] N. Garcia, Y. H. Kao and M. Strongin, Phys. Rev. B **5**, 2029 (1972).
- [152] K. W. Rhie (private communication).
- [153] C. R. Ast *et al.*, Phys. Rev. Lett. **98**, 186807 (2007).
- [154] J. C. Rojas Sánchez *et al.*, Nat. Comm. **4**, 2944 (2013).
- [155] H. Bentmann *et al.*, Phys. Rev. B **84**, 115426 (2011).
- [156] F. Meier *et al.*, Phys. Rev. B **79**, 241408 (2009).
- [157] S. Karube (private communication).
- [158] E. Saitoh and S. Murakami, in *Spin Currents and Topological Insulators* (in Japanese, Kyoritsu Shuppan 2014).
- [159] S. Onoda, N. Sugimoto and N. Nagaosa, Phys. Rev. Lett. **97**, 126602 (2006).
- [160] Y. Yao *et al.*, Phys. Rev. Lett. **92**, 037204 (2004).
- [161] A. A. Abrikosov, L. P. Gor'kov and L. E. Dzyaloshinski, in *Methods of Quantum Field Theory in Statistical Physics* (Dover, 1975).
- [162] Lecture notes by Dr. Nagai in JAEA (in Japanese) uploaded in <http://park.itc.u-tokyo.ac.jp/kato-yusuke-lab/nagai/nagainotes.htm>